Fall 2018

Structured low rank approaches for exponential recovery - application to MRI

Arvind Balachandrasekaran
University of Iowa

STRUCTURED LOW RANK APPROACHES FOR EXPONENTIAL RECOVERY - APPLICATION TO MRI

by

Arvind Balachandrasekaran

A thesis submitted in partial fulfillment of the
requirements for the Doctor of Philosophy degree
in Electrical and Computer Engineering
in the Graduate College of
The University of Iowa

December 2018

Thesis Supervisor: Associate Professor Mathews Jacob

Graduate College
The University of Iowa
Iowa City, Iowa

CERTIFICATE OF APPROVAL

PH.D. THESIS

This is to certify that the Ph.D. thesis of

Arvind Balachandrasekaran

has been approved by the Examining Committee for the thesis requirement for the Doctor of Philosophy degree in Electrical and Computer Engineering at the December 2018 graduation.

Thesis Committee: _____
Mathews Jacob, Thesis Supervisor

_____
Weiyu Xu

_____
Soura Dasgupta

_____
Sajan Goud Lingala

_____
Vincent Magnotta

ACKNOWLEDGEMENTS

When I started this journey towards a PhD degree, I felt that I was taking a road in pitch darkness and I couldn't see where I was going and the destination was not in sight. As I proceeded, I encountered several people who lit up my path and helped me find my way. Now, I would like to take this opportunity to thank these people.

First and foremost, I would like to thank Professor Mathews Jacob. I have been very fortunate to have him as my mentor. He gave me a wide range of interesting problems to work on. I have always found his door to be open when I needed guidance, and he has calmly and patiently answered all my questions. At times, when my progress was slow, he has been very encouraging and given me hope that I will figure out a way to solve the problems. I have found him to be very enthusiastic about research, and he has shaped my ideas about how to be a good researcher. I believe that through the course of my PhD, my maturity as a researcher has grown tremendously, and I owe this to my advisor.

I would like to thank my committee members Professor Soura Dasgupta, Professor Weiyu Xu, Professor Vincent Magnotta and Professor Sajan Goud Lingala for taking time out of their busy schedule and agreeing to be in my committee. Their valuable suggestions and inputs have enhanced my understanding of my work and offered fresh perspectives on the various problems I have been trying to solve.

I have been very fortunate to be taught by amazing Professors at the University. I thank them for being in this noble profession and for their continued commitment to imparting wisdom to the students.

I would like to thank my collaborators Dr. Gregory Ongie, Dr. Merry Mani and Dr Stanley Kruger. One of the projects in my thesis was an extension and application of Greg's work to dynamic MRI. Greg was patient enough to explain the ideas behind his work and my discussions with him helped me to make quick progress. Merry has been patient and has always assisted me in acquiring data from the scanner. Stan

has been kind enough to teach me to work with the scanner, so that I can acquire data with minimal assistance.

I would like to thank Cathy and Dina for all their help. They have answered all my questions patiently and calmly. Special thanks to Cathy for her encouraging words during exams and other stressful times.

I would also like to thank Kori Rich, Autumn Craig and Marla Kleingartner for their help in acquiring data from the scanner.

I would like to thank all my past and present lab members for making me feel less alone in this journey. The chatter in the lab definitely lightened me up and helped me de-stress.

I met my wife and best friend Sunrita here in grad school. She has always held my hand, assuring me that I was not alone in this journey. Whenever I went astray, she had this uncanny ability to steer me back in the right direction. I have had a lot of fun discussing about everything 'under the sun' with her. We have had numerous illuminating discussions about science, politics, philosophy, food, movies, books, universe, and countless other things. I enjoyed every second of it. In this journey, she has been the one person who was constantly shining light on my path. I thank her for all the love, encouragement and support she has given me during this difficult journey.

I am also extremely fortunate to have the finest group of friends. We call ourselves the "Droogs". Our mutual interest in movies brought us together. Discussing with them about different topics ranging from politics to movies to books has certainly enlightened me about various aspects of life. I would like to especially thank Ananth for introducing me to the world of Murakami by suggesting that I read "Hard boiled wonderland and the end of the world". This re-kindled my love for reading and encouraged me to explore many different authors.

I would like to thank my brother Arun and my sister-in-law Sunitha. They have

always welcomed me, taken care of me and fed me with amazing food, making me feel at home even though I was away from India. My cute nephews Akshan and Aryav were always there to make me forget about the worries of PhD life for a short period of time. I would like to thank my mom (Amma), dad (Appa) and Lalli sithi for their continued love, support and encouragement throughout my PhD. Amma and Appa have always believed in me and have supported all my decisions. I feel extremely blessed and fortunate to have such amazing parents.

Finally I thank the universe for bringing the necessary forces together and having created the circumstances which inspired me to take up this interesting journey.

ABSTRACT

Recovering a linear combination of exponential signals characterized by parameters is highly significant in many MR imaging applications such as parameter mapping and spectroscopy. The parameters carry useful clinical information and can act as biomarkers for various cardiovascular and neurological disorders. However, their accurate estimation requires a large number of high spatial resolution images, resulting in long scan time. One of the ways to reduce scan time is by acquiring undersampled measurements. The recovery of images is usually posed as an optimization problem, which is regularized by functions enforcing sparsity, smoothness or low rank structure. Recently structured matrix priors have gained prominence in many MRI applications because of their superior performance over the aforementioned conventional priors. However, none of them are designed to exploit the smooth exponential structure of the 3D dataset.

In this thesis, we exploit the exponential structure of the signal at every pixel location and the spatial smoothness of the parameters to derive a 3D annihilation relation in the Fourier domain. This relation translates into a product of a Hankel/Toeplitz structured matrix, formed from the $k-t$ samples, and a vector of filter coefficients. We show that this matrix has a low rank structure, which is exploited to recover the images from undersampled measurements. We demonstrate the proposed method on the problem of MR parameter mapping. We compare the algorithm with the state-of-the-art methods and observe that the proposed reconstructions and parameter maps have fewer artifacts and errors.

We extend the structured low rank framework to correct field inhomogeneity artifacts in MR images. We introduce novel approaches for field map compensation for data acquired using Cartesian and non-Cartesian trajectories. We adopt the time segmentation approach and reformulate the artifact correction problem into a recovery of time series of images from undersampled measurements. Upon recovery,

the first image of the series will correspond to the distortion-free image. With the above re-formulation, we can assume that the signal at every pixel follows an exponential signal characterized by field map and the damping constant $\mathbf{R}_2^*$. We exploit the smooth exponential structure of the 3D dataset to derive a low rank structured matrix prior, similar to the parameter mapping case. We demonstrate the algorithm on spherical MR phantom and human data and show that the artifacts are greatly reduced compared to the uncorrected images.

Finally, we develop a structured matrix recovery framework to accelerate cardiac breath-held MRI. We model the cardiac image data as a 3D piecewise constant function. We assume that the zeros of a 3D trigonometric polynomial coincides with the edges of the image data, resulting in a Fourier domain annihilation relation. This relation can be compactly expressed in terms of a structured low rank matrix. We exploit this low rank property to recover the cardiac images from undersampled measurements. We demonstrate the superiority of the proposed technique over conventional sparsity and smoothness based methods. Though the model assumed here is not exponential, yet the proposed algorithm is closely related to that developed for parameter mapping.

The direct implementation of the algorithms has a high memory demand and computational complexity due to the formation and storage of a large multi-fold Toeplitz matrix. Till date, the practical utility of such algorithms on high dimensional datasets has been limited due to the aforementioned reasons. We address these issues by introducing novel Fourier domain approximations which result in a fast and memory efficient algorithm for the above-mentioned applications. Such approximations allow us to work with large datasets efficiently and eliminate the need to store the Toeplitz matrix. We note that the algorithm developed for exponential recovery is general enough to be applied to other applications beyond MRI.

PUBLIC ABSTRACT

In many Magnetic Resonance Imaging (MRI) applications the underlying signal of interest at every pixel location behaves in a exponential manner. Such a signal is usually characterized by parameters, which carry important clinical information about various pathologies, including cardiovascular and brain disorders. Since MRI is a slow imaging modality it takes a long time to acquire the high resolution images, which are needed to estimate these parameters accurately. One of the ways to reduce scan time is to collect only few measurements per image. Using computational approaches, the remaining samples of each image can be estimated by exploiting the structures present in the images.

In this thesis, we exploit the exponential behavior of the signal at every pixel location along with the smoothness of the parameters across the spatial locations to recover the remaining samples of each image. We demonstrate the proposed idea in a few MRI applications such as parameter mapping, artifact correction in MRI and reconstructing cardiac breath-held images from few acquired measurements. We show that images reconstructed using the proposed idea have fewer artifacts and errors than those obtained from the competing methods.

The straightforward implementation of the algorithm requires a lot of computer memory and is computationally expensive. Till date, the practical utility of such algorithms on large datasets was limited due to the aforementioned reasons. To address these issues, we introduce novel approximations to the algorithms presented for each application. These approximations enable us to work with very large data sets efficiently. We also note that the algorithm developed for exponential signal recovery is general enough to be applied to other applications in MRI and beyond.

TABLE OF CONTENTS

LIST OF TABLES

Table

LIST OF FIGURES

Figure

CHAPTER 1
INTRODUCTION

Recovering a linear combination of exponential signals is highly significant in many Magnetic Resonance (MR) Imaging applications such as MR parameter mapping [8, 76], MR spectroscopy [11], fat/water imaging [20] etc. In these applications, the measured signal, which can be characterized by a few parameters, varies exponentially with time. The main objective in these applications is to recover a series of images corresponding to the sampled time points of the exponential curve. From the recovered images, the parameters are estimated by fitting a single or multi-exponential signal at each pixel location. The estimated spatial map of parameters provide useful clinical information and act as biomarkers for various pathologies including cardiovascular and neurological disorders [8,11,76]. For instance in MR parameter mapping, the spatial map of the parameters is dependent on the underlying tissue micro-structure. They provide valuable information regarding tissue properties and can be used for early diagnosis of various disorders including neurological, musculoskeletal and cardiovascular disorders [8, 76]. Similarly in MR spectroscopic imaging a spatial map of metabolite concentrations is estimated from the series of images. These concentrations maps can be used to study the metabolism of different molecules and are very useful in the investigation of neurological disorders [11]. Hence it is absolutely necessary to estimate these spatial maps accurately.

Usually a series of high spatial resolution images is required for the accurate estimation of these parameters. However the acquisition of these images results in a long scan time due to the inherently slow nature of the MR imaging modality. Specifically, the physical constraints on the gradient hardware and the physiological constraints such as the risk of peripheral nerve stimulation place a limit on the achievable speed of acquisition. One of the ways to reduce the acquisition time is by performing an undersampling operation and acquiring only a fraction of the full

Fourier space measurements. However the recovery of images from very few measurements is an ill-posed problem; we have to exploit the structure present in the signal to make the problem well-posed. Some of the common signal structures exploited are the sparsity in the signal or transform domain (e.g., Wavelet or Fourier domain) smoothness and low-rankness [7, 12, 14, 24, 33, 64, 77, 79–82]. Typically in compressive sensing algorithms, the recovery is posed as an optimization problem regularized by functions that enforce the aforementioned signal structures. In this thesis, we derive a novel Fourier domain structured matrix prior by exploiting the exponential signal structure along with other structures present in the MR images. We enforce this prior and solve an optimization problem to recover the time series of images from undersampled measurements.

1.1 Problem statement

Let the time series of images be represented in Casorati matrix [34] form as $\boldsymbol{\rho} = [\boldsymbol{\rho}_1, \boldsymbol{\rho}_2, \dots \boldsymbol{\rho}_T] \in \mathbb{C}^{B \times T}$ where the i^{th} column of $\boldsymbol{\rho}$ represents a vector of image data at time instant t_i. We also assume that the temporal profile of $\boldsymbol{\rho}$ at every pixel location follows an exponential curve. We model this signal as a linear combination of L exponentials:

$$\rho[\mathbf{r}, n] = \sum_{i=1}^{L} \alpha_i(\mathbf{r})\ \beta_i(\mathbf{r})^n, \tag{1.1}$$

where $\alpha_i(\mathbf{r}) \in \mathbb{C}$ are the amplitudes, $\beta_i(\mathbf{r}) \in \mathbb{C}$ is the exponential parameter that is dependent on the underlying physiology, n refers to the signal index along the parameter dimension and L is the number of exponentials at the voxel.

In this thesis we are interested in recovering the time series of images $\boldsymbol{\rho}$ from the corresponding Fourier measurements $\mathbf{b}$. The multi-channel Fourier measurements $\mathbf{b}$ corresponding to the image series $\boldsymbol{\rho}$ can be modeled linearly as follows:

$$\mathbf{b} = \mathcal{A}(\boldsymbol{\rho}) + \boldsymbol{\eta} \tag{1.2}$$

where $\mathcal{A}$ is a linear acquisition operator. Since (1.2) is an ill-posed problem, we exploit the exponential signal structure present at every pixel along with the structure present in the MR images to recover the time series of images.

1.2 Motivation for proposed work: Prony's method

Recovering parameters of the linear combination of exponential signals is a well studied problem in signal processing. One of the first persons to study this problem was Prony, who devised an elegant method to estimate the parameters characterizing the exponential signals from a few uniformly spaced measurements. Here we briefly describe Prony's method [72], which is the main motivation behind the algorithms developed in this thesis.

Let $\widehat{\rho}[k]$ be a 1D signal, which is described using a L exponential signal model. Given only a few uniformly spaced samples of $\widehat{\rho}[k]$, the goal of Prony's method is to recover a signal $\rho[n]$, which is made up of a linear combination of L Diracs. The signals $\rho[n]$ and $\widehat{\rho}[k]$ are depicted in Fig. 1.1. The number of unknowns in this problem is $2L$ and they correspond to the amplitude and location of the Diracs. Hence from a simple degrees of freedom argument, we can deduce that the number of measurements needed for the recovery of the parameters is atleast $2L$.

We observe that the complex exponential signal $\widehat{\rho}[k]$ can be annihilated by a $L+1$ tap FIR filter [72]:

$$\sum_{m=0}^{L} \widehat{\rho}[m]\ \widehat{h}[n-m] = 0 \tag{1.3}$$

where the above equation represents a 1D convolution relation between the signal $\widehat{\rho}[k]$ and $\widehat{h}[k]$. Taking inverse Fourier transform on both sides of (1.3), the above relation translates into a product between a stream of Diracs $\rho[n]$ and a trigonometric polynomial $h[n]$; the zeros of a trigonometric polynomial coincides exactly with the location of the Diracs. The polynomial $h[n]$ is termed as an annihilating polynomial. Refer to Fig. 1.1 for an illustration of the annihilation relations.

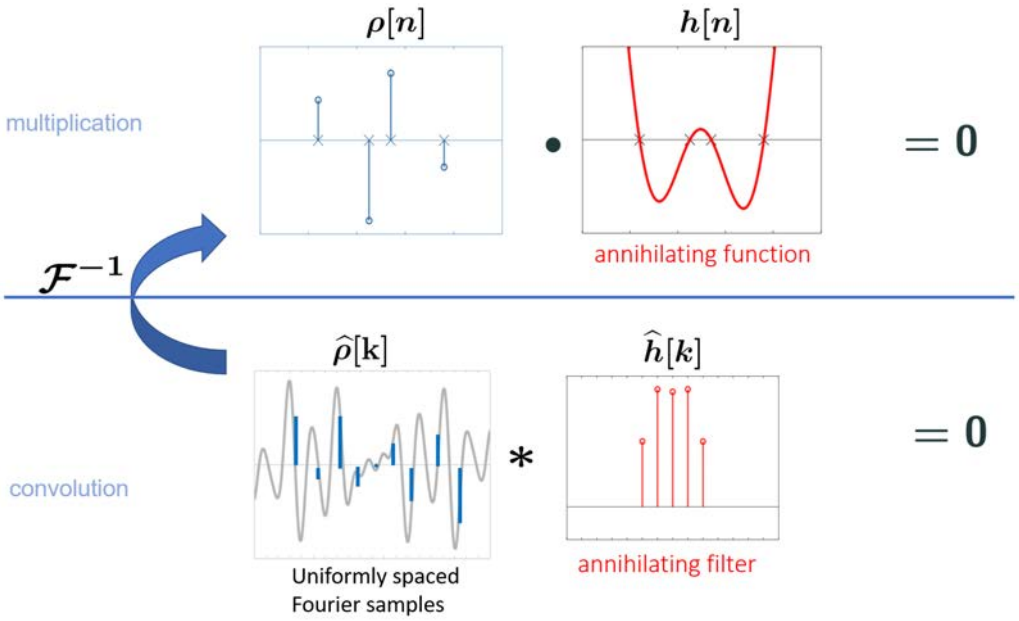

Figure 1.1: Prony's method to recover the amplitudes and locations of Diracs representing $\rho[n]$: $\widehat{\rho}[k]$ is a linear combination of 4 complex exponentials. Given only a few uniformly spaced samples of $\widehat{\rho}[k]$, the goal is to estimate the location and amplitude of the Diracs representing $\rho[n]$. The convolution of $\widehat{\rho}[k]$ with a five tap filter $\widehat{h}[k]$ is zero. This relation gives rise to a system of linear equations, which can be solved to obtain the filter coefficients. The convolution relation translates to a multiplication in the Fourier domain. We can obtain the location of Diracs from the the zero crossings of $h[n]$. Finally, the amplitudes can be obtained by solving another system of linear equations.

The first step in Prony's method is to estimate the location of the Diracs using the uniformly spaced samples. When $2L$ samples of $\widehat{\rho}[k]$ are atleast known at contiguous locations, we can form a system of linear equations from the relation in (1.3) and solve for the $L+1$ unknown filter coefficients. Taking the inverse Fourier transform of the filter coefficients then yields the annihilating polynomial $h[n]$. The zero crossings of the polynomial which gives the location of the Diracs can be deduced from the roots of the polynomial. We can substitute the location of Diracs in the exponential signal model and estimate the amplitudes by solving another overdetermined system of equations.

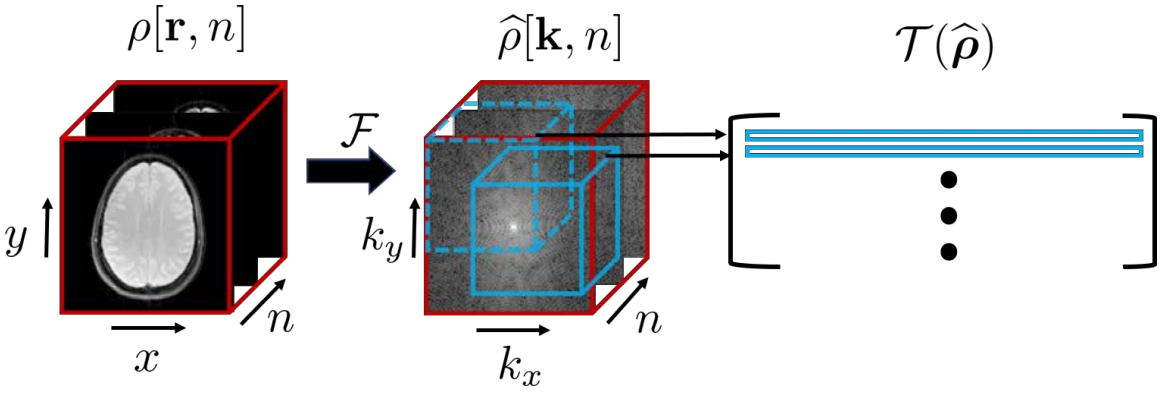

Figure 1.2: Illustration of the construction of the Toeplitz matrix: The rows of the Toeplitz matrix correspond to the cuboid shaped neighborhoods of the Fourier samples. The number of columns is equal to the size of the filter support. Similarly, the number of rows is equal to the number of valid linear convolutions between $\widehat{\rho}[\mathbf{r}, n]$ and the filter.

Similar to Prony's method, in this work we exploit the linear predictability of exponential signals to estimate the exponential parameter β and the amplitude α at every spatial location. In the next section, we give a brief overview about structured matrix priors, whose low-rankness is exploited to recover the parameters of the exponential signal from undersampled measurements.

1.3 Structured matrix prior for exponential recovery

In many MRI applications, structured matrix priors are emerging as powerful alternatives for conventional priors such as sparsity (ℓ_1) or smoothness (TV) based priors. Typically in structured matrix recovery methods, an annihilation relation similar to (1.3) is derived between a signal and a FIR filter. This relation can be compactly represented as a product of a Hankel/Toeplitz matrix formed from the signal samples and a vector of filter coefficients. Such a matrix is shown to have a low rank structure, which is exploited to recover the signal from undersampled measurements.

In this thesis, we derive a structured low rank matrix prior by exploiting the

exponential behavior of the signal at every pixel location along with the smoothness of the exponential parameter ($\beta(\mathbf{r})$). The low rank property is exploited to recover the exponential image time series $\boldsymbol{\rho}$ from undersampled Fourier measurements. The proposed work has similarities with structured matrix priors introduced to exploit various signal properties, including finite support and smoothly varying phase [17], piecewise smooth continuous domain images [60], and continuous domain wavelet sparsity [27]. Similar structured low rank priors have also appeared in the recovery of calibrationless multichannel data [71] and multi-shot diffusion weighted images [44]. However, none of the above 2-D methods are designed to exploit the smooth exponential structure of the 3-D dataset.

The exponential parameters usually vary from pixel to pixel and since they depend on the underlying physiology, it is very unlikely that they will vary in an arbitrary fashion. Hence we assume them to vary smoothly across the spatial locations. This fact enables us to jointly exploit the linear predictability of the exponential signals at all the spatial locations to derive a Fourier domain convolution relation between the 3-D Fourier data corresponding to the image series $\boldsymbol{\rho}$ and a 3D FIR filter $d[\mathbf{k}, n]$:

$$\widehat{\rho}[\mathbf{k}, n] \otimes d[\mathbf{k}, n] = 0 \tag{1.4}$$

The above convolution relation can be compactly written as:

$$\mathcal{T}(\widehat{\rho})\mathbf{d} = 0 \tag{1.5}$$

where $\mathcal{T}$ is a linear operator that maps a 3-D dataset $\widehat{\boldsymbol{\rho}}$ into a lifted matrix $\mathcal{T}(\widehat{\boldsymbol{\rho}}) \in \mathbb{C}^{m \times s}$. The construction of the matrix is illustrated in Fig. 1.2. Similarly $\mathbf{d}$ represents the vectorized 3-D filter $d[\mathbf{k}, n]$. The number of the columns of the matrix is given by the product of the dimensions of the filter while the number of rows corresponds to the number of valid linear convolutions between $\widehat{\boldsymbol{\rho}}$ and the filter. We observe that

$\mathcal{T}(\widehat{\boldsymbol{\rho}})$ has a multi-fold Toeplitz structure since (1.5) corresponds to a 3-D convolution. From (1.5), we observe that the Toeplitz matrix is rank deficient by one since $\mathbf{d}$ is in its null space. In fact, in the next chapter we show that $\mathcal{T}(\widehat{\rho})$ has a much larger null space and is low rank. We exploit this low rank property to recover the time series of images $\boldsymbol{\rho}$ by solving optimization problems of the form:

$$\widehat{\boldsymbol{\rho}}^{\star} = \arg\min_{\widehat{\boldsymbol{\rho}}} \|\mathcal{T}(\widehat{\boldsymbol{\rho}})\|_p + \frac{\mu}{2}\|\mathcal{A}(\widehat{\boldsymbol{\rho}}) - \mathbf{b}\|_2^2 \tag{1.6}$$

where μ is a regularization parameter and $\|.\|_p$ is the Schatten p norm. The direct implementation of the above problem involves the formation and storage of a large Toeplitz matrix, which increases computational complexity. In this thesis, we propose novel approximations to solve the above problem efficiently for different applications.

We note that the proposed work shares some similarities with Prony's method. Specifically, in both cases the annihilation relations are derived by exploiting the exponential behavior of the signal. Despite the similarity, we note that Prony's method cannot be applied to our setting since the $k-t$ Fourier samples corresponding to $\boldsymbol{\rho}$ are sampled at non-uniform locations; i.e. the samples are not at contiguous locations. Also in the proposed work we jointly exploit the exponential structure at all pixel locations, while Prony's method works by exploiting the exponential behavior independently.

1.4 MRI applications

In this thesis, we employ the ideas presented in the previous section to solve problems arising in various MRI applications. Next, we briefly describe the problems along with the proposed approaches to solve them.

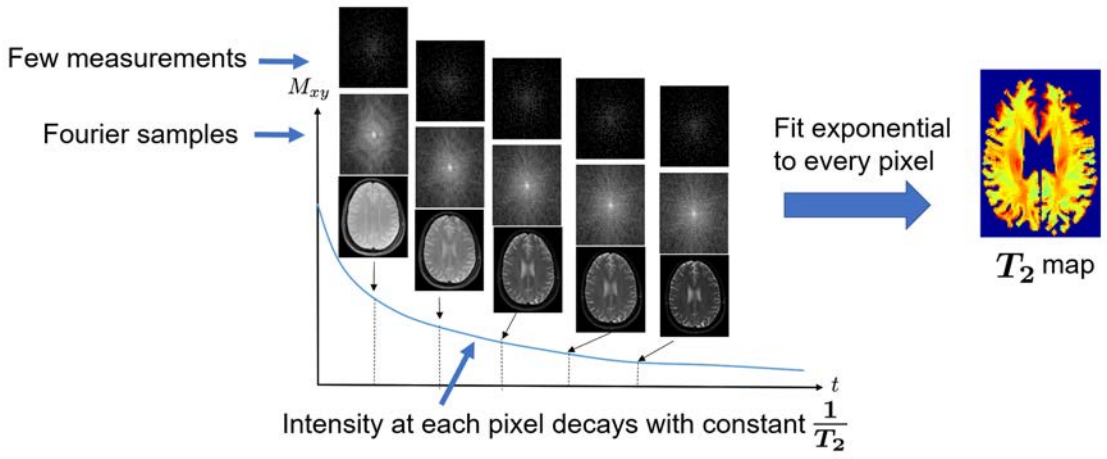

Figure 1.3: Accelerated MR parameter mapping: In the illustration, five images are acquired at different echo times. The temporal profile at each pixel follows an exponential decay, characterized by the damping constant ($\frac{1}{T_2}$) for that pixel. The goal is to estimate the T_2 value at each pixel location. To reduce the scan time, only few Fourier samples are acquired per image. After image recovery from these samples, an exponential is fitted at every pixel to estimate its T_2 value.

1.4.1 MR parameter mapping

In MR parameter mapping, the goal is to estimate a spatial map of parameters from a series of images, which are acquired at different sampled time points of the exponential curve. As these maps are indicative of the underlying tissue microstructure or metabolism, they are often used as bio-markers for various pathologies including neuro-degenerative and cardiovascular disorders. However, to get an accurate estimate of the maps, we need to acquire a large number of high spatial resolution images which in turn increases the scan time significantly. One of the ways to speed up the acquisition is by acquiring very few measurements. The recovery of images is then posed as an optimization problem, which is regularized by sparsity, smoothness or low rank priors [7, 12, 14, 24, 33, 64, 77, 79–82]. An illustration of the idea behind MR parameter mapping is shown in Fig. 1.3.

In this thesis, we derive an annihilation relation in the Fourier domain by exploiting the exponential structure of the signal at every pixel location along with the smoothness of the exponential parameters. This relation can be compactly written in terms of a Toeplitz matrix, formed from the $k-t$ Fourier samples. We show that this matrix has a low rank structure, which we exploit to recover the time series of images from undersampled measurements. We employ an iterative re-weighted least squares based algorithm [47], which alternates between the update of a weight matrix and recovery of images. The straightforward implementation of the algorithm is computationally expensive due to the formation and storage of the Toeplitz matrix. To alleviate this challenge, we introduce novel Fourier domain approximations which enable us to solve the problem very efficiently; the approximations eliminate the need to form and store the Toeplitz matrix resulting in a fast algorithm. We demonstrate the validity of the algorithm on a multi-channel human data and show improved reconstructed images and maps over those obtained from state-of-the-art methods. Part of this work was presented at ISBI 2015 [3] and was extended to result in a journal manuscript [4].

1.4.2 Field map (B0) compensation

MR images acquired using acquisition trajectories with long read outs are often susceptible to off-resonance related artifacts, resulting due to inhomogeneities in the main magnetic field (B0). Here we focus on developing an algorithm for field map compensation for data acquired using both Cartesian (Echo Planar Imaging) and non-Cartesian (Rosette) trajectories.

1.4.2.1 Cartesian trajectories: Echo Planar Imaging (EPI)

Echo Planar Imaging (EPI) is a fast MR imaging scheme for acquiring Fourier data in a single shot. EPI acquisitions are widely used to reduce scan time in applications including diffusion MRI and parameter mapping [65]. However the long read out

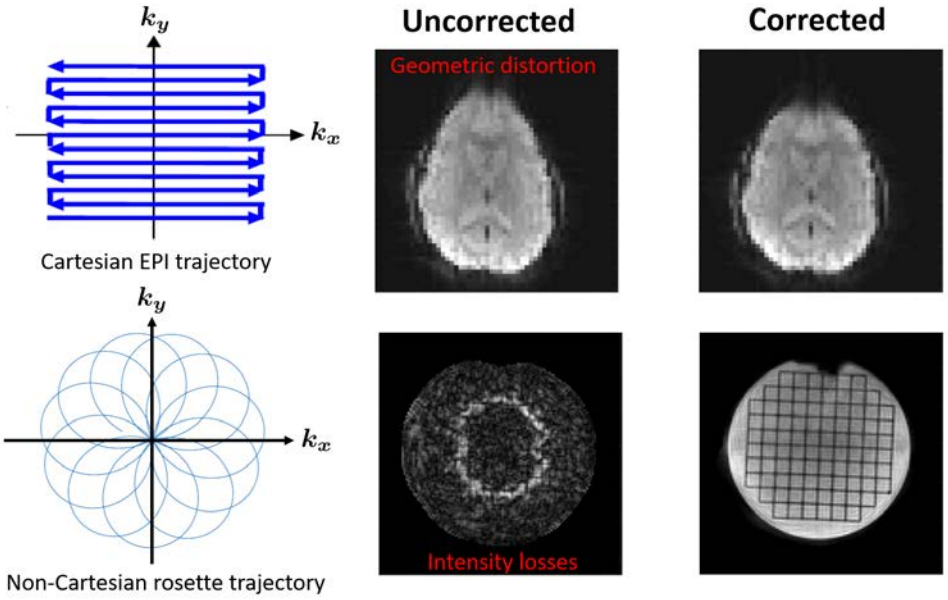

Figure 1.4: Field inhomogeneity induced artifacts for different trajectories: Images obtained using Cartesian acquisitions with long read outs have geometric distortion artifacts as shown above. For the Rosette trajectory, the artifacts manifest themselves in the form of severe intensity losses. The corrected images are shown for reference.

associated with EPI makes it susceptible to off-resonance related geometric distortion artifacts, which result from B0 inhomogeneities. This is illustrated in Fig. 1.4. These inhomogeneities arise due to the susceptibility difference between air, tissue and bone. Typically in many applications these low resolution EP images, which reflect some functional detail, are registered with high resolution anatomical images. However, the distortion artifacts in EPI leads to poor correspondence between the two sets of images, resulting in poor data interpretation.

In this work, we introduce a novel two-step structured low rank algorithm to compensate for field inhomogeneity artifacts in EPI. For this purpose we combine information from two EPI acquisitions and adopt a time segmentation approach [53] to transform the field map compensation problem to the recovery of an image time

series from highly undersampled measurements. Upon recovery, the distortion-free image corresponds to the first image of the series. We assume that the temporal profile at each pixel follows a single exponential, which is characterized by the field map and T_2^*. Using similar ideas as in the case of parameter mapping application, we derive an annihilation relation between the $k-t$ samples corresponding to the volume and a 3D FIR filter. This relation can be compactly represented in terms of a Toeplitz matrix, whose property is exploited to recover the missing entries of the volume. To reduce the memory demand and computational complexity of the algorithm, we introduce novel approximations which eliminate the need to store the large Toeplitz matrix. We demonstrate the algorithm on a numerical brain phantom, MR spherical phantom and two human datasets and show that the artifacts are significantly reduced compared to the uncorrected images. This work resulted in a journal manuscript [5].

1.4.2.2 Non-Cartesian trajectories: Rosette

Rosette trajectory was first proposed in [36] and was re-introduced in [52] for spectrally selective imaging. It has been applied in many applications such as functional MRI (fMRI), spectroscopy and fat/water imaging. The function generating the trajectory consists of a rapid one dimensional oscillating sinusoid, which is modulated by a complex exponential. The trajectory goes through the origin and intersects itself many times. This results in significant de-phasing throughout the Fourier space, leading to loss of image intensity. This is illustrated in Fig. 1.4.

To correct the off-resonance related intensity losses, we extend the structured low rank framework developed for EPI. The reformulation using time segmentation approach generates a volume with lot of missing entries. In contrast to the EPI setting, here the undersampling pattern in each frame of the time series is highly incoherent with respect to the other frames. This favours a compressed sensing based algorithm to be employed for the recovery of images. Hence we adopt an IRLS based algorithm, similar to the one for MR parameter mapping. We designed the

rosette trajectory and acquired MR phantom datasets in the 3T MR scanner. We demonstrated the algorithm on these datasets and showed that the intensity losses were significantly reduced.

1.4.3 Dynamic MRI reconstruction

Dynamic MRI is a very useful imaging modality to study the structure and function of different organs such as heart, lungs, abdomen etc. However, there are inconvenient trade offs in Dynamic MRI, especially in achieving high spatio-temporal resolution and good slice coverage simultaneously due to the slow nature of the acquisition process. In particular, cardiac MRI is especially challenging due to the presence of both cardiac and respiratory motion. One of the ways to alleviate the challenges is to perform the imaging in the breath-held mode. However many critically ill patients find it difficult to sustain long breath-holds. To address this challenge, we focus on shortening the required breath-hold duration by acquiring fewer samples. We can then pose the recovery of the images from their undersampled measurements as an regularized optimization problem.

Here, we propose to develop an algorithm to recover the dynamic image series by modeling it as a piece-wise constant function in three dimensions. We assume that the partial derivatives or edge sets of the images coincide with the zero crossings of a band-limited trigonometric polynomial. This implies that the signal can be annihilated by a set of finite impulse response filters in the Fourier domain. The annihilation relations result in a structured matrix formed from the weighted Fourier coefficients. Such a matrix will have a Toeplitz/Hankel structure and will be low rank. We propose to enforce this low rank prior to fill in the missing Fourier entries. We introduce novel Fourier domain approximations which result in a fast and memory efficient algorithm.

Note that in contrast to the previous applications, here we employ a piece-wise constant model and derive the appropriate annihilation relations. Yet, we present it

as part of this thesis since the algorithm proposed here closely resembles the algorithm for the parameter mapping application.

1.5 Contributions

1. **Exponential recovery using structured low rank matrix priors** We derive a structured low rank matrix prior by exploiting the exponential behavior at every pixel location along with the smoothness of the parameters. Even though structured matrix priors are being employed in many MRI applications, none of them exploit the smooth exponential structure of the 3D dataset. In this work, we exploit the low rank property of the matrix and recover the exponential image time series from undersampled measurements. We introduce novel Fourier domain approximations which results in a fast and memory efficient algorithm. Though the algorithm is demonstrated for MR parameter mapping application, it is general enough to be applied to other applications. The forward model, which reflects how the measurements are acquired needs to be modified accordingly.

2. **Accelerated MR parameter mapping** The algorithm developed for exponential signal recovery was demonstrated in the context of MR parameter mapping. Specifically, we solved the optimization problem to recover the time series of images from highly undersampled Fourier measurements. Once the images were estimated, we fitted a mono-exponential signal model at every pixel location to obtain a spatial map of the relaxation constant T_2. We compared the proposed reconstructions and maps to those obtained from state-of-the-art methods and showed significant improvements. The competing methods exploit different structures present in the images and enforce priors such as sparsity, low rankness and linear predictability of exponential signal. The structured matrix prior proposed in this work can be thought to qualitatively combine all of the

above-mentioned priors into a single prior.

3. **Calibration-less field (B0) map compensation**

   We propose a two-step structured low rank method to compensate for B0 inhomogeneities in EPI data. Even though structured low rank methods have been developed for many applications, none of them are applicable for field inhomogeneity compensation in EPI. We reformulate the field inhomogeneity correction of the 2-D EP image as the recovery of a 3D (2D + time) dataset from highly undersampled measurements. This reformulation allows us to use a structured low rank prior, which is designed to exploit the exponential structure present in the 3-D dataset, to recover it. To the best of our knowledge, this approach has not been adopted before for field inhomogeneity compensation in EPI. We introduce fast alternatives to current two-step nullspace based approaches [60], [17], [58] to significantly reduce the computational complexity and memory demand of the algorithm. We demonstrate the algorithm on phantom and human datasets and show that the artifacts are significantly reduced compared to the single shot uncorrected images.

   We extend the structured low rank framework for EPI data to the data acquired using rosette trajectory. The reformulation results in a volume with very few measurements in each frame; the sampling pattern corresponding to these frames are incoherent with respect to each other. This enables us to use an iterative compressed sensing algorithm to recover the missing entries. This approach has never been employed in the context of field map compensation for rosette data. We also designed the rosette trajectory using the GE's Multi-Nuclear Spin (MNS) package and used it to acquire data. We demonstrate the algorithm on MR phantom datasets and show that the proposed reconstructions have fewer artifacts.

4. **Accelerated cardiac MRI**

   Many compressed sensing schemes employ sparsity and smoothness priors to regularize the image recovery problem. However these schemes are not able to use other structural information such as smoothness present in the edges etc, which could improve the recovery at higher accelerations. In many 2D MRI applications, structured matrix priors based algorithms are shown to perform better than conventional sparsity and smoothness priors based algorithms. However extension of these algorithms to multidimensional imaging applications is very difficult due to the huge memory demand and high computational complexity. In this work, we introduce a structured matrix prior for accelerating cardiac MRI. We develop a fast and memory efficient algorithm that addresses the aforementioned issues on memory and speed and enables us to work with these very large structured matrices. Specifically, we introduce novel approximations which enables us to use these powerful matrix priors in the recovery of cardiac MRI data from under-sampled Fourier measurements. We demonstrate the algorithm on a cardiac breath-held data and show improved reconstructions over sparsity and smoothness based methods.

1.6 Organization

Chapter 2 introduces a structured low rank matrix based algorithm for the recovery of MR parameter maps from under-sampled Fourier measurements. This is demonstrated on human brain data. In chapter 3, we develop a framework to solve the problem of field inhomogeneity compensation for EPI acquisitions. The developed scheme is demonstrated on both phantom and human data. We extend this technique to non-Cartesian rosette trajectories in chapter 4. We designed a trajectory to acquire phantom data, and used it to demonstrate our algorithm. In chapter 5, we develop a scheme for accelerating breath-held dynamic cardiac MR imaging, using similar structured low rank based ideas. The algorithm is demonstrated on

human data and compared to other traditional compressed sensing based techniques. Finally, we summarize our work and present possible future extensions in chapter 6.

CHAPTER 2
ACCELERATED MR PARAMETER MAPPING

2.1 Introduction

Recovering parameters of a linear combination of damped exponentials is a problem of high significance in many MR imaging applications, including MR parameter mapping [8,76], MR spectroscopy [11], and fat/water imaging [20]. The objective is to estimate from a series of MR images the spatial maps of the exponential parameters, which are indicative of the underlying tissue microstructure or metabolism. These maps are often used as bio-markers for pathologies including neuro-degenerative and cardiovascular disorders [8, 11, 76]. Current approaches involve acquiring multiple images by sampling the exponential signals at different points, followed by a pixel-by-pixel fitting of the exponential model to estimate the parameters. However, the main challenge with these schemes is the long acquisition time, resulting from the need to acquire a large number of high spatial resolution images. Recently, several researchers have considered compressive sensing methods for recovering images from under-sampled Fourier measurements using priors which enforce sparsity, smoothness and low-rankness [7, 12, 14, 24, 33, 64, 77, 79–82].

The recovery of exponential parameters from few uniform samples of a linear combination of exponentials is a classical and well researched problem in signal processing [72]. The model has been extended to include a large class of signals with finite rate of innovation or finite number of discontinuities in [35, 78]. The early work in this direction focussed on the uniform sampling setting, where the linear dependencies between the samples of the signal translated to an "annihilation relationship". This implies that the signal can be nulled by the convolution with a finite impulse response filter. Recently, several researchers have extended the framework to recover a linear combination of undamped sinusoids from a few non-uniform Fourier samples [9, 17, 60]. These methods compactly represent the annihilation relation as a

product of a Hankel matrix formed from the signal samples and a vector of annihilation filter coefficients. With this reformulation, the Hankel matrix can be shown to be low-rank; the low-rank property can be enforced to complete the matrix from its non-uniform measurements.

In this work, we introduce a structured matrix completion algorithm for recovering a series of MR images from their non-uniformly under-sampled Fourier measurements, where the signal along the parameter dimension at every pixel is described by a linear combination of damped exponentials. We also assume that the exponential parameters vary smoothly in space. We observe that this model is general enough to account for many applications, including MR spectroscopy, parameter mapping, and diffusion MRI. For example, in MR parameter mapping, the signal along the parameter dimension could vary as a function of echo time, repetition time, and/or spin-lock duration. Here, we consider the single parameter setting for simplicity. We exploit the exponential behavior at every pixel, along with the smoothness of the parameters in the spatial dimensions, to derive an annihilation relation in the $k-t$ domain; t denotes the parameter dimension. These 3-D convolution relations can be compactly represented using a multi-fold Toeplitz matrix formed from the $k-t$ samples. We show that this matrix has a large null space, and hence is low rank. We enforce the low rank property of the structured matrix as a prior to recover the missing entries from the under-sampled Fourier measurements. The spatial smoothness as well as the number of exponentials in the model can be controlled by the rank of the Toeplitz matrix, which is in-turn dependent on the regularization parameter.

The straightforward implementation of the above structured Toeplitz matrix recovery scheme is associated with huge memory demand and high algorithmic complexity. Specifically, the size of the Toeplitz matrix is often several orders of magnitude greater than the size of the multidimensional signal. We introduce an algorithm based on a half-circulant approximation of the Toeplitz matrix, which eliminates the

need for the explicit evaluation and storage of the structured matrix. This work is a generalization of our recent work [61], where we introduced the GIRAF (Generalized Iterative Reweighted Annihilating Filter) algorithm for recovering the missing entries of a Toeplitz/Hankel matrix, when only few of its entries are observed. The approximation of linear convolutions by circular convolutions enabled an efficient implementation of the algorithm using Fast Fourier transforms (FFTs). The circulant approximation in [61] is valid when the signal samples decay rapidly towards the boundaries. This scheme is not directly applicable in our setting, since the signal samples have significant magnitude at the first few points along the parameter dimension. We modify the GIRAF algorithm and adopt a hybrid approach to solve the problem. Specifically, we perform the 3-D linear convolution as a series of 2-D circular convolutions along the spatial dimensions and linear convolution along the parameter dimension. Such a modification allows us to apply our algorithm on large scale multi-dimensional exponential estimation problems. The preliminary version of this work is accepted as a conference paper [3]. Compared to the work [3], the theoretical and algorithmic frameworks are further developed here, in addition to the application of the problem to the recovery of single and multi-channel T_2 weighted images.

The proposed method has similarities with structured matrix priors introduced to exploit various signal properties, including finite support and smoothly varying phase [17], piece-wise smooth continuous domain images [60], and continuous domain wavelet sparsity [27]. Similar structured low rank priors have also appeared in the recovery of calibrationless multichannel data [71] and multi-shot diffusion weighted images [44]. However, none of the above 2-D methods are designed to exploit the smooth exponential structure of the 3-D dataset. In [31], a Hankel matrix is constructed by exploiting the temporal smoothness using a Fourier transform and the spatial redundancies are exploited using a wavelet transform; the exponential struc-

ture of the temporal signal is not taken into account. In addition, the recovery of each $k_y - t$ slice is performed independently, assuming Cartesian sampling. The exponential structure of the signal is exploited in [63] and [49], where a Hankel matrix is constructed at every pixel by exploiting the linear predictability of the exponential time series. Since the linear combination of pixel-wise structured low rank priors is not capable of exploiting the similarities between the pixels in the dataset, the authors additionally use low rank and joint sparsity penalties on the Casorati matrix; see section II.D for more details. The proposed formulation enables the joint exploitation of the spatial correlations as well as the exponential structure, thereby mitigating the need for additional spatial priors; this approach is computationally more efficient and requires fewer free regularization parameters.

2.1.1 Notation

We collect the different notations used through out this chapter and describe them in this section for easy reference. Unless otherwise mentioned, bold upper-case letters $\mathbf{X}$ and bold lower-case letters $\mathbf{y}$ are used to represent matrices and vectors respectively; $[\mathbf{y}]^T$, $[\mathbf{X}]^T$ represent a transpose of the vector $\mathbf{y}$ and matrix $\mathbf{X}$ respectively. We denote a function that is dependent on $\mathbf{r}$ and n by $x[\mathbf{r}, n]$. The collection of function values for all possible values of $\mathbf{r}$ and n are denoted by the vector $\mathbf{x}$. The discrete Fourier transform of x is denoted by $\hat{x}$, while the vector corresponding to the function values is denoted by $\hat{\mathbf{x}}$. We use non-bold lower-case greek alphabets such as μ, α to represent constants. Upper-case greek alphabets Λ, Θ represent index sets containing the support of the coefficients of the filter and Fourier data; $|\Lambda|$ is used to denote the size of the set Λ. We denote the 2D and 3D convolution by $*$ and $\otimes$ respectively. The calligraphic letters (e.g. $\mathcal{A}, \mathcal{T}$) denote operators. For example, $\mathcal{A}$ is the forward operator that models the image acquisition as in (2.2), while $\mathcal{T}$ is a lifting operator that constructs a multi-fold Toeplitz structured matrix $\mathcal{T}(\hat{\boldsymbol{\rho}})$ from the entries of $\hat{\boldsymbol{\rho}}$.

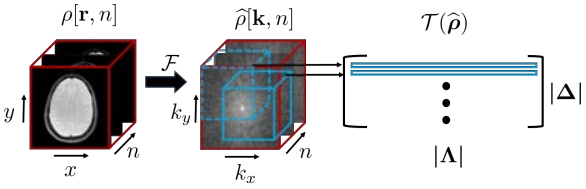

(a) Construction of the Toeplitz matrix $\mathcal{T}(\widehat{\boldsymbol{\rho}})$ of dimension $|\Delta| \times |\Lambda|$.

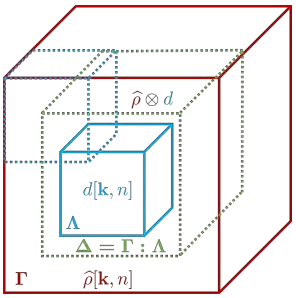

(b) Illustration of the index sets for the construction of Toeplitz matrix.

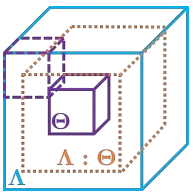

(c) Illustration of the index sets for the minimal and assumed filters.

Figure 2.1: (a) Illustration of the construction of the matrix $\mathcal{T}(\widehat{\boldsymbol{\rho}})$ from the dataset $\widehat{\boldsymbol{\rho}}$: The rows of the Toeplitz matrix correspond to the cuboid shaped neighborhoods of the Fourier samples. The number of columns is equal to the size of the filter support ($|\Lambda|$). Similarly, the number of rows is equal to the number of valid linear convolutions between $\widehat{\rho}$ and the filter, denoted by Δ. b) Illustration of the relation between the filter and signal supports and the matrix dimensions: The Fourier samples $\widehat{\rho}[\mathbf{k}, n]$ and the filter coefficients $d[\mathbf{k}, n]$ are assumed to be supported on the rectangular sets Γ and Λ, respectively. The 3-D convolution between them is valid in the dotted rectangular region (in green) and the set of valid indices is represented by $\Delta = \Gamma : \Lambda$. c) The rectangular sets containing the coefficients of the minimal and assumed filters are represented by Θ and Λ respectively. The number of linearly independent null space vectors of $\mathcal{T}(\widehat{\boldsymbol{\rho}})$ is given by all possible valid shifts of Θ in Λ, denoted by $\Lambda : \Theta$; this implies that $\mathcal{T}(\widehat{\boldsymbol{\rho}})$ is low rank and we enforce this property to estimate the missing entries of the matrix.

2.2 Recovery using annihilation relations

2.2.1 Measurement model

We consider the recovery of a series of images $\boldsymbol{\rho}$ from its multichannel Fourier measurements $\mathbf{b}$. The multichannel Fourier data $\widehat{\boldsymbol{\rho}}_i$ corresponding to the i^{th} image frame can be modeled as

$$\mathbf{b}_{ij} = \underbrace{\mathbf{S}_i \mathbf{F} \mathbf{C}_j \mathbf{F}^*}_{\mathbf{A}_{ij}} \widehat{\boldsymbol{\rho}}_i + \boldsymbol{\eta}_{ij}, \;\; j = 1 \ldots N_{coils} \tag{2.1}$$

where $\mathbf{b}_{ij}$ and $\boldsymbol{\eta}_{ij}$ are the under-sampled Fourier measurements and zero mean white gaussian noise corresponding to the i^{th} frame and j^{th} coil respectively, $\mathbf{C}_j$ is the receiver coil sensitivity of the j^{th} coil, $\mathbf{S}_i$ is the sampling mask for the i^{th} frame and $\mathbf{F}$ is the 2D discrete Fourier transform (DFT) matrix. (2.1) can be compactly written as

$$\mathbf{b} = \mathcal{A}(\widehat{\boldsymbol{\rho}}) + \boldsymbol{\eta} \tag{2.2}$$

where $\widehat{\boldsymbol{\rho}} = [\widehat{\boldsymbol{\rho}}_1, \widehat{\boldsymbol{\rho}}_2, \ldots \widehat{\boldsymbol{\rho}}_T] \in \mathbb{C}^{B\times T}$ is the Fourier data in Casorati matrix form [34] with the i^{th} column representing the vector of Fourier data at time instant t_i. $\mathcal{A}$ is a linear operator representing Fourier under-sampling and multiplication of coil sensitivities with $\widehat{\boldsymbol{\rho}}$.

2.2.2 Annihilation property of smooth exponentials

We model the signal at the spatial location $\mathbf{r} = (x, y)$ as a linear combination of L exponentials:

$$\rho[\mathbf{r}, n] = \sum_{i=1}^{L} \alpha_i(\mathbf{r})\ \beta_i(\mathbf{r})^n, \tag{2.3}$$

where $\alpha_i(\mathbf{r}) \in \mathbb{C}$ are the amplitudes, $\beta_i(\mathbf{r}) \in \mathbb{C}$ is the exponential parameter that is dependent on the underlying physiology, n refers to the signal index along the parameter dimension and L is the number of exponentials at the voxel. For instance, in T_2 mapping applications the exponential parameters at the pixel location indexed by $\mathbf{r}$ are given by $\beta_i(\mathbf{r}) = \exp\left(\frac{-\Delta T}{T_{2,i}(\mathbf{r})}\right)$. Here ΔT is the difference in echo times between two frames and $T_{2,i}$ is the relaxation parameter of the i^{th} tissue component (e.g. gray matter, CSF or white matter).

The exponential signal, described in (5.1), at each pixel location can be annihilated by a 1-D FIR filter $g[\mathbf{r}, n]$ [72]:

$$\sum_{m=0}^{L} \rho[\mathbf{r}, m]\ g[\mathbf{r}, n-m] = 0, \quad \forall \mathbf{r}. \tag{2.4}$$

where (3.4) represents a 1-D convolution between the signal $\rho[\mathbf{r}, n]$ and the $L+1$ tap filter $g[\mathbf{r}, n]$. Since the exponential parameters vary from pixel to pixel, the filter $g[\mathbf{r}, n]$ also varies with the spatial location $\mathbf{r}$.

In practice, the exponential parameters vary smoothly as a function of space. This implies that the coefficients of the filter $g[\mathbf{r}, n]$ can be assumed to be smooth functions of the spatial variable $\mathbf{r}$. Taking the 2-D Fourier transform of (3.4) along the spatial dimensions, we obtain the following annihilation relation in the Fourier domain:

$$\widehat{\rho}[\mathbf{k}, n] \otimes d[\mathbf{k}, n] = 0. \tag{2.5}$$

where $\widehat{\rho}[\mathbf{k}, n] \overset{\mathcal{F}_{2D}}{\leftrightarrow} \rho[\mathbf{r}, n]$ and $d[\mathbf{k}, n] \overset{\mathcal{F}_{2D}}{\leftrightarrow} g[\mathbf{r}, n]$ are the spatial Fourier coefficients of $\rho[\mathbf{r}, n]$ and $g[\mathbf{r}, n]$, respectively. Here, $\otimes$ denotes 3-D convolution.

Since the filter coefficients of $g[\mathbf{r}, n]$ vary smoothly as a function of space, we assume $d[\mathbf{k}, n]$ to be a 3-D FIR filter, whose coefficients are support limited in the rectangular set $\Lambda \subset \mathbb{Z}^3$; the size of Λ (spatial bandwidth of $d[\mathbf{k}, n]$) controls the spatial smoothness of the parameters, while the bandwidth along the parameter dimension is dependent on the number of exponentials in the signal model.

We focus on the recovery of the Fourier coefficients of the signal specified by $\widehat{\boldsymbol{\rho}}$ within the rectangular set $\Gamma \subset \mathbb{Z}^3$. For simplicity, we assume $\widehat{\boldsymbol{\rho}}$ has T frames, each of dimension $P \times Q$. The set Γ is illustrated by the red cuboid in Fig. 2.1.(b). The 3-D convolution (2.5) can be compactly written as

$$\mathcal{T}(\widehat{\boldsymbol{\rho}})\, \mathbf{d} = 0 \tag{2.6}$$

where $\mathcal{T}$ is a linear operator that maps a 3-D dataset $\widehat{\boldsymbol{\rho}}$ into a lifted matrix $\mathcal{T}(\widehat{\boldsymbol{\rho}}) \in \mathbb{C}^{m \times s}$. The construction of the matrix is illustrated in Fig. 2.1.(a). Similarly $\mathbf{d}$ represents the vectorized 3-D filter $d[\mathbf{k}, n]$. Here, $s = |\Lambda|$ is the number of the columns of the matrix, where Λ denotes the support of the filter d indicated by the blue cuboid

in Fig. 2.1.(b). The number of rows in the matrix is denoted by $m = |\Gamma : \Lambda|$, which corresponds to the number of valid linear convolutions between $\widehat{\boldsymbol{\rho}}$ and the filter; the convolutions are valid in the green dotted cuboid in Fig. 2.1.(b). The set $\Gamma : \Lambda$ is specified by

$$\Gamma : \Lambda = \{\mathbf{v} \mid \Lambda + \mathbf{v} \subseteq \Gamma; \mathbf{v} \in \mathbb{Z}^3\}. \tag{2.7}$$

The blue dotted cuboid in Fig. 2.1.(b) indicates a valid shift of the blue solid cuboid, whose support is given by Λ. We observe that $\mathcal{T}(\widehat{\boldsymbol{\rho}})$ has a multi-fold Toeplitz structure since the matrix-vector product in (2.6) corresponds to a 3-D convolution.

2.2.3 Dimensions of the fundamental subspaces of $\mathcal{T}(\widehat{\rho})$

We denote the index set of the filter with the smallest support (termed as the minimal filter), which satisfies the annihilation relation, to be Θ. In practice, the support Θ (denoted by the purple cuboid in Fig. 2.1.(c) is unknown. In such cases, the support set of the filter is overestimated to Λ, such that $\Theta \subset \Lambda$. Let the dimensions of Λ be $N_1 \times N_2 \times M$.

When the size of the filter is overestimated to Λ, it will result in multiple linearly independent vectors $\mathbf{d}$ in the null space of $\mathcal{T}(\widehat{\boldsymbol{\rho}})$. Specifically, if $c[\mathbf{k}, n]$ is the minimal filter, then any FIR filter of the form

$$d[\mathbf{k}, n] = c[\mathbf{k}, n] \otimes e[\mathbf{k}, n] \tag{2.8}$$

will also satisfy the following annihilation relation $\hat{\rho}[\mathbf{k}, n] \otimes d[\mathbf{k}, n] = 0$, or equivalently $\mathcal{T}(\widehat{\boldsymbol{\rho}})\mathbf{d} = 0$. Here, $e[\mathbf{k}, n]$ is any FIR filter such that $d[\mathbf{k}, n]$ is support limited to Λ. The number of such filters ($d[\mathbf{k}, n]$) is specified by the set of all valid shifts of Θ in Λ, denoted by $\Lambda : \Theta$ [60]; this set is indicated by the orange cuboid in Fig. 2.1.(c). The corresponding shifted filters are linearly independent [60].

The above discussion shows that the dimension of the kernel of $\mathcal{T}(\widehat{\boldsymbol{\rho}})$ is at least

$|\Lambda : \Theta|$. i.e.,

$$\dim\Big(\ker\left(\mathcal{T}\left(\widehat{\boldsymbol{\rho}}\right)\right)\Big) \geq |\Lambda : \Theta| \tag{2.9}$$

where Λ is the assumed filter size and $|\Lambda : \Theta|$ denotes the cardinality of the set $\Lambda : \Theta$. By the rank-nullity theorem, the rank of $\mathcal{T}\left(\widehat{\boldsymbol{\rho}}\right)$ or the dimension of the image space of $\mathcal{T}\left(\widehat{\boldsymbol{\rho}}\right)$ is specified by

$$\operatorname{rank}\Big(\mathcal{T}\left(\widehat{\boldsymbol{\rho}}\right)\Big) = \dim\Big(\operatorname{im}\left(\mathcal{T}\left(\widehat{\boldsymbol{\rho}}\right)\right)\Big) \leq |\Lambda| - |\Lambda : \Theta|. \tag{2.10}$$

Consider two datasets $\widehat{\boldsymbol{\rho}}_1$ and $\widehat{\boldsymbol{\rho}}_2$, where the size of Θ (purple cuboid in Fig. 2.1.(c)) is smaller for $\widehat{\boldsymbol{\rho}}_2$. Note that a smaller minimal filter corresponds to a dataset with fewer exponentials and smoother parameters. Since the number of valid shifts indicated by the set $|\Lambda : \Theta|$ is higher for the dataset $\widehat{\boldsymbol{\rho}}_2$, we have $\operatorname{rank}(\mathcal{T}(\widehat{\boldsymbol{\rho}}_2)) < \operatorname{rank}(\mathcal{T}(\widehat{\boldsymbol{\rho}}_1))$. Hence, the rank of the Toeplitz matrix can be used as a measure of complexity of the dataset.

Since we expect the matrix $\mathcal{T}(\widehat{\boldsymbol{\rho}})$ to be low rank, we use the rank prior as well as the Toeplitz structure of the matrix to recover the exponential image series from under-sampled Fourier measurements. The support of the different index sets along with the construction of the Toeplitz matrix is illustrated in Fig. 2.1.

2.2.4 Structured low rank recovery from few measurements

Since (2.2) is an ill-posed problem, we employ the structured low rank matrix prior proposed in the previous sub-sections for the recovery of missing Fourier samples. We formulate the recovery of the Fourier data $\hat{\rho}$ from the under-sampled measurements $\mathbf{b}$ as the following structured matrix completion problem:

$$\min_{\widehat{\boldsymbol{\rho}}} \ \operatorname{rank}\left[\mathcal{T}(\widehat{\boldsymbol{\rho}})\right] \ \text{such that} \ \mathbf{b} = \mathcal{A}(\widehat{\boldsymbol{\rho}}) + \boldsymbol{\eta} \tag{2.11}$$

Since the problem specified in (2.11) is NP hard, we relax the rank function with a Schatten p $(0 \leq p \leq 1)$ norm. The relaxed objective function is then given by

$$\widehat{\boldsymbol{\rho}}^{\star} = \arg\min_{\widehat{\boldsymbol{\rho}}} \|\mathcal{T}(\widehat{\boldsymbol{\rho}})\|_p + \frac{\mu}{2}\|\mathcal{A}(\widehat{\boldsymbol{\rho}}) - \mathbf{b}\|_2^2 \tag{2.12}$$

where μ is a regularization parameter that balances the weight given to the Schatten norm of the matrix and the data consistency term in (2.12). $\mathcal{T}(\widehat{\boldsymbol{\rho}}) \in \mathbb{C}^{m\times s}$ is a multifold Toeplitz matrix formed from the Fourier samples $\widehat{\boldsymbol{\rho}}$. $\|\mathbf{X}\|_p$ is the Schatten p norm, defined as $\|\mathbf{X}\|_p := \frac{1}{p}\mathrm{Tr}[(\mathbf{X}^H\mathbf{X})^{\frac{p}{2}}] = \frac{1}{p}\mathrm{Tr}[(\mathbf{X}\mathbf{X}^H)^{\frac{p}{2}}] = \frac{1}{p}\sum_i \sigma_i^p$; σ_i are the singular values of $\mathbf{X}$. When $p = 1$, the Schatten norm reduces to the convex nuclear norm and for $(0 \leq p < 1)$, the Schatten norm is a non-convex penalty; When $p \to 0$, $\|\mathbf{X}\|_p := \sum_i \log \sigma_i$. In section 2.3, we will focus on the algorithm to solve the optimization problem (2.12).

2.2.5 Relation to pixel-wise structured low rank priors

The recovery of MR parameter weighted images considered in [63] is closely related to the proposed work. In [63], the sum of structured low rank priors, formed at every pixel, is considered. Specifically, for every pixel, a Hankel matrix is constructed using the temporal signal at that pixel. The images are reconstructed by exploiting the low rank structure of all these matrices. The objective function is specified by

$$\{\bar{\boldsymbol{\rho}}_m\} = \arg\min_{\bar{\boldsymbol{\rho}}} \sum_{i=1}^{l} \mathrm{rank}[\mathcal{T}(\bar{\boldsymbol{\rho}}(\mathbf{r}_i))], \text{ such that } \mathcal{A}(\bar{\boldsymbol{\rho}}) = \mathbf{b} \tag{2.13}$$

where $\bar{\boldsymbol{\rho}}_m$ is the set of images to be recovered, l is the total number of pixels, $\mathcal{A}$ is a linear operator and $\mathbf{b}$ is a vector of measurements.

We now consider a special case of our setting, where the spatial dimensions of Λ (assumed filter size) are the same as that of the dataset (i.e. $P = N_1$ and $Q = N_2$), which is related to the above model. Since the spatial dimensions of the filter are

the same as the dataset, no spatial smoothness is assumed on the annihilation filter coefficients. In this case, the dimension of the Toeplitz matrix $\mathcal{T}(\boldsymbol{\rho})$, where $\boldsymbol{\rho}$ is a signal of interest, is specified by $(T - M + 1) \times (N_1 \cdot N_2 \cdot M)$. The Toeplitz matrix after a re-arrangement of the columns has the following structure:

$$\mathcal{T}(\boldsymbol{\rho}) = \Big(\ \mathcal{T}(\boldsymbol{\rho}(\mathbf{r}_1)) \ \Big| \ \mathcal{T}(\boldsymbol{\rho}(\mathbf{r}_2)) \ \Big| \ \ldots \ \Big| \ \mathcal{T}(\boldsymbol{\rho}(\mathbf{r}_l)) \ \Big) \tag{2.14}$$

In (2.14), each of the Toeplitz matrices $\mathcal{T}(\boldsymbol{\rho}(\mathbf{r}_i)) \in \mathbb{C}^{(T-M+1)\times M}$, whose entries correspond to the temporal signal at location $\mathbf{r}_i$. We observe that enforcing a low rank prior on the special case considered in (2.14) results in a more constrained approach than the pixel-wise low rank penalty in (2.13). In particular, the global low-rank prior considered in (2.14) enables the exploitation of correlations between the columns of $\mathcal{T}(\boldsymbol{\rho})$, in addition to the annihilation relations. In contrast, the pixel-wise approach in (2.13) is not capable of exploiting these correlations. An additional low-rank prior on the Casorati matrix of the images or a wavelet prior has to be used as in [63] to exploit these correlations. Since the special case of our formulation is already capable of exploiting these correlations, we do not require additional priors. More importantly, we consider spatially bandlimited filters, which account for the smoothness of the exponential parameters. We observe that this property offers a 3 dB improvement (see Table 2.1) over the special case considered in (2.14). In summary, the structured low-rank prior considered in this work qualitatively consolidates and unifies the multiple diverse priors used in [63].

Another key benefit of the above special case is the reduced computational complexity. When an iterative re-weighted least squares (IRLS) based approach [47] is employed, each step of the algorithm (2.13) requires the eigen decomposition of as many Gram matrices as pixels in the dataset. In contrast, the use of the prior (2.14) requires the eigen decomposition of only one Gram matrix at each iteration.

As the dimension of the Gram matrices in both the cases is the same and equal to $(T-M+1)\times(T-M+1)$, the computational complexity of the special case is orders of magnitude lower than that of the pixel-wise structured low rank strategy.

2.3 Optimization algorithm

The minimization of (2.12) using classical low-rank matrix recovery schemes is challenging due to the large size of the structured matrix, which often requires several orders of magnitude more memory, when compared to the original 3-D dataset. Current structured low-rank methods [17, 27] employ approaches originally designed for low-rank matrix recovery and do not exploit the structure of the matrix; the direct use of these 2-D algorithms to our 3-D setting is difficult due to the large memory demand and computational complexity.

We modify the GIRAF algorithm [61] to the 3-D setting to minimize the computational complexity. Specifically, we employ an IRLS based algorithm [47] to solve the optimization problem in (2.12). This approach allows us to use efficient approximations for operations involving the Toeplitz matrix using fast Fourier transforms; these modifications quite significantly reduce the computational complexity and memory demand. To derive the basic idea of the algorithm, we use the following identity to express the Schatten p norm of a matrix as a weighted Frobenius norm:

$$\|\mathbf{Y}\|_p = \frac{1}{p}\mathrm{Tr}[\underbrace{(\mathbf{Y}\mathbf{Y}^*)^{\frac{p}{2}-1}}_{\mathbf{H}}\mathbf{Y}\mathbf{Y}^*] \tag{2.15}$$

$$= \frac{1}{p}\|\mathbf{H}^{\frac{1}{2}}\mathbf{Y}\|_F^2 \tag{2.16}$$

Hence the solution to the minimum Schatten norm can be obtained by alternating between the update of a weight matrix $\mathbf{H}$ and the solution to a weighted least squares problem. In our case, we set $\mathbf{Y} = \mathcal{T}(\widehat{\boldsymbol{\rho}})$ in (2.15), which decouples (2.12) into two

sub-problems. At the n^{th} iteration, the sub-problems are given by

$$\widehat{\boldsymbol{\rho}}^{(n)} = \arg\min_{\widehat{\boldsymbol{\rho}}} \|(\sqrt{\mathbf{H}})^{(n-1)}\, \mathcal{T}(\widehat{\boldsymbol{\rho}})\|_F^2 + \frac{\mu p}{2}\|\mathcal{A}(\widehat{\boldsymbol{\rho}}) - \mathbf{b}\|_2^2 \tag{2.17}$$

$$\mathbf{H}^{(n)} = [\underbrace{\mathcal{T}(\widehat{\boldsymbol{\rho}}^{(n)})\, \mathcal{T}(\widehat{\boldsymbol{\rho}}^{(n)})^*}_{\mathbf{R}} + \epsilon^{(n)}\, \mathbf{I}]^{\frac{p}{2}-1} \tag{2.18}$$

where $\epsilon^{(n)} \to 0$ is added to stabilize the inverse. Hence to solve (2.12), we employ an alternating minimization scheme that cycles between the sub-problems (2.17) and (2.18) till the cost of (2.12) between successive iterates is below a tolerance threshold. In the next two sub-sections, we describe an efficient implementation of the two sub-problems.

2.3.1 Least squares solution

Let the rows of $\sqrt{\mathbf{H}}$ be denoted by $\left[(\mathbf{h}^{(1)})^T, \ldots, (\mathbf{h}^{(M)})^T\right]^T$. Substituting for $\sqrt{\mathbf{H}}$ in (2.17), we obtain

$$\widehat{\boldsymbol{\rho}}^* = \arg\min_{\widehat{\boldsymbol{\rho}}} \sum_{i=1}^{M} \|\mathbf{h}^{(i)}\, \mathcal{T}(\widehat{\boldsymbol{\rho}})\|_2^2 \;+\; \frac{\mu p}{2}\, \|\mathcal{A}(\widehat{\boldsymbol{\rho}}) - \mathbf{b}\|_2^2 \tag{2.19}$$

The term $\mathbf{h}^{(i)}\, \mathcal{T}(\widehat{\boldsymbol{\rho}})$ in (2.19) represents a 3-D linear convolution between the 3-D sequences $\mathbf{h}^{(i)}$ and $\widehat{\boldsymbol{\rho}}$.

In the GIRAF algorithm [61], the linear convolutions were approximated by circular convolutions, so that they could be efficiently implemented using Fast Fourier transforms (FFTs). The approximations were valid due to the rapid decay of the Fourier coefficients towards the boundaries. However, in our case as the signal at every voxel follows an exponential curve, the magnitude of the Fourier coefficients are high at the first few points along the parameter dimension. Hence, the direct application of the GIRAF scheme to our setting gives poor results.

We introduce a hybrid strategy to improve the approximations, while keeping the

memory demand and computational complexity low. In particular, we approximate the 3-D linear convolution as a series of 2-D circular convolutions along the spatial dimensions and a linear convolution along the parameter dimension. Denoting the l^{th} frame of $\widehat{\boldsymbol{\rho}}$ and h as $\widehat{\rho}_l[\mathbf{k}]$ and $h_l[\mathbf{k}]$ respectively, we rewrite the convolution relation as

$$\begin{aligned} h[\mathbf{k},n] \otimes \widehat{\rho}[\mathbf{k},n] &= \sum_m \sum_{\mathbf{p}} \widehat{\rho}[\mathbf{k}-\mathbf{p}, n-m]\, h[\mathbf{p},m] \\ &= \sum_m \underbrace{\sum_{\mathbf{p}} \widehat{\rho}_{n-m}[\mathbf{k}-\mathbf{p}]\, h_m[\mathbf{p}]}_{g_{n-m,m} = \widehat{\rho}_{n-m} \,*\, h_m}, \end{aligned} \tag{2.20}$$

where $\otimes$ denotes 3-D convolution and $*$ denotes 2-D convolution. Since the spatial Fourier coefficients of $\widehat{\rho}[\mathbf{k}]$ decay rapidly towards the boundaries, the 2-D linear convolutions $g_{j,l} = \hat{\rho}_j \;*\; h_l$ can be approximated as 2-D circular convolutions and efficiently computed using fast Fourier transforms as shown in [61]. After the 2-D convolutions are evaluated for all feasible combinations $g_{j,l}$, we compute the outer sum.

Now, we express the aforementioned idea in compact matrix notations. Let $\mathbf{h}$ and $\hat{\rho}$ consist of M and T frames respectively. We consider an arbitrary filter h of spatial dimensions $N_1 \times N_2$ and denote its i^{th} frame by $\mathbf{h}_i$. Now $(\mathbf{h}\, \mathcal{T}(\widehat{\boldsymbol{\rho}}))$ can be expanded as,

$$\mathbf{h}\, \mathcal{T}(\widehat{\boldsymbol{\rho}}) = \begin{pmatrix} \mathbf{h}_M & \dots & \mathbf{h}_1 \end{pmatrix} \begin{pmatrix} \mathbf{T}(\widehat{\boldsymbol{\rho}}_1) & .. & \mathbf{T}(\widehat{\boldsymbol{\rho}}_{T-M+1}) \\ \vdots & \vdots & \vdots \\ \mathbf{T}(\widehat{\boldsymbol{\rho}}_M) & .. & \mathbf{T}(\widehat{\boldsymbol{\rho}}_T) \end{pmatrix} \tag{2.21}$$

In the above equation, $\mathbf{T}(\widehat{\boldsymbol{\rho}}_j)$ represents a Toeplitz matrix formed from the samples of $\widehat{\boldsymbol{\rho}}_j$. This matrix can be expressed in terms of a larger circulant matrix [61] in the following way:

$$\mathbf{T}(\widehat{\boldsymbol{\rho}}_j) \approx \mathbf{P}^*_{\Lambda_s}\, \mathbf{C}(\widehat{\boldsymbol{\rho}}_j) \tag{2.22}$$

Here $\mathbf{C}(\widehat{\boldsymbol{\rho}}_j) \in \mathbb{C}^{L\times L}$ is a circulant matrix formed from the Fourier samples $\widehat{\boldsymbol{\rho}}_j$, Λ_s is the support of a frame of the filter and $\mathbf{P}^*_{\Lambda_s} \in \mathbb{C}^{N_1N_2\times L}$ corresponds to zero padding operation outside the filter support Λ_s. Note that the support of $\mathbf{h}_l$ is often much smaller than that of $\widehat{\boldsymbol{\rho}}_j$.

Using the approximation in (2.22), we can efficiently evaluate $\mathbf{h}_l\ \mathbf{T}(\widehat{\boldsymbol{\rho}}_j)$, which is the 2-D linear convolution between the l^{th} frame of $\mathbf{h}$ and j^{th} frame of $\widehat{\boldsymbol{\rho}}$, as

$$\begin{aligned} \mathbf{h}_l\ \mathbf{T}(\widehat{\boldsymbol{\rho}}_j) &\approx \mathbf{h}_l\ \mathbf{P}^*_{\Lambda_s}\ \mathbf{C}(\widehat{\boldsymbol{\rho}}_j) \\ &= \left[\widehat{\boldsymbol{\rho}}_j\right]^T \underbrace{\mathbf{C}(\mathbf{h}_l\ \mathbf{P}^*_{\Lambda_s})}_{\mathbf{C}_l}. \end{aligned} \tag{2.23}$$

where we have used the commutative property of convolution to arrive at the expression in (2.23). Here, $\mathbf{C}_l = \mathbf{C}(\mathbf{h}_l\mathbf{P}^*_{\Lambda_s})$ is a circulant matrix formed from the zero padded filter coefficients $\mathbf{h}_l$. Hence, the product $\left[\widehat{\boldsymbol{\rho}}_j\right]^T \mathbf{C}_l$ denotes the 2-D circular convolution between $\left[\widehat{\boldsymbol{\rho}}_j\right]^T$ and the zero-padded filter coefficients.

We propose to implement the circular convolutions using fast Fourier transforms to minimize the computational complexity. Specifically, we compute (2.23) efficiently as

$$\left[\widehat{\boldsymbol{\rho}}_j\right]^T \mathbf{C}_l = \left[\widehat{\boldsymbol{\rho}}_j\right]^T \underbrace{\mathbf{F}^*\mathbf{D}_l\mathbf{F}}_{\mathbf{C}_l} \tag{2.24}$$

where $\mathbf{D}_l$ is a diagonal matrix with diagonal entries $\mu_l \overset{\mathcal{F}_{2D}}{\leftrightarrow} \mathbf{h}_l\ \mathbf{P}^*_{\Lambda_s}$ and $\mathbf{F}$ denotes the 2-D discrete Fourier transform matrix.

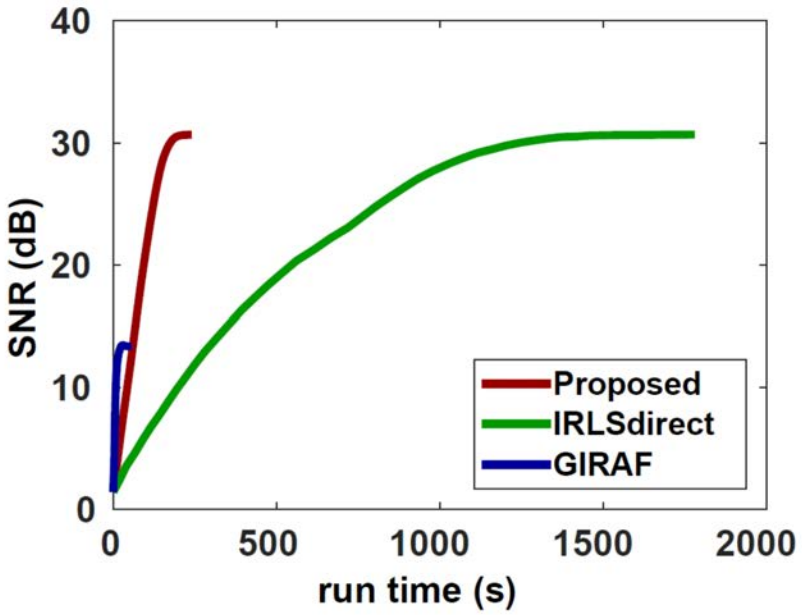

Figure 2.2: Effect of approximations on the run time of the proposed algorithm and comparison of SNR: The approximations introduced in the proposed method enable efficient computation of the sub-problems (2.17) and (2.18) using fast Fourier transforms (FFTs). This results in a faster convergence (7.5 fold speed up) to the same solution as the one obtained using the IRLS (direct) method.

Using (2.24), we simplify (2.21) as,

$$\mathbf{hT}(\widehat{\boldsymbol{\rho}}) \approx [\widehat{\boldsymbol{\rho}}]^T \mathbf{Q}^* \underbrace{\begin{pmatrix} \mathbf{D}_M & \cdots & & \mathbf{0} \\ \mathbf{D}_{M-1} & \mathbf{D}_M & & \vdots \\ \vdots & \vdots & \ddots & \\ \mathbf{D}_1 & \cdots & & \mathbf{0} \\ \mathbf{0} & \mathbf{D}_1 & & \mathbf{D}_M \\ \vdots & \vdots & \cdots & \vdots \\ \mathbf{0} & \mathbf{0} & \cdots & \mathbf{D}_1 \end{pmatrix}}_{[\mathbf{D}(\mathbf{h})]^T} \mathbf{Q}$$

where each of the matrices $\mathbf{D}_l$ are diagonal matrices and the dimension of $\mathbf{D}(\mathbf{h})^T$ is $PQT \times PQk$ with $k = T - M + 1$. Here, $[\widehat{\boldsymbol{\rho}}]^T = [\widehat{\boldsymbol{\rho}}_1, \ldots, \widehat{\boldsymbol{\rho}}_T]^T$ and $\mathbf{Q}^* = \mathbf{I} \bigotimes \mathbf{F}^*$ is a block diagonal matrix with the diagonal blocks being the inverse 2-D Fourier

transform matrix. Thus, we can express $\|\mathbf{h}\ \mathbf{T}(\widehat{\boldsymbol{\rho}})\|^2$ as $\|\mathbf{D}(\mathbf{h})\mathbf{Q}^*\ \widehat{\boldsymbol{\rho}}\|^2$.

Using the above relation and substituting for the first term in (2.19) we obtain,

$$\widehat{\boldsymbol{\rho}}^* = \arg\min_{\widehat{\boldsymbol{\rho}}} \sum_{i=1}^{M} \|\mathbf{D}(\mathbf{h}^{(i)})\mathbf{Q}^*\widehat{\boldsymbol{\rho}}\|_2^2 + \frac{\mu p}{2}\|\mathcal{A}(\widehat{\boldsymbol{\rho}}) - \mathbf{b}\|_2^2 \tag{2.25}$$

The above equation can be solved by taking its gradient and setting it to zero. The gradient is given by

$$2\mathbf{Q}\underbrace{\left(\sum_{i=1}^{M}(\mathbf{D}(\mathbf{h}^{(i)}))^*\mathbf{D}(\mathbf{h}^{(i)})\right)}_{\mathbf{G}}\mathbf{Q}^*\widehat{\boldsymbol{\rho}} + \mu p\ \mathcal{A}^*\mathcal{A}\widehat{\boldsymbol{\rho}} = \mu p\ \mathcal{A}^*\mathbf{b} \tag{2.26}$$

Note that prior to solving (2.26), $\mathbf{G}$ can be precomputed efficiently. Denote $\mathbf{E}^* = [\mathbf{D}_M, \mathbf{D}_{M-1} \ldots, \mathbf{D}_1]$. In order to populate the entries of $(\mathbf{D}(\mathbf{h}^{(i)}))^*\mathbf{D}(\mathbf{h}^{(i)})$, we need to compute one product $(\mathbf{E}\mathbf{E}^*)^{(i)}$, and the sum of $k = (T - M + 1)$ sparse matrices. Each sparse matrix contains a shifted version of $(\mathbf{E}\mathbf{E}^*)^{(i)}$ as the only non-zero block. After precomputing $\mathbf{G}$, we only need a few iterations of conjugate gradient (cg) algorithm to solve (2.26).

2.3.2 Weight update

The first step in computing the weight matrix $\mathbf{H}^{\frac{1}{2}}$ involves forming the Gram matrix $\mathbf{R} = \mathcal{T}(\widehat{\boldsymbol{\rho}})\,\mathcal{T}(\widehat{\boldsymbol{\rho}})^*$. The direct computation of $\mathbf{R}$ requires the evaluation and storage of the lifted matrix $\mathcal{T}(\widehat{\boldsymbol{\rho}})$, which will be a computationally expensive and memory intensive operation. Instead we propose an efficient way to compute the

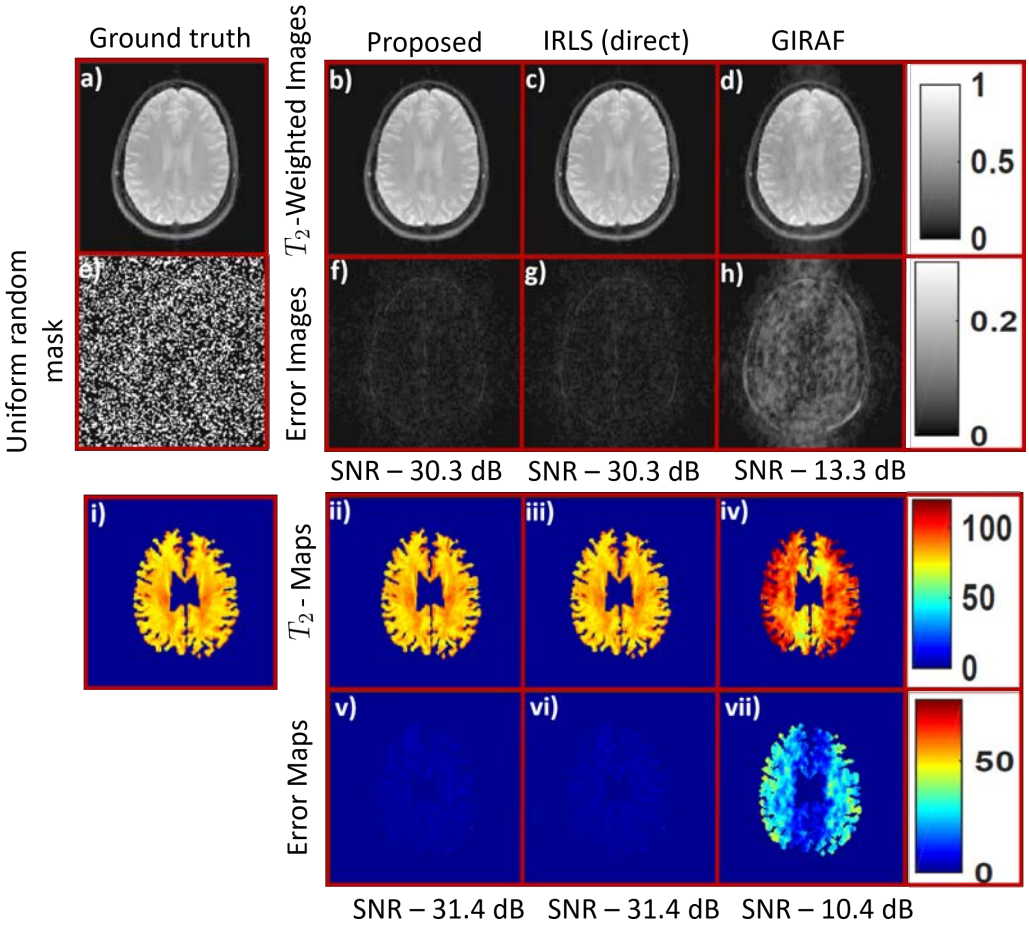

Figure 2.3: Effect of approximations introduced in the proposed method on the recovery of coil combined T_2 weighted images from 30 percent uniform random Fourier measurements: One frame (4th Echo, TE = 40ms) of the image sequence corresponding to the ground truth is shown in (a) along with the frame of the sampling mask in (e). The 4th echo of the reconstructed image sequence using proposed method (b) is compared with those obtained using IRLS (direct) in (c) and GIRAF in (d). The corresponding error images are shown in (f)-(h). The estimated T_2 maps, which were multiplied by a mask to remove the background and the CSF region, are shown in (i)-(iv) and the corresponding error maps are shown in (v)-(vii).

Gram matrix. Specifically, we assume $\mathbf{R}$ to be partitioned in the following way:

$$\begin{pmatrix} \mathbf{R}_{1,1} & \mathbf{R}_{1,2} & \dots & \mathbf{R}_{1,M} \\ \mathbf{R}_{2,1} & \mathbf{R}_{2,2} & \dots & \mathbf{R}_{2,M} \\ \vdots & \vdots & \dots & \vdots \\ \vdots & \vdots & \dots & \vdots \\ \mathbf{R}_{M,1} & \mathbf{R}_{M,2} & \cdots & \mathbf{R}_{M,M} \end{pmatrix} \tag{2.27}$$

Algorithm 1: Proposed algorithm for the recovery of exponential image time series

Initialize $\widehat{\boldsymbol{\rho}}^{(0)}$ and choose $\epsilon^{(0)} > 0$;
for $n = 1$ *to* N_{max} *or tolerance threshold reached* **do**
  Step1: Weight matrix update:
    Compute each block $\mathbf{R}_{p,q}$ of the Gram matrix $\mathbf{R}$ using (2.28) and (2.29);
    Compute the eigen values and eigen vectors $\{\lambda^{(i)}, \mathbf{u}^{(i)}\}_{i=1}^{M}$ from the eigen decomposition of $\mathbf{R}$;
    Evaluate the null space vectors:
      $\mathbf{h}^{(i)} = \sqrt{\alpha_i}(\mathbf{u}^{(i)})^*$, where $\alpha^{(i)} = (\lambda^{(i)} + \epsilon^{(n-1)})^{\frac{p}{2}-1}$;
  Step2: Least Squares update:
    Solve the least squares problem:
      $\widehat{\boldsymbol{\rho}}^{(n)} = \arg\min_{\widehat{\boldsymbol{\rho}}} \sum_{i=1}^{M} \|\mathbf{D}(\mathbf{h}^{(i)})\mathbf{Q}^*\widehat{\boldsymbol{\rho}}\|_2^2 + \frac{\mu p}{2}\|\mathcal{A}(\widehat{\boldsymbol{\rho}}) - \mathbf{b}\|_2^2$
    using Conjugate gradient (CG) method;
  Choose $\epsilon^{(n)}$ such that $0 < \epsilon^{(n)} \leq \epsilon^{(n-1)}$;
end

where the above matrix has M column and row partitions and $\mathbf{R}_{i,j}$ is a matrix block of dimension $N_1N_2 \times N_1N_2$. We obtain a general expression for the matrix block corresponding to the p^{th} row and q^{th} column partition of $\mathbf{R}$ as

$$\mathbf{R}_{p,q} = \sum_{i=1}^{k} \mathbf{T}(\widehat{\boldsymbol{\rho}}_{p+i-1})\mathbf{T}(\widehat{\boldsymbol{\rho}}_{q+i-1})^* \tag{2.28}$$

where $k := T - M + 1$. To compute $\mathbf{R}_{p,q}$, we use the relation in (2.22) and simplify $\mathbf{T}(\widehat{\boldsymbol{\rho}}_i)\mathbf{T}(\widehat{\boldsymbol{\rho}}_j)^*$ as

$$\mathbf{P}_{i,j} = \mathbf{T}(\widehat{\boldsymbol{\rho}}_i)\mathbf{T}(\widehat{\boldsymbol{\rho}}_j)^* = \mathbf{P}_{\Lambda_s}^* \underbrace{\mathbf{C}(\widehat{\boldsymbol{\rho}}_i)\mathbf{C}(\widehat{\boldsymbol{\rho}}_j)^*}_{\mathbf{C}(\mathbf{g})} \mathbf{P}_{\Lambda_s} \tag{2.29}$$

where the entries of $\mathbf{C}(\mathbf{g})$ are obtained from the array $\mathbf{g}$. The entries of $\mathbf{g}$ are given by $\mathbf{F}(\boldsymbol{\rho}_i \circ \text{conj}(\boldsymbol{\rho}_j))$, where $\boldsymbol{\rho}_i$ and $\boldsymbol{\rho}_j$ are the images corresponding to the Fourier samples $\widehat{\boldsymbol{\rho}}_i$ and $\widehat{\boldsymbol{\rho}}_j$ respectively, $\mathbf{F}$ denotes a 2-D DFT matrix, conj denotes the conjugate operation and $\circ$ denotes point-wise multiplication. Hence the entries of every row of $\mathbf{P}_{i,j}$ can be populated by performing a sliding window operation that extracts and vectorizes a $N_1 \times N_2$ patch from a $(2N_1 - 1) \times (2N_2 - 1)$ neighborhood.

Next the weight matrix $\mathbf{H}^{\frac{1}{2}}$ is efficiently computed from the eigen decomposition of $\mathbf{R}$. Let $\mathbf{U}$ represent the orthogonal basis of eigen vectors $\mathbf{u}^{(i)}$ and Λ be a diagonal matrix containing the eigen values $\lambda^{(i)}$. Then the eigen decomposition of $\mathbf{R}$ is given by $\mathbf{U}\Lambda\mathbf{U}^*$. Substituting for $\mathbf{R}$ in (2.18) and simplifying further we obtain,

$$\mathbf{H} = \left[\mathbf{U}(\mathbf{\Lambda} + \epsilon\mathbf{I})\mathbf{U}^*\right]^{\frac{p}{2}-1} = \mathbf{U}(\mathbf{\Lambda} + \epsilon\mathbf{I})^{\frac{p}{2}-1}\mathbf{U}^*.$$

Hence, one choice of the matrix square root $\mathbf{H}^{\frac{1}{2}}$ is

$$\mathbf{H}^{\frac{1}{2}} = (\mathbf{\Lambda} + \epsilon\mathbf{I})^{\frac{p}{4}-\frac{1}{2}}\mathbf{U}^* = \left[(\mathbf{h}^{(1)})^T, \ldots, (\mathbf{h}^{(M)})^T\right]^T$$

where $\mathbf{h}^{(i)} = \sqrt{\alpha^{(i)}}(\mathbf{u}^{(i)})^*$ and $\alpha^{(i)} = (\lambda^{(i)} + \epsilon)^{\frac{p}{2}-1}$.

2.3.3 Implementation details

The details of the alternating minimization algorithm to solve (2.17) and (2.18) are described in Algorithm (1). We initialize and vary the value of ϵ as described in [47]. Specifically, we initialize ϵ as $\epsilon^{(0)} = \lambda_{max}/100$, where λ_{max} is the largest eigen value of the gram matrix $\mathcal{T}(\widehat{\boldsymbol{\rho}}_{init})\mathcal{T}(\widehat{\boldsymbol{\rho}}_{init})^*$, which is formed from the initial guess $\widehat{\boldsymbol{\rho}}_{init} = \widehat{\boldsymbol{\rho}}^{(0)}$. Every iteration, we decrease the value of ϵ as $\epsilon^{(n)} = \epsilon^{(n-1)}/\gamma$, $\gamma > 1$. For all our experiments we set $\gamma = 1.4$. We run the optimization algorithm for different values of the regularization parameter μ and choose the value which results in the best signal to noise ratio (SNR), where SNR $:= 20\log\frac{\|\mathbf{X}_g\|_2}{\|\mathbf{X}_g - \mathbf{X_r}\|_2}$. Here $\mathbf{X_g}$ and $\mathbf{X_r}$ are the ground truth and the reconstructed images respectively. To observe the behavior of μ across different acceleration factors, we reconstructed images at different acceleration factors ranging from six to twelve. We observed that the optimal μ estimated was fairly constant across different acceleration factors. In the absence of ground truth data it is not possible to compute the SNR. Hence choosing the regularization parameter using the above-mentioned approach is not feasible. In

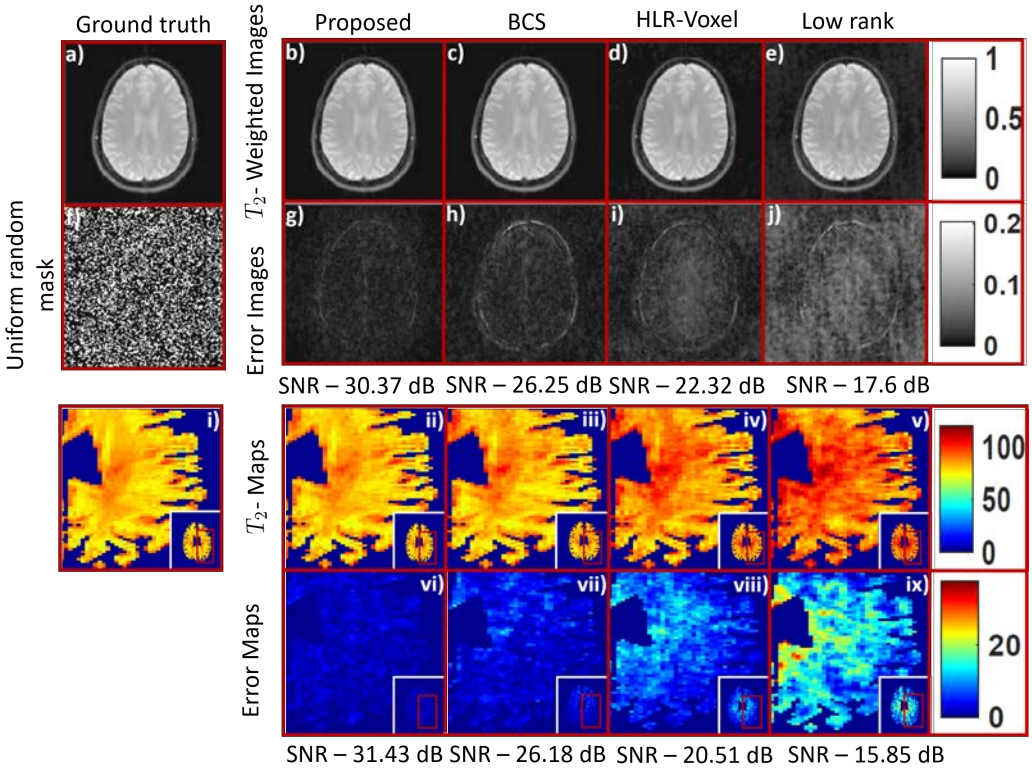

Figure 2.4: Comparison of the proposed method with different reconstruction schemes on the recovery of coil combined data from 30 percent uniform random Fourier measurements: One frame (4th Echo, TE = 40ms) of the image sequence is shown in (a)-(e) along with the frame of sampling mask in (f). The corresponding error images are shown in (g)-(j). The estimated T_2 maps, specifically the enclosed rectangular region is zoomed and is shown in (i)-(v) with the corresponding error maps shown in (vi)-(ix). Here the maps were multiplied by a mask to remove the background and the CSF region. The improvements offered by the proposed scheme can be easily appreciated from the T_2 error images and the estimated T_2 maps.

such cases, we could employ heuristic techniques such as the L-curve method [19] or more sophisticated methods [66,67], where risk functions approximating the SNR are used to estimate the optimal regularization parameter. We plan to investigate such techniques for the selection of regularization parameter in the future. We implemented the algorithm in MATLAB, which runs on a Linux workstation with a 3.6Ghz Intel Xeon CPU and 32GB RAM.

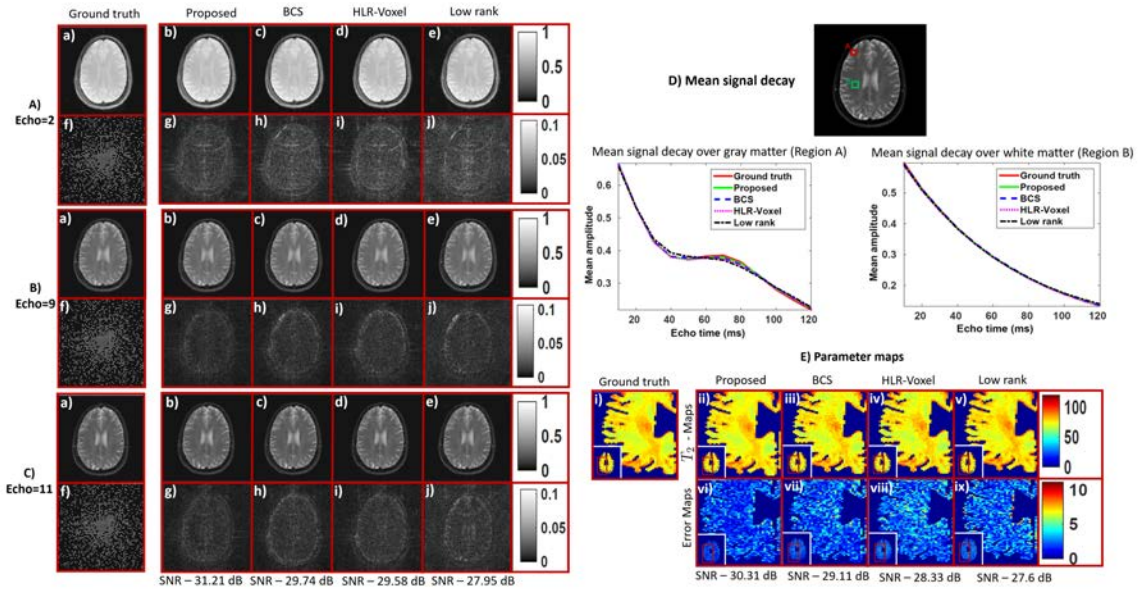

Figure 2.5: Comparison of the proposed method with different reconstruction schemes on the recovery of multi channel data at an acceleration factor of 12: In the first row of A), B) and C) three frames corresponding to 2nd Echo (TE=20ms), 9th Echo (TE=90ms) and 11th Echo (TE=110ms) are shown in (a)-(e) along with the frame of the sampling mask in (f). The corresponding error images are shown in (g)-(j) in the second row of A), B) and C). In D), the mean signal decay is plotted over a gray matter (Region A) and white matter (Region B) region for the ground truth and all the competing methods. The signal within the red ROI was corrupted due to some non-idealities in the acquisition. In E), the estimated T_2 maps, specifically the enclosed rectangular region is zoomed and is shown in (i)-(v) with the corresponding error maps shown in (vi)-(ix). Here the maps were multiplied by a mask to remove the background and the CSF region. We observe that the reconstructions from the proposed method have fewer errors, which can be appreciated from the error maps of the T_2 weighted images as well with the noise-like artifacts in the T_2 maps.

2.4 Results

We demonstrate our algorithm on a fully sampled axial 2-D dataset, which was acquired on a Siemens 3T Trio scanner with 12 coils using a turbo spin echo sequence. The scan parameters were: TR = 2500 ms, slice thickness = 5 mm, Matrix size = 128×128 and FOV = 22×22 cm^2. By varying the echo times (TE) from 10 to 120 ms, we acquired T_2 weighted images at twelve equispaced TE.

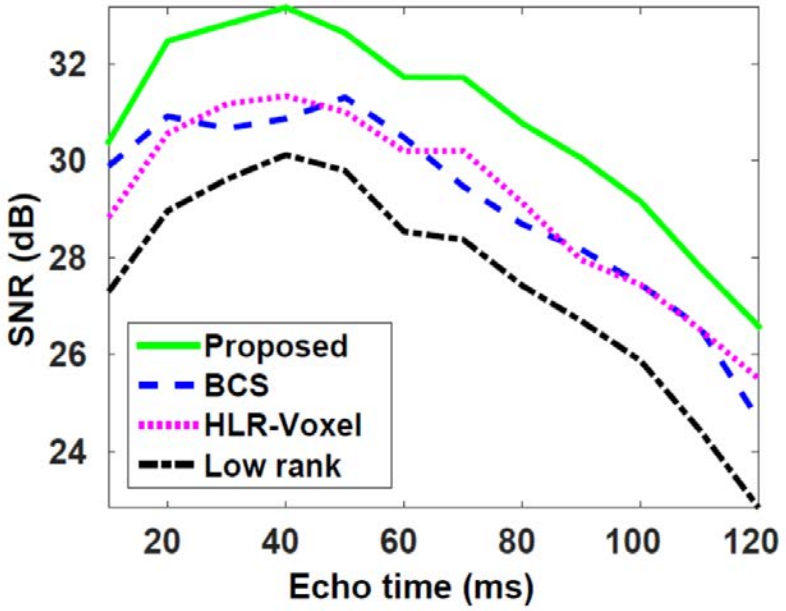

Figure 2.6: Plot showing the SNR of the reconstructions at all the echo times for the proposed and the competing methods.

2.4.1 State-of-the-art methods for comparison

We compare the proposed method with three state-of-the-art methods: $k-t$ low rank [37], blind compressed sensing (BCS) [7], and the pixel-wise structured low-rank prior in (2.13), which we refer to as HLR-Voxel. An IRLS algorithm [47] was employed to solve the nuclear norm minimization in (2.13). We compared the methods for both single and multi-channel recovery experiments.

We also demonstrate the improved speed up offered by the proposed scheme by comparing it with traditional IRLS as well as the multidimensional GIRAF algorithm [61]. For the traditional IRLS (direct) method, we solve (2.17) and (2.18) directly without introducing FFT based approximations. After the images are reconstructed, we estimate the T_2 maps by fitting a mono exponential model to every pixel.

2.4.2 Single channel recovery

We demonstrate the proposed method on the recovery of single channel T_2-weighted data from 30% uniform random measurements and compare it with the three aforementioned methods. To create the single channel data, we performed a principal component analysis (PCA) on the original multi-channel data and selected the most significant component to obtain a coil compressed data. For the proposed method, a filter of size $122 \times 122 \times 2$ was used to recover the images. The value of $p = 0.6$ for the Schatten norm was chosen for both the $k - t$ low rank and the proposed algorithm. The results from the different methods are shown in Fig. 2.4. We observe that the T_2 weighted images and the estimated T_2 maps from the proposed method have fewer errors and artifacts than the competing methods.

2.4.3 Multi-channel recovery

In Fig. 2.5, we compare the different methods on the recovery of multi-channel T_2-weighted data from twelve fold under-sampled Fourier measurements. The data was retrospectively under-sampled using a combination of uniform Cartesian and a pseudo-random variable density sampling patterns. Specifically, we uniformly under-sampled the x and y directions by a factor of 2 and refer this sampling mask as a 2×2 uniform Cartesian mask. To increase the incoherence between the frames, we also shifted every frame of the mask by zero or one unit (done randomly) along the x and y directions. We achieved an acceleration factor of twelve by combining the four fold uniform Cartesian mask with a three fold pseudo-random variable density undersampling pattern. Three frames of the sampling mask corresponding to the three echoes are shown in (f) in Fig. 2.5 A), B) and C). We used a Schatten $p = 0.7$ for both the proposed and the low rank methods. Also for the proposed method, a filter of size $102 \times 102 \times 10$ was used in the recovery of images. Reconstructions corresponding to three echos with TE = 20ms, TE = 90ms and TE = 110ms respectively and the T_2 maps for all the methods are shown in A) through C) and E) respectively

Table 2.1: Effect of filter size on SNR of T_2 weighted images.

(a) Varying spatial dimension

filter size	SNR
128x128x10	28.05
122x122x10	30.30
114x114x10	31.00
108x108x10	31.12
102x102x10	**31.21**
100x100x10	31.20

(b) Varying temporal dimensions

filter size	SNR (dB)
102x102x11	30.80
102x102x10	**31.21**
102x102x7	31.13
102x102x4	30.96
102x102x2	30.78
102x102x1	29.88

in Fig. 2.5. We observe that the T_2 weighted images from the proposed method have fewer errors than the competing methods. Also, the T_2 maps corresponding to the proposed method are a lot smoother and have fewer artifacts, especially in the enclosed rectangular region, than those obtained from the competing methods. In Fig. 2.5 D), we plot the mean signal decay over two regions of interests for all the methods. We observe that the signal corresponding to the proposed method matches closely to the ground truth signal in both cases. We also observe that the mean signal decay from the ROI (in red) in the gray matter is not exactly an exponential function. Nevertheless, the proposed signal model (5.1) approximates the signal as a linear combination of exponentials and captures the signal decay quite well. This suggests that the performance of the algorithm may degrade gradually, when the signal deviates from an exponential model. In Fig. (2.6), we plot the Signal to Noise ratio (SNR) of the reconstructions at each echo time for the proposed and the competing methods. We observe that for all the methods, the SNR increases for the first few echoes and then decreases for the remaining echoes, which could be due to non-ideal acquisition conditions. Nevertheless, the SNR of the images obtained from the proposed method is higher at all echo times, when compared to the state-of-the-art methods.

2.4.4 Effect of filter size on image recovery

We study the effect of filter size or equivalently the dimensions of the Toeplitz matrix on the SNR of the T_2-weighted images recovered from twelve fold under-sampled multi-channel Fourier data in Table 2.1. We study the effect of varying the spatial dimensions of the filter on the SNR in Table 2.1a. We observe that the filters with a smaller spatial support ($102 \times 102 \times 10$) provide improved results than larger filters, thus demonstrating the benefit of exploiting spatial smoothness. A filter with large spatial dimensions ($128 \times 128 \times 10$) fails to exploit any spatial smoothness. We demonstrate the benefit of exploiting the annihilation relations, which takes into account the exponential structure of the signal along the parameter dimension at every pixel, in 2.1b. We observe that a filter having multiple taps along the temporal dimension ($102 \times 102 \times 10$) results in reconstructions with a better SNR than those obtained using a filter with size ($102 \times 102 \times 1$), which just exploits joint sparsity. From these experiments, we also note that varying the spatial support of the filter has a higher impact on the SNR than the temporal support.

2.4.5 Effect of approximations on image recovery

We study the effect of the approximations, introduced in the proposed method, on the recovery of coil compressed T_2-weighted data from 30% uniform random Fourier measurements. We note that the approximations introduced in the proposed method enable efficient computation of the sub-problems (2.17) and (2.18) using Fast Fourier transforms (FFT). This results in a faster convergence to the solution when compared to the IRLS-direct method, as shown in Fig. 2.2. Specifically, we observe a 7.5 fold speed up due to the proposed algorithm. In Fig. 2.3, we observe that the T_2 weighted images and the T_2 maps corresponding to the proposed method have similar SNR and image quality compared to those obtained using the IRLS-direct method. These results demonstrate the effectiveness of the approximations introduced in the proposed method. From the figure, we also observe that the images and the maps obtained

from the GIRAF algorithm have a lot of errors and artifacts. This is because the approximations in the GIRAF algorithm break down in our setting thus resulting in poor T_2 estimates.

2.5 Discussion and conclusion

We introduced a novel structured matrix recovery algorithm to recover an image series with smoothly varying exponential parameters from under-sampled Fourier measurements. As the proposed method exploits the spatial smoothness of the parameters and the exponential structure of the signal along the parameter dimension at every pixel, it results in improved reconstructions over the other state-of-the-art methods. The comparisons on T_2 estimation problems in the context of MR parameter mapping demonstrate the potential of this scheme, with reduced errors in both the reconstructed images and T_2 maps compared to state of the art methods.

As the size of the filter is not known apriori, we treated it as an optimization parameter and chose the dimension that resulted in the best SNR. We observed that the spatial dimensions of the filter had a greater effect on the SNR than the temporal dimensions. Specifically, a filter with smaller spatial support ($102 \times 102 \times 10$) provided improved reconstructions with higher SNR than a filter of size $128 \times 128 \times 10$, which failed to incorporate any spatial smoothness. Hence as the proposed matrix prior incorporates spatial smoothness, it eliminates the need for additional spatial regularizers or priors to further constrain the image recovery. Similarly, the reconstructions using a filter with multiple taps along the temporal dimension ($102 \times 102 \times 10$) had higher SNR than the filter with one tap, which exploits the joint sparsity of the Casorati matrix formed from the Fourier samples. We also observed that for both the multi-channel and coil combined data, the filter sizes yielding reconstructions with highest SNR were different. The size of the filter reflects the complexity of the model which is usually dependent on the number of measured samples, number of coils etc. Since the model complexity is different for both the datasets, it resulted in

different sizes of the filter.

To solve the optimization problem, we employ an iterative least squares (IRLS) based strategy, which decouples the original problem into two sub-problems. We adopt a hybrid approach to keep the memory demand and computational complexity low. Specifically, we introduce novel approximations, which allow us to solve the sub-problems using FFTs. This resulted in a faster convergence to the same solution as the one obtained using the IRLS (direct) method. The proposed algorithm was approximately 7.5 times faster than the IRLS (direct) method. We also observed that the GIRAF algorithm broke down in our setting resulting in poor reconstructed images and T_2 maps.

The proposed framework may be extended to the multi-dimensional parameter setting. For instance, in MR parameter mapping, if the signal along the parameter dimension at every pixel varies as a function of both TR and TE, then the filter coefficients will be dependent on both exponential parameters T_1 and T_2. Hence, annihilation relations similar to (3.4) and (2.5) can be derived, which can be compactly represented using a low rank Toeplitz matrix. The low rank property of the Toeplitz matrix can then be enforced to recover the images from under-sampled Fourier measurements. We plan to investigate this problem in the future.

The results in Fig.(2.5).D indicate that the performance of the algorithm degrades gradually, when the voxel time profiles deviate from the exponential signal model. Specfically, such signals may be reasonably approximated as a linear combination of few exponentials. In addition, the use of the low-rank penalty that only requires the matrix to be approximately low-rank, rather than a low-rank constraint, also allows the signal to deviate from the exponential model. We did not account for the presence of artifacts due to stimulated echoes [6, 10, 22, 41, 42] which are formed when a turbo spin echo sequence is used. Further investigation is required to study the impact of such errors.

CHAPTER 3
FIELD MAP COMPENSATION FOR CARTESIAN TRAJECTORIES: DEMONSTRATING ON ECHO PLANAR IMAGING (EPI) DATA

3.1 Introduction

Echo Planar Imaging (EPI), which is a fast MR imaging scheme, is widely used to reduce scan time in applications including diffusion MRI and parameter mapping [65]. The capability to provide high temporal resolution makes EPI a popular choice in many dynamic MR imaging studies, including perfusion MRI [65] and imaging of the BOLD contrast in functional MRI (fMRI) [30]. In recent years, there has been a push towards achieving higher spatial and temporal resolution in many of these applications. However, the long read-out associated with EPI makes it particularly susceptible to off-resonance related geometric distortion artifacts, resulting from magnetic field (B0) inhomogeneities. B0 inhomogeneities arise primarily due to difference in magnetic susceptibility between air, tissue, and bone, which are particularly severe around the sinus and air canal regions. Field inhomogeneity results in phase modulation that is independent of imaging gradients and manifest as geometric distortions in the image; the poor correspondence of the EP images with high spatial resolution anatomical images makes it difficult to interpret the data.

The widely used solution is to reduce the duration of the readout using multi-shot strategies [2]. However, the readout duration has to be significantly reduced to bring distortions down to reasonable levels. This translates to a large number of shots resulting in increased scan time and motion sensitivity [2]. An alternative is to correct for the B0 distortion in EP images, which is a well-researched field [1, 13, 15, 21, 23, 25, 26, 28, 29, 40, 43, 48, 50, 53–55, 69, 70, 73, 74]. Current methods can be broadly classified as calibration-based or calibration-free algorithms. In calibration-based methods, a field map is estimated prior to the EPI scan [68], which is then used in the recovery of a distortion-free image. The reconstruction algorithms range from computationally efficient conjugate phase methods [40, 43, 53, 54, 69, 70]

to more sophisticated and computationally expensive model based reconstruction methods [15, 21, 48, 73]. The main challenge with calibration based methods is the mismatch between the estimated and the actual field map, resulting from patient motion, scanner drift and field inhomogeneity differences due to physiological changes such as respiration. To overcome these issues, calibration-less methods which jointly estimate the field map and the distortion-free image from the acquired data have been proposed [29, 50, 74]. An alternative strategy is image space correction using registration [1, 23], which can work with magnitude images acquired using two different sampling trajectories. The main challenge with the above calibration-less methods is the non-convex nature of the optimization algorithms, which translates to high computational complexity and risk of local minima.

In this work, we propose a fast calibration-free structured low rank framework for compensating field inhomogeneity artifacts in EPI. We combine the information from two EPI acquisitions, which differ in echo-time (TE). We reformulate the field inhomogeneity compensation of the 2-D EPI dataset as the the recovery of an image time series (2D+time dataset) from highly undersampled measurements. Upon recovery, the distortion-free image corresponds to the first image in the time series. We note that a similar strategy has been employed in the recent work of T_2 shuffling [75], even though the proposed algorithm and application are fundamentally different. In our work, the temporal intensity profile of each pixel is assumed to decay exponentially with a frequency and damping constant, which are dependent on the fieldmap and T_2^* value respectively at that pixel. We also assume that the exponential frequency shift and damping vary smoothly across space, which allows us to exploit the smooth nature of the B0 inhomogeneity. Under these assumptions, the $k-t$ space samples of the image time series can be annihilated by convolutions with several linearly independent finite impulse response filters, whose filter taps are dependent on the exponential parameters. The convolution between the signal and the filter can be

compactly represented as the product of a multi-fold Toeplitz matrix formed from the Fourier samples, with the vector of filter coefficients. The annihilation relations imply that the Toeplitz matrix has several linearly independent null space vectors and hence is low rank [3, 4]. We exploit the low rank property of this matrix to complete its missing entries and recover the image series.

The direct implementation of the above algorithm requires the evaluation and storage of a large multi-fold Toeplitz matrix, which is computationally expensive. Hence, we introduce a fast two-step approach to solve this problem. In the first step, we form a sub-matrix of the above Toeplitz matrix by selecting the fully sampled rows, and estimate the null space from it. Since this submatrix is an order of magnitude smaller than the original Toeplitz matrix, the first step has low memory demand and is computationally efficient. These null-space vectors are then used to recover the missing entries of the original Toeplitz matrix in the second step. Specifically, we seek a matrix that is orthogonal to the estimated null-space vectors, while satisfying data-consistency. To reduce the computational complexity of the second subproblem, we estimate the signal subspace by compactly representing the signal using an exponential signal model. This facilitates the easy estimation of the signal from its measurements. This approach reduces the number of effective unknowns to be solved and results in a very fast and efficient algorithm. It also eliminates the need to store the entries of the Toeplitz matrix. We demonstrate the effectiveness of the proposed approaches by performing simulations on a numerical brain phantom and also applying it on phantom and human data.

The proposed field inhomogeneity compensation scheme is an addition to the growing family of structured low rank methods for continuous domain compressed sensing [4, 17, 27, 57, 60, 61], parallel MRI [39, 71], calibration-free correction of multi-shot EPI data [44], correction of Nyquist ghost artifacts in EPI [32, 38, 46], parameter mapping [3, 4], and trajectory correction in radial acquisitions [45]. None of these

schemes are directly applicable to field inhomogeneity compensation in EPI. The novel contributions of this work are:

1. We reformulate the distortion correction of the 2-D EP image as the recovery of a 3D (2D + time) dataset from highly undersampled measurements. This reformulation allows us to use a structured low rank prior, which is designed to exploit the exponential structure present in the 3-D dataset, to recover it. To the best of our knowledge, this approach has not been adopted before for field inhomogeneity compensation in EPI.

2. We introduce fast alternatives to current two-step null-space based approaches [18, 58, 60] to significantly reduce the computational complexity and memory demand of the algorithm. The proposed signal subspace approach relies on the prior information that there is only one exponential per pixel. Since the central k-space region is not fully sampled as in [18,58,60], we gather the fully sampled rows of the Toeplitz matrix which correspond to the measurements from the two EPI datasets to estimate the signal subspace.

Though this work is conceptually similar to [50], there are fundamental differences. In [50], the off-resonance frequencies and relaxation values along each column of the image are estimated independently using Prony's algorithm. Since the estimates are obtained as an unsorted list, an additional sorting step is needed to ensure a smoothly varying intensity and phase values. When the noise level is high or when the field map is non-smooth, the sorting process can result in erroneous estimates; [50] relies on additional interpolation steps to replace the intensity values in the discontinuous regions. In contrast, we jointly estimate the field map and relaxation map at all the locations by modeling them as a smooth function in space. The proposed algorithm does not require any sorting and can account for low SNR signal regions.

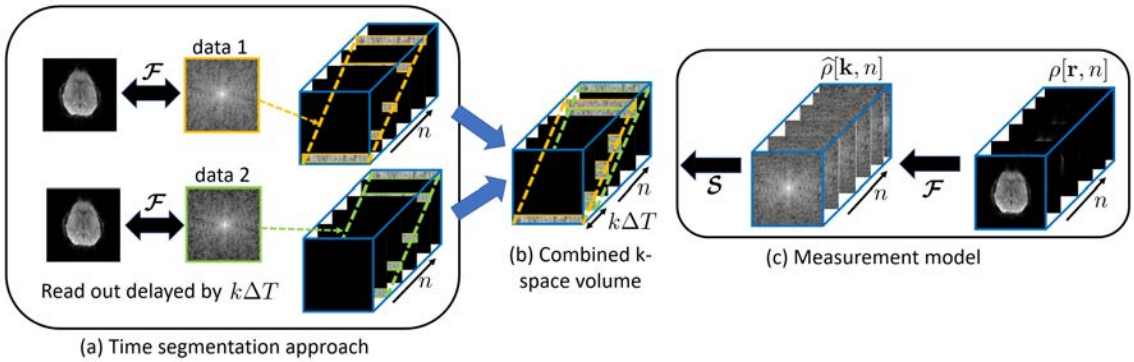

Figure 3.1: Illustration of the time segmented approach and the measurement model: (a) The data acquired from the two EPI acquisitions and their corresponding uncorrected IFFT reconstructions are shown. A time segmentation approach is adopted such that the acquisition window of the two datasets is divided into a number of segments. (b) By combining the time-segmented volumes of both the datasets, a k-space volume with many missing entries is formed. Data from the two EPI acquisitions lie on the yellow and green oblique planes respectively. (c) The operators $\mathcal{F}$ and $\mathcal{S}$ are defined. The data $\widehat{\boldsymbol{\rho}}$ can be undersampled using the operator $\mathcal{S}$ to obtain the volume shown in (b).

3.2 Background

3.2.1 EPI signal model in the presence of B0 inhomogeneity

We model the acquired EPI signal as [51]:

$$s(\mathbf{k}(t)) = \int \underbrace{\rho_0(\mathbf{r}) e^{-\gamma(\mathbf{r})t}}_{\rho(\mathbf{r},t)} \; e^{-j2\pi \mathbf{k}(t)\cdot\mathbf{r}} \mathbf{dr} + \eta(t), \tag{3.1}$$

where $\mathbf{k}(t)$ is the k-space location sampled at time t and $s(\mathbf{k}(t))$ is the corresponding measurement. $\rho_0(\mathbf{r})$ denotes the transverse magnetization of the object and η represents zero mean white Gaussian noise. The term $\gamma(\mathbf{r})$ is a complex quantity that captures the field inhomogeneity induced distortion:

$$\gamma(\mathbf{r}) = R_2^*(\mathbf{r}) + j\omega(\mathbf{r}). \tag{3.2}$$

Here $R_2^*(\mathbf{r})$ and $\omega(\mathbf{r})$ are the relaxation and off-resonance effects respectively at the spatial location $\mathbf{r}$. Note that if $\gamma(\mathbf{r}) = 0$, the relation in (3.1) simplifies to a simple Fourier transform between the object $\rho_0(\mathbf{r})$ and $s(\mathbf{k}(t))$.

3.2.2 Discretization using time segmentation

Since (3.1) contains the field distortion term $\gamma(\mathbf{r})$, it is no longer a Fourier integral and cannot be efficiently computed using the fast Fourier transform (FFT). According to the time segmentation approach [53], the data acquisition window can be divided into several small time segments such that the temporal evolution due to field inhomogeneity ($e^{-\gamma(\mathbf{r})t}$) is assumed to be constant in each segment. For short time segments, this is a fairly accurate assumption and previous works [53] have employed this idea to reduce the computational complexity of image reconstruction in the presence of field inhomogeneity.

3.2.3 Multi-exponential signal model and annihilation

In [4], we model the signal at every pixel location $\mathbf{r}$ as a linear combination of L exponentials:

$$\rho[\mathbf{r}, n] = \sum_{i=1}^{L} \alpha_i(\mathbf{r})\ \beta_i(\mathbf{r})^n, n = 1, 2, \ldots \tag{3.3}$$

where $\alpha_i(\mathbf{r}) \in \mathbb{C}$ is the amplitude and $\beta_i(\mathbf{r}) \in \mathbb{C}$ is an exponential parameter that is dependent on the underlying physiology. Specifically, the imaginary part of β_i can capture the off-resonance effects in the i^{th} component, while the real part can capture the relaxation effects. The exponential signal in (3.3) can be annihilated by a 1-D FIR filter $g[\mathbf{r}, n]$ [72]:

$$\sum_{m=0}^{L} \rho[\mathbf{r}, m]\ g[\mathbf{r}, n-m] = 0, \quad \forall \mathbf{r}. \tag{3.4}$$

where (3.4) represents a 1-D convolution between the signal $\rho[\mathbf{r}, n]$ and a $L+1$ tap filter $g[\mathbf{r}, n]$. The coefficients of the filter are specified by its z transform, $g[\mathbf{r}, z] = \prod_{i=1}^{L}(1 - \beta_i(\mathbf{r})z^{-1})$. The number of taps of the filter $g[\mathbf{r}, n]$ is only dependent on the number

of exponentials in the signal model, which is L. Note that the filter can annihilate signals containing both off-resonance and relaxation terms. The linear predictability relationship described in (3.4) is also exploited in [63] to estimate parameter maps of the brain.

3.2.4 Two step subspace based image recovery

In [34], a two step subspace based approach was introduced to recover dynamic MR images from sparsely sampled Fourier measurements. In the first step, a subspace of temporal basis functions was estimated from a fully sampled calibration data. This was followed by a subspace aware recovery in the second step, where the images are reconstructed using a least squares approach. This two-step strategy was extended in [18,58,60] for single image recovery using low rank Toeplitz matrix priors. Specifically, a fully sampled calibration region was acquired in the center of k-space. The rows of the Toeplitz matrix whose entries correspond to this region was used to estimate the null-space. Using the estimated null space, the image is then reconstructed using a least squares approach in the second step. We note that the Toeplitz priors used in [18, 58, 60] are designed to exploit sparsity and phase relations in 2-D images and are fundamentally different from the exponential priors used in this work.

3.3 Proposed work

We focus on the field inhomogeneity compensation from dual-echo acquisitions in this section. In Section 3.3.1 & 3.3.2, we show how field inhomogeneity compensation can be formulated as the recovery of an image time series from highly undersampled Fourier measurements. We model the time series by an exponential signal model, which is characterized by spatially smooth parameters. In Sections 3.3.3, we show that such a signal satisfies an annihilation condition, which translates to a low rank property of the Toeplitz matrix constructed out of the signal samples. This prior facilitates the recovery of the time series from undersampled measurements; the al-

gorithmic details are introduced in Section 3.3.4.

3.3.1 Reformulation as time series recovery

We propose to adopt the time segmentation approach, described in Section 3.2.2, to reformulate field inhomogeneity compensation to the recovery of an image time series from undersampled measurements; the distortion-free image is the first image of the recovered time series.

We assume the size of each image in the time series is $N \times N$. Each image corresponds to a time segment and contains only k lines of kspace. Let the time taken to acquire one line of kspace be ΔT, which translates to a delay of $T = k\Delta T$ between two consecutive segments/images. Fig. 3.1 a) illustrates this time segmentation approach. With this discretization, the measurements at $t_n = nT; n = 1, 2, \ldots \frac{N}{k}$, are specified by:

$$\begin{aligned} \mathbf{b}_n &= \int \underbrace{\rho_0(\mathbf{r}) e^{-\gamma(\mathbf{r})nT}}_{\rho_n(\mathbf{r})} e^{-j2\pi \mathbf{k}_n \cdot \mathbf{r}} \mathbf{dr} + \boldsymbol{\eta}_n \\ &= \mathcal{A}_n(\boldsymbol{\rho}_n) + \boldsymbol{\eta}_n \end{aligned} \tag{3.5}$$

Here $\boldsymbol{\rho}_n$ is the image corresponding to $t_n = nT$, while $\mathbf{b}_n$ is its Fourier measurement. The operator $\mathcal{A}_n$ is a linear acquisition operator corresponding to the n^{th} segment, which represents a fast Fourier transform followed by multiplication by the sampling mask of the n^{th} segment. Mathematically, $\mathcal{A}_n = \mathcal{S}_n \circ \mathcal{F}$, where $\mathcal{S}_n$ denotes the sampling operator at the n^{th} time instant, $\mathcal{F}$ is the Fourier operator and $\circ$ denotes point-wise multiplication. Since the temporal evolution of $e^{-\gamma(\mathbf{r})t}$ can be safely ignored during the duration T, the magnitude of the images $\rho_n(\mathbf{r})$ can be assumed to have no geometric distortion. However, due to relaxation effects the magnitude image $\rho_n(\mathbf{r})$ is given by $\rho_0(\mathbf{r})e^{-R_2^*(\mathbf{r})nT}$; the first image $\rho_1(\mathbf{r})$ is least affected by $\mathbf{R}_2^*$. Since $\mathbf{b}_n$ corresponds to only a small fraction of the k-space measurements of $\boldsymbol{\rho}_n$, the direct recovery of $\rho_n(\mathbf{r})$ from $\mathbf{b}_n$ is challenging.

3.3.2 Time series recovery from dual echo acquisition

We consider the joint estimation of the distortion (field inhomogeneity and relaxation) map and the distortion-free image from the given set of Fourier measurements. This translates to estimating two complex unknowns, $\rho_0(\mathbf{r})$ and $\gamma(\mathbf{r})$, at every pixel. By a simple degrees of freedom argument, we deduce that at least two complex measurements are needed at each pixel to estimate all of the unknown parameters. For this purpose, we acquire two gradient echo EPI datasets, where the readout of the second dataset is delayed by $m\Delta T,\ m \in \mathbb{Z}$; the echo times are separated by $m\Delta T$. In the illustration in Fig. 3.1 (a), the Fourier measurements corresponding to the two EPI acquisitions can be visualized as the yellow and green oblique planes for the case $m = k$.

Let $\mathbf{b}_n^{(1)}$ and $\mathbf{b}_n^{(2)}$ represent the undersampled Fourier measurements corresponding to the two EPI datasets. We express them using the linear acquisition operator $\mathcal{A}_n$, defined in (4.4):

$$\begin{aligned} \mathbf{b}_n^{(1)} &= \mathcal{A}_n(\boldsymbol{\rho}_n); \quad n = 1, 2, \dots \frac{N}{k} \\ \mathbf{b}_{n-\frac{m}{k}}^{(2)} &= \mathcal{A}_{n-\frac{m}{k}}(\boldsymbol{\rho}_n); \quad n = \frac{m}{k} + 1, \dots M \end{aligned} \tag{3.6}$$

where $M := \frac{N}{k} + \frac{m}{k}$. We have assumed that the two EPI datasets have been time-segmented into $\frac{N}{k}$ segments and each segment contains exactly k lines. For example, when $N = 64$ and $m, k = 4$, the time segmented volume contains 16 segments or frames. When $m = k$, we can observe that the phase evolution present in the second segment of $\mathbf{b}_n^{(1)}$ and first segment of $\mathbf{b}_n^{(2)}$ will be the same, the phase evolution present in the third segment of $\mathbf{b}_n^{(1)}$ and second segment of $\mathbf{b}_n^{(2)}$ will be the same and so on. We combine the measurements from both the acquisitions and express them compactly:

$$\mathbf{b} = \mathcal{A}(\boldsymbol{\rho}) + \boldsymbol{\eta} \tag{3.7}$$

where $\boldsymbol{\rho} = [\boldsymbol{\rho}_1, \boldsymbol{\rho}_2, \ldots \boldsymbol{\rho}_M]$ is the time series of images, $\mathcal{A}$ is the measurement operator and $\boldsymbol{\eta}$ represents zero mean white Gaussian noise. The formation of the combined k-space volume corresponding to the image series $\boldsymbol{\rho}$, for the case $m = k$, is illustrated in Fig. 3.1 (b). For an illustration of the measurement model, refer to Fig. 3.1 (c).

Thus by adopting the time segmentation approach, the field inhomogeneity correction problem was transformed into a problem of recovering an image series from highly undersampled and structured Fourier measurements. The distortion-free image corresponds to the first frame of the recovered volume. However, (3.7) is an ill-posed problem and direct recovery of $\boldsymbol{\rho}$ from $\mathbf{b}$ is not possible without enforcing a signal prior.

3.3.3 Annihilation of single exponential with smoothly varying parameters

We will now focus on a single exponential signal model ($L = 1$), which is a special case of the model considered in (3.3). From Section 3.2.3, it follows that $\rho[\mathbf{r}, n]$ can be annihilated by a two tap FIR filter $d[\mathbf{r}, n]$, whose filter coefficients are $[1, -\beta(\mathbf{r})]$. Note that the linear prediction/annihilation relations in (3.4) and the work in [63] consider the independent annihilation of the signal at each pixel. In the EPI setting, the exponential parameter $\gamma(\mathbf{r})$ depends on the distortion map and can be assumed to vary smoothly across the spatial locations. Hence, the filter coefficients which depend on the exponential parameters can be assumed to be smooth functions of $\mathbf{r}$. Plugging $L = 1$ in (3.4) and taking the 2D Fourier transform along the spatial dimension $\mathbf{r}$, we obtain the following 3-D annihilation relation:

$$\widehat{\rho}[\mathbf{k}, n] \otimes \widehat{d}[\mathbf{k}, n] = 0. \tag{3.8}$$

where $\rho[\mathbf{r}, n] \overset{\mathcal{F}_{2D}}{\leftrightarrow} \widehat{\rho}[\mathbf{k}, n]$ and $d[\mathbf{r}, n] \overset{\mathcal{F}_{2D}}{\leftrightarrow} \widehat{d}[\mathbf{k}, n]$ are the 2-D Fourier coefficients of $\rho[\mathbf{r}, n]$ and $d[\mathbf{r}, n]$ respectively, while $\otimes$ denotes 3-D convolution. Since the inhomogeneity map is smooth, we assume $\widehat{d}[\mathbf{k}, n]$ to be a bandlimited 3-D FIR filter; its spatial

bandwidth controls the smoothness of the parameters, while its bandwidth along the temporal dimension is dependent on the number of exponentials in the signal model, which is two in this case. When the filter dimensions are over-estimated, there will be multiple filters $\widehat{d}_1[\mathbf{k}, n], .., \widehat{d_P}[\mathbf{k}, n]$ that satisfy (3.8) [4, 60].

Expressing the above annihilation relations in compact matrix notation, we obtain

$$\mathcal{T}(\widehat{\boldsymbol{\rho}}) \ \left[\widehat{\mathbf{d}_1}, \ldots, \widehat{\mathbf{d}_P}\right] = 0 \tag{3.9}$$

where $\mathcal{T}$ is a linear operator that maps a 3-D dataset $\widehat{\boldsymbol{\rho}}$ into a multi-fold Toeplitz matrix $\mathcal{T}(\widehat{\boldsymbol{\rho}}) \in \mathbb{C}^{m \times s}$. Here m refers to the number of valid convolutions between $\widehat{\rho}[\mathbf{k}, n]$ and $\widehat{d}[\mathbf{k}, n]$, represented by the red cuboid in Fig. 3.2. Λ denotes the support of the filter $\widehat{d}[\mathbf{k}, n]$, indicated by the blue cuboid in Fig. 3.2 and $s = |\Lambda|$ (product of the filter dimensions). $\widehat{\mathbf{d}}_i$ represents the vectorized 3-D filter $\widehat{d}_i[\mathbf{k}, n]$. From (3.9), we observe that $\mathcal{T}(\widehat{\boldsymbol{\rho}})$ has a large null space and hence has a low rank structure.

3.3.4 Two step algorithm

First we describe the extension of the two-step null-space based strategy described in Section 3.2.4, before introducing the signal subspace approach in Section 3.4.

3.3.4.1 Step 1: Estimation of the null space

The null space of the multi-fold Toeplitz matrix $\mathcal{T}(\widehat{\boldsymbol{\rho}})$ can be estimated from the observed samples. Similar to [18, 58, 60], we construct a sub-matrix of $\mathcal{T}(\widehat{\boldsymbol{\rho}})$, denoted by $\mathcal{T}_s(\widehat{\boldsymbol{\rho}})$, by selecting rows that are fully sampled. Since the acquisition of fully sampled calibration region is not possible in the EPI setting, we extract fully sampled rows of the Toeplitz matrix whose entries correspond to the measured data; they are shown to lie on the dotted yellow and green oblique planes in Fig. 3.1.(a)&(b). Note that this is possible since the filter has only two taps along time. When sufficient number of rows are measured, the null-space of the sub-matrix $\mathcal{T}_s(\widehat{\boldsymbol{\rho}})$ is the same

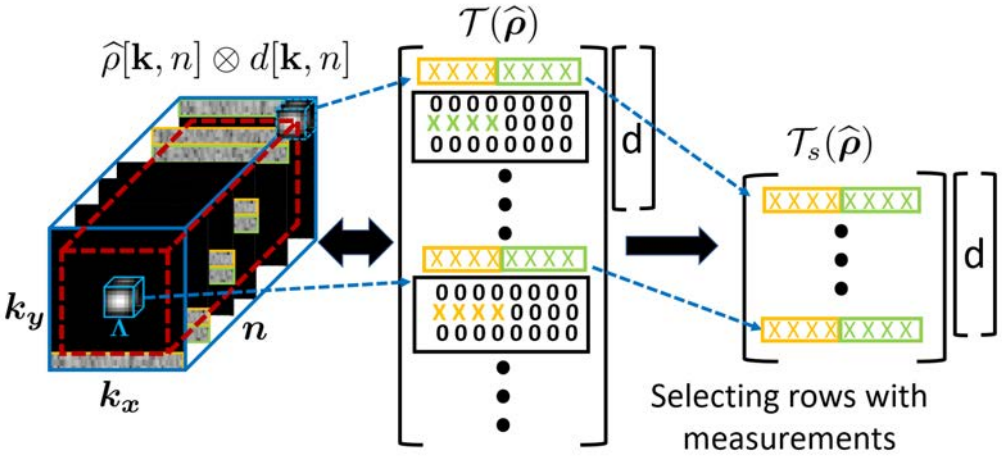

Figure 3.2: Illustration of the construction of the matrices $\mathcal{T}(\widehat{\boldsymbol{\rho}})$ and $\mathcal{T}_s(\widehat{\boldsymbol{\rho}})$ from the combined k-space volume $\widehat{\boldsymbol{\rho}}$: The 3D convolution between a filter with support Λ and $\widehat{\boldsymbol{\rho}}$ results in a multi-fold Toeplitz matrix $\mathcal{T}(\widehat{\boldsymbol{\rho}})$ with many rows filled with zeros; the valid convolutions are defined inside the red cuboid. The rows of $\mathcal{T}(\widehat{\boldsymbol{\rho}})$ correspond to cuboid shaped neighborhoods of the Fourier samples. A smaller matrix $\mathcal{T}_s(\widehat{\boldsymbol{\rho}})$ is constructed from $\mathcal{T}(\widehat{\boldsymbol{\rho}})$ by selecting only fully sampled rows.

as that of the full matrix $\mathcal{T}(\widehat{\boldsymbol{\rho}})$. When data from multiple channels are available, Toeplitz matrices corresponding to different coils are concatenated vertically to form $\mathcal{T}(\widehat{\boldsymbol{\rho}})$. See Fig. 3.2 for the construction of $\mathcal{T}(\widehat{\boldsymbol{\rho}})$ and $\mathcal{T}_s(\widehat{\boldsymbol{\rho}})$. We obtain the null-space of $\mathcal{T}_s(\widehat{\boldsymbol{\rho}})$ as

$$\mathbf{D} = \mathbf{V}\mathbf{Q}, \tag{3.10}$$

where $\mathbf{V}$ are the eigen vectors of $\mathbf{R} = [\mathcal{T}_s(\widehat{\boldsymbol{\rho}})]^* [\mathcal{T}_s(\widehat{\boldsymbol{\rho}})]$ and is estimated from the eigen decomposition of $\mathbf{R} = \mathbf{V}\Lambda\mathbf{V}^*$. The matrix $\mathbf{Q}$ in (3.10) is specified by $\mathbf{Q} = \mathbf{\Lambda}^{-q/2}$, where q is a small number between 0 and 0.5. Since the eigen values are small for null space vectors, more weight is given to them. Hence this strategy eliminates the need to threshold the eigen values to determine the null space.

3.3.4.2 Step 2: Null space aware recovery of distortion-free image

Once the null space matrix $\mathbf{D}$ is estimated from $\mathcal{T}_s(\widehat{\boldsymbol{\rho}})$, we use it to recover the entire k-space volume by solving the following optimization problem in the Fourier

domain:

$$\min_{\widehat{\boldsymbol{\rho}}} \|\mathbf{S}\widehat{\boldsymbol{\rho}} - \mathbf{b}\|_2^2 \text{ such that } \mathcal{T}(\widehat{\boldsymbol{\rho}})\mathbf{D} = 0 \tag{3.11}$$

where $\mathbf{S}$ is the sampling matrix.

3.4 Accelerating recovery using signal subspace

The second step of the algorithm involves solving (3.11). However its direct implementation is associated with high memory demand and computational complexity due to the construction and storage of the large multi-fold Toeplitz matrix. To overcome this problem, we introduce a signal subspace approach that exploits the prior information of one exponential per pixel to accelerate the recovery. Specifically, we re-express the null-space constrained problem in (3.11) as

$$\min_{\boldsymbol{\rho}} \|\mathcal{A}(\boldsymbol{\rho}) - \mathbf{b}\|_2^2 \text{ such that } \rho[\mathbf{r}, n] = \alpha(\mathbf{r})\beta(\mathbf{r})^n, \tag{3.12}$$

where $\beta(\mathbf{r})$ is the exponential parameter.

We note that (3.12) is a fast and memory efficient alternative to a penalized version of (3.11). To see this, we analyze the memory demand and computational complexity of the gradient computations in one CG iteration of (3.11) and (3.12). For (3.11), the memory and computational complexity are determined by the term $\mathcal{T}^*(\mathcal{T}(\widehat{\boldsymbol{\rho}})\mathbf{D}\mathbf{D}^H)$ in the gradient; here $\mathcal{T}^*$ is the adjoint operator corresponding to $\mathcal{T}$.

Memory demand: We assume each image to be of size $N \times N$, T to be the number of time frames, and the dimensions of the filter to be $p \times p \times 2$. The dominant term determining the memory demand is the space to store the matrix $\mathcal{T}(.)$. Thus, the memory demand of the gradient term is $O((N-p)^2p^2T)$. In contrast, the gradient of (3.12) only requires matrices of the same size as that of the dataset, resulting in a memory demand of $O(N^2T)$. The analysis shows that the proposed scheme provides a factor of $\approx p^2$ fold reduction in memory demand compared to the direct approach

specified by (3.11).

Computational complexity: The dominant term in the evaluation of the gradient of (3.11) is the multiplication of the Toeplitz matrix by $\mathbf{D}\mathbf{D}^H$, which requires $O((N-p)^2p^2T)$ operations. Note that for this formulation, all the computations are performed in the Fourier domain. In contrast, the unconstrained formulation of (3.12) is solved in the image domain. The computational complexity of the gradient computation is determined by the number of FFTs and IFFTs. Thus the number of operations is $O(N^2T\log N)$. The proposed approach offers a speed up of $\frac{(N-p)^2p^2}{N^2\log N}$. For typical values such as $N=64, p=11$ we obtain a 10 fold speed up.

To estimate $\beta(\mathbf{r})$, first we evaluate the spatial IFFT of the null space vectors, denoted by the columns of $\mathbf{D}$. We know from (3.3), that if $\rho[\mathbf{r},n]$ is composed of a single exponential, it can be annihilated by a unique two-tap filter. Hence, the temporal filters $d_i[\mathbf{r},n] \overset{\mathcal{F}_{2D}}{\leftrightarrow} \widehat{d}_i[\mathbf{k},n]$, at a specific $\mathbf{r}$, will be linearly dependent. It is sufficient to use any one of them to recover the signal in foreground pixels and this is computationally more efficient. Note that there is a one-to-one correspondence between exponential parameters and filter coefficients; in this case the signal recovery can be simplified to (3.12). Unfortunately, there are multiple linearly independent temporal filters in background pixels with very low signal. Choosing an arbitrary vector $\mathbf{d}$ from the null space may result in noise amplification in the background regions. To minimize this risk, we propose two strategies to choose a single null space vector.

In the first strategy, we classify the pixels as foreground or background based on the rank of the matrix $(\mathbf{D}_s(\mathbf{r}))$ formed from the temporal filters. Specifically, we choose a single temporal filter at each $\mathbf{r}$ in the foreground regions, while a full rank matrix is assumed in the background regions. In this case, we set the filter coefficients to a small value.

A challenge with the above approach is the relatively high computational com-

plexity, since it requires the singular value decomposition of as many matrices ($\mathbf{D}_s$) as pixels in the image. To reduce the complexity, we introduce a second strategy which is slightly sub-optimal. In this approach, we select one temporal filter at each pixel, irrespective of the pixel being foreground or background. The filter is chosen such that the exponential parameters are spatially smooth. We describe these two strategies in Sections 3.4.1 and 3.4.2.

3.4.1 Exponential parameter estimation using pixel classification

Once the null space vectors specified by the columns of $\mathbf{D}$ are obtained, we estimate the temporal filters $d_i[\mathbf{r}, n]$ by computing the zero-padded IFFT of its columns. At each spatial location $\mathbf{r}$, we form the matrix

$$\mathbf{D}_s(\mathbf{r}) = \begin{bmatrix} d_1[\mathbf{r},0] & \dots & d_L[\mathbf{r},0] \\ d_1[\mathbf{r},1] & \dots & d_L[\mathbf{r},1] \end{bmatrix} \tag{3.13}$$

and compute its rank. We expect the rank of $\mathbf{D}_s(\mathbf{r}) = 1$ in foreground regions, which results in unique two tap filters at these pixels. In contrast, the rank of $\mathbf{D}_s(\mathbf{r}) = 2$ in background regions, where the signal is very low or zero. In the first case, the eigen vector corresponding to the maximum eigen value of $\mathbf{D}_s(\mathbf{r})$ can be chosen, and the exponential parameters can be estimated from it as described below in (3.20). When the rank of $\mathbf{D}_s(\mathbf{r}) = 2$, we infer that the pixel corresponds to a background region, and assume the signal to be zero at that location. In this case, there is no unique temporal filter and hence we set it to a small value.

To improve the estimation of the null-space vectors in the presence of noisy measurements, we propose to first denoise the measurements. We formulate the denoising of the k-space data as the following Schatten-p norm minimization:

$$\widehat{\boldsymbol{\rho}}_{\boldsymbol{d}}{}^{\star} = \arg\min_{\widehat{\boldsymbol{\rho}}_{\boldsymbol{d}}} \|\widehat{\boldsymbol{\rho}}_{\boldsymbol{d}} - \mathbf{b}\|_2^2 + \gamma_0 \|\mathcal{T}(\widehat{\boldsymbol{\rho}}_{\boldsymbol{d}})\|_p \tag{3.14}$$

where γ_0 is a regularization parameter, $\mathcal{T}(\widehat{\boldsymbol{\rho}}_{\boldsymbol{d}})$ is a multi-fold Toeplitz matrix formed from the samples $\widehat{\boldsymbol{\rho}}_{\boldsymbol{d}}$. $\|\mathbf{X}\|_p$ is the Schatten-p norm, defined as $\|\mathbf{X}\|_p := \frac{1}{p}\mathrm{Tr}[(\mathbf{X}^H\mathbf{X})^{\frac{p}{2}}] = \frac{1}{p}\sum_i \sigma_i^p$, where σ_i are the singular values of $\mathbf{X}$. We employ the iterative re-weighted least squares (IRLS) based algorithm recently proposed in [4] to solve (3.14). This scheme alternates between the solution to a quadratic subproblem and the update of the weight matrix $\mathbf{W}$:

$$\widehat{\boldsymbol{\rho}}_{\boldsymbol{d}} = \arg\min_{\widehat{\boldsymbol{\rho}}_{\boldsymbol{d}}} \|\widehat{\boldsymbol{\rho}}_{\boldsymbol{d}} - \mathbf{b}\|_2^2 + \gamma_0 \|\mathcal{T}(\widehat{\boldsymbol{\rho}}_{\boldsymbol{d}})\sqrt{\mathbf{W}}\|_F^2, \tag{3.15}$$

$$\mathbf{W} = \left[\underbrace{[\mathcal{T}(\widehat{\boldsymbol{\rho}}_{\boldsymbol{d}})]^* [\mathcal{T}(\widehat{\boldsymbol{\rho}}_{\boldsymbol{d}})]}_{\mathbf{R}} + \epsilon \mathbf{I}\right]^{\frac{p}{2}-1} \tag{3.16}$$

Here ϵ is added to stabilize the inverse. We note that $\sqrt{\mathbf{W}}$ has a similar structure as the null space matrix $\mathbf{D}$, which is computed in (3.10). Specifically, the columns of $\sqrt{\mathbf{W}}$ correspond to the weighted eigen vectors of the Gram matrix $\mathbf{R}$; the weights being inversely proportional to the eigen values [4]. Thus, (3.15) seeks a signal $\widehat{\boldsymbol{\rho}_d}$ such that the projection of $\mathcal{T}(\widehat{\boldsymbol{\rho}}_{\boldsymbol{d}})$ onto its null space $\sqrt{\mathbf{W}}$ is as small as possible. We use $\sqrt{\mathbf{W}}$ as the surrogate for the null space matrix $\mathbf{D}$.

3.4.2 Smoothness based exponential parameter estimation

The low rank based approach described above suffers from high computational complexity. Hence, we propose a computationally efficient alternative to estimate the vector in the null space of $\mathcal{T}_s(\widehat{\boldsymbol{\rho}})$ which yields spatially smooth exponential parameters. We formulate the recovery of this vector as the following optimization problem:

$$\min_{\widehat{\mathbf{d}}} \|\mathcal{T}_s(\widehat{\boldsymbol{\rho}})\widehat{\mathbf{d}}\|_2^2 + \mu_0 \|\mathbf{C}\widehat{\mathbf{d}}\|_2^2 \tag{3.17}$$

where $\mathbf{C}$ is a diagonal matrix with entries $\sqrt{(k_x^2 + k_y^2)}$; (k_x, k_y) are the kspace coordinates corresponding to the filter coefficients and μ_0 is a regularizing parameter. The regularizer $\|\mathbf{C}\widehat{\mathbf{d}}\|_2^2 = \|\nabla d\|_2^2$, where $d[\mathbf{r}, n] \overset{\mathcal{F}_{2D}}{\leftrightarrow} \widehat{d}[\mathbf{k}, n]$ is the 3-D polynomial corresponding to the Fourier coefficients $\widehat{d}[\mathbf{k}, n]$ and ∇ is the gradient operator. Taking the gradient of (3.17) with respect to $\widehat{\mathbf{d}}$ and setting it to zero, we obtain:

$$\Big[\underbrace{[\mathcal{T}_s(\widehat{\boldsymbol{\rho}})]^*[\mathcal{T}_s(\widehat{\boldsymbol{\rho}})] + \mu_0\mathbf{C}^*\mathbf{C}}_{\mathbf{G}}\Big]\widehat{\mathbf{d}} = 0 \tag{3.18}$$

The solution to (3.18) is the eigen vector corresponding to the minimum eigen value of the matrix $\mathbf{G}$. This scheme is very computationally efficient since $\widehat{\mathbf{d}}$ can be estimated from a single eigen decomposition of $\mathbf{G}$.

The above approach provides a single temporal filter at each pixel, assuming the field map to be smooth. It is also robust to noise and other sources of errors. This approach is significantly faster than the approach described in Section 3.4.1. However, it could be sub-optimal due to the potential degradation in cases with abrupt field map variations at the air-tissue interfaces.

3.4.3 Signal subspace based recovery

Once the nullspace vector $\mathbf{d}$ is estimated using one of the approaches described in Section 3.4.1 or 3.4.2, we can estimate the exponential parameter $\beta[\mathbf{r}]$ and use it to recover the time series by solving (3.12). First, we compute the 3D function corresponding to $\widehat{\mathbf{d}}$ as :

$$\boldsymbol{\mu} = \mathbf{F}^*\mathbf{P}_\Lambda^*\widehat{\mathbf{d}} \tag{3.19}$$

where $\boldsymbol{\mu} = \left[\boldsymbol{\mu}^{(1)}, \boldsymbol{\mu}^{(2)}\right]$, $\mathbf{P}_\Lambda^*$ represents the zero padding operation outside the filter support Λ and $\mathbf{F}^*$ is the inverse discrete Fourier transform matrix. After normalizing,

$\boldsymbol{\mu} = \left[\mathbf{1}, \bar{\boldsymbol{\mu}}^{(2)}\right]$. The exponential parameter $\boldsymbol{\beta}$ can then be computed as:

$$\beta(\mathbf{r}) = (-\bar{\mu}^{(2)}(\mathbf{r}))^{\frac{1}{k}} \tag{3.20}$$

where $k \in \mathbb{Z}$ and $k\Delta T$ is the delay in the readout of the second EPI dataset. Once $\boldsymbol{\beta}$ is estimated, we can recover the time series by solving the following regularized problem:

$$\boldsymbol{\alpha}^* = \arg\min_{\boldsymbol{\alpha}} \|\mathcal{A}\left(\alpha(\mathbf{r})\,\beta(\mathbf{r})^n\right) - \mathbf{b}\|_2^2 + \epsilon_0\|\boldsymbol{\alpha}\|_2^2 \tag{3.21}$$

where ϵ_0 is a parameter that we set to a small value to prevent solutions with very high pixel intensities. We note that (3.21) is equivalent to (3.12) when $\epsilon_0 = 0$. (3.21) can be efficiently solved using a few iterations of the CG algorithm without the evaluation and storage of the Toeplitz matrix $\mathcal{T}(\widehat{\boldsymbol{\rho}})$. When data from multiple channels are available, we solve (3.21) for each coil independently. The final solution $\boldsymbol{\alpha}$ is obtained by a sum-of-squares combination of individual coil solutions.

3.4.4 Algorithm summary

1. Construct the matrix $\mathcal{T}_s(\widehat{\boldsymbol{\rho}})$ from the EPI measurements.

2. Estimate the null space vector using the proposed low rank or smoothness approach. Use (3.20) to estimate the exponential parameter $\boldsymbol{\beta}$.

3. Solve (3.21) to recover the distortion-free image.

3.5 Results

We validate the proposed approach using simulations performed on a numerical brain phantom, and MRI experiments performed on phantom and human data. The human data was collected in accordance with the Institutional Review Board of the University of Iowa. MRI experiments were performed on a GE 3T scanner with a 32-channel head coil using a gradient-echo EPI (GRE-EPI) acquisition. Data from

the spherical phantom and two healthy volunteers were acquired, following shimming. The scan parameters used for the phantom and the human experiments were: FOV = 256 mm, matrix size = 64×64, slice thickness = 3.6 mm, minimum TE = 30 ms, TR = 3100 ms for a total of 40 slices (77.5 ms per slice). For the above GRE-EPI, the time taken to acquire one k-space line (ΔT) was 0.636 ms. For each experiment, we acquired two sets of GRE-EPI data such that the readout of the second data set was delayed by $4\Delta T$. For comparison purposes, we collected a four-shot GRE-EPI data, where we expect to see lower distortions, and a high spatial resolution anatomical image. The anatomical image is only used for qualitative comparisons with images from other methods. It looks different from the other images, since it has a different contrast mechanism.

While solving (3.21) for all our experiments, we formed the time-segmented k-space volume by assuming one line of k-space per time segment ($k = 1$). This resulted in a total of sixty eight time frames ($M = 68$).

3.5.1 Methods for comparison

For the numerical phantom experiments, we compare the proposed approach to the following methods:

3.5.1.1 Iterative smoothness-based approach

The model based iterative smoothness method proposed in [74] is conceptually similar to the proposed framework. We obtained the codes from the authors and adapted the cost function as follows:

$$\min_{\boldsymbol{\rho_0},\boldsymbol{\omega},\mathbf{R}_2^*} \|\mathcal{A}(\boldsymbol{\rho}) - \mathbf{b}\|_F^2 + \lambda_1\|\mathcal{D}(\boldsymbol{\omega})\|_2^2 + \lambda_2\|\mathcal{D}(\mathbf{R}_2^*)\|_2^2 + \lambda_3\|\boldsymbol{\rho_0}\|_2^2 \tag{3.22}$$

where we have modified the data consistency term to be consistent with our signal model and also incorporated the effects of $\mathbf{R}_2^*$, to perform valid comparisons. λ_1, λ_2

and λ_3 are the regularization parameters and $\mathcal{D}$ is a finite difference operator, which is used to enforce smoothness on the field map and the $\mathbf{R}_2^*$ map. To solve (3.22), we employ an alternating minimization algorithm, which iterates between the updates of the distortion-free image $\boldsymbol{\rho_0}$, $\boldsymbol{\omega}$ and $\mathbf{R}_2^*$ till convergence. We employ a gradient descent algorithm to solve the field map and $\mathbf{R}_2^*$ map sub-problems. Using these updates, we update $\boldsymbol{\rho_0}$ by solving the least squares problem in (3.21).

3.5.1.2 Harmonic retrieval method (HR)

In the HR method [50], two-echo EPI data is acquired using a specialized sequence and field map compensation is done on every column of the image independently using a least squares based Prony's method. As their acquisition scheme is different from ours, the simulated data with artifacts was generated using the model in [50]. The codes to simulate the Fourier data and reconstruct the image were downloaded from the author's website.

3.5.1.3 Direct Toeplitz method

Using all the null space vectors, we solve the unconstrained problem corresponding to (3.11) to recover the kspace volume. Note that in this approach, we have to explicitly form and store the Toeplitz matrix $\mathcal{T}(\widehat{\rho})$. Since the null space vectors are estimated from two EPI datasets with echo times separated by $4\Delta T$, we form a k space volume such that the delay (T) between two time frames is $4\Delta T$. Hence in (3.11), the kspace volume consists of seventeen segments with only four kspace lines per segment.

3.5.1.4 Direct method

Here, the distortion maps are obtained from the pixel-wise ratio of the uncorrected images corresponding to the two EPI acquistions. Specifically, the field and $\mathbf{R}_2^*$ maps are computed from the magnitude and phase respectively of the ratio image. To

reduce noise, we also smoothed the maps using a Gaussian filter with a standard deviation of two. Using the smoothed maps, we recovered the distortion-free image by solving (3.21).

3.5.2 Simulation

We demonstrate the performance of the proposed method in correcting the artifacts due to inhomogeneities on a numerical brain phantom [16]. For this purpose, we introduced intensity losses and geometric distortions on the brain phantom shown in (a) in Fig. 3.3 A, using the fieldmap and $\mathbf{R}_2^*$ map (shown in (a) in B and C respectively). The simulated distorted image is shown in (b) in Fig. 3.3 A. To demonstrate the proposed approaches, we created two sets of image series and generated the Fourier data corresponding to them. The exponential decay of the Fourier data corresponding to the second image series was delayed by $4\Delta T$ along the temporal dimension; $\Delta T = 0.636$ ms. Finally, we combined the Fourier data corresponding to both the image series to form a k-space volume using (3.6) and (3.7). We compare the reconstructions, maps and the error images corresponding to the proposed low rank and smoothness methods with the techniques in Section 3.5.1.

Compared to the proposed approaches, the direct Toeplitz method is computationally more expensive and results in a reconstruction with more errors. This can be attributed to the fact that the data is time-segmented with four kspace lines per segment. The assumption that the phase is constant during this time period might not be very accurate. Also, no field and $\mathbf{R}_2^*$ maps have been displayed for this method. This is because there are multiple null space vectors for this method and it is not possible to obtain a single map from them.We observe that the geometric distortions have been reduced to a great extent in the reconstructions corresponding to both the proposed and iterative approaches. We also observe that the field maps corresponding to the proposed and the iterative method closely match the ground truth. However, the $\mathbf{R}_2^*$ map for the iterative approach has a lot more errors than those obtained

using the proposed methods. This results in intensity losses in some regions of the reconstructed image, which are pointed by the red arrows in (e) in Fig. 3.3 A. From the error maps displayed in (j) in Fig. 3.3 B and C, we can infer that the field map and $\mathbf{R}_2^*$ maps estimated using the HR method have a lot of errors and hence results in an image with artifacts, as pointed by the red arrows. As the data was generated to simulate a two-echo EPI acquisition, the read out associated was about twice as long as our read out. Hence, this caused the data to experience more significant $\mathbf{R}_2^*$ loss and geometric distortion artifacts. We also note that the reconstruction from the direct method suffers from artifacts and this can be attributed to poor estimates of the field map and $\mathbf{R}_2^*$ map. We compare the Signal to Error Ratio (SER) and computation times of different methods in Fig. 3.3 A. They were recorded on a high performance computing server with a 24 core Xeon processor. We observe that the run times of the proposed smoothness and low rank approaches are 0.22 s and 41.7 s respectively. The iterative, HR and direct approaches have a run time of 996 s, 0.82 s and 13 s respectively. The increased run time of the low rank approach is due to the additional IRLS based optimization step (3.14) for denoising.

3.5.3 Phantom experiment

The effect of the magnetic field inhomogeneities leading to image distortions can be clearly appreciated in the spherical phantom data in Fig. 3.4, where the straight gridlines appear curved in the uncorrected EP image. Other regions, where the artifacts are quite obvious are pointed by the red arrows. We compare the uncorrected images and the proposed reconstructions corresponding to a few slices in Fig. 3.4. The proposed approaches provide reconstructions with reduced distortion levels comparable to that of the multi-shot EPI data. For a particular slice, we show the estimated field maps using a filter of size 5×5×2 and compare the proposed reconstructions to a high spatial resolution anatomical scan in Fig. 3.6 (A).

3.5.4 Validation on human data

We also validate the proposed algorithms on two human datasets. We compare the uncorrected images and the proposed reconstructions corresponding to a few slices of both the datasets in Fig. 3.5 (A) and (B). As expected, the severity of the distortions vary across subjects and brain regions. We observe that the proposed algorithms are able to correct the distortions effectively in all these regions. Note that there are some differences between the proposed and the multi-shot reconstructions for human dataset 2 due to the shorter echo time of the multi-shot data. For a particular slice, we show the estimated field maps and compare the proposed reconstructions to an anatomical scan in Fig. 3.6 (B) and (C). We observe that both the low rank and smoothness based algorithms provide similar reconstructions with minimal artifacts, when compared to the uncorrected single-shot EPI data. For both the proposed approaches, a filter size of $7\times7\times2$ was used to recover both the datasets.

3.5.5 Choice of optimization parameters

There are a few tuning parameters associated with the proposed two step algorithm. In all our experiments, they were chosen empirically. Below, we briefly describe them.

Step1: We have to tune different parameters depending on the approach (low rank or smoothness) employed to estimate the null space vector. μ_0 is associated with the smoothness approach. It was chosen for a dataset with large field inhomogeneity distortion and the same value was retained for other datasets. We observed that this strategy resulted in smooth field maps across the datasets and gave reconstructions with minimal artifacts. Corresponding to the low rank approach, there are two tuning parameters namely γ_0 and ϵ for the denoising step. γ_0 was chosen such that there was significant reduction of noise outside the image while preserving the structures present inside. We observed that the same value gave similar denoising performance across datasets. ϵ is a parameter appearing in the update of the weight matrix $\mathbf{W}$

in (2.18). It ensures the invertibility of $\mathbf{W}$ and also the stability of the IRLS based algorithm. We employ the strategy described in [4] to initialize and vary the value at every iteration.

Step2: ϵ_0 is associated with the least squares problem in (3.21). We set it to a small value to prevent solutions with very high pixel intensities and kept it constant across datasets.

Finally, as the filter size was not known apriori, we also treated it as an optimization parameter and chose it empirically to result in an image with minimal distortions. Specifically, we estimated the filter size for a dataset with large field inhomogeneity distortion and retained it for other datasets. We observed that this strategy did not affect the performance of the algorithm and gave good reconstructions for all the datasets.

We observed that the distortions were quite different between our datasets. Yet, the same tuning parameters resulted in good performance across datasets. This leads us to believe that for new datasets, the parameters will be in the same ballpark.

3.6 Discussion and conclusion

We introduced a two step structured low rank algorithm for the calibration-free compensation of field inhomogeneity artifacts in EPI data. We transformed the EPI distortion correction to the recovery of an image time series from undersampled Fourier measurements. This enabled us to rely on 3-D annihilation relations in the Fourier domain, resulting from exponential signal structure and spatial smoothness of the exponential parameters, to recover the dataset from highly undersampled measurements. We introduced a novel signal subspace based approach to solve the optimization problem, which resulted in a fast and efficient algorithm.

We validated the proposed methods on MRI phantom and human data and demonstrated the potential of the proposed approaches in correcting the artifacts. Specifically, the geometric distortions and intensity losses were significantly reduced in the

reconstructions from the proposed methods, compared to the uncorrected single-shot EPI data. The proposed reconstructions were also in agreement with a high spatial resolution structural scan and a four shot EPI data. Since the proposed approach requires two EPI datasets, its acquisition time is half that of the four shot EPI acquisition considered in this work. We expect the need for more shots to reduce the distortions in high-resolution applications, where the proposed algorithm would be even more desirable. Specifically, the longer acquisition time of multi-shot EPI makes it more susceptible to motion artefacts.

The validations on the MR phantom and human data also show that the exponential parameter estimated from smoothness and low rank approaches are very similar, thus resulting in similar reconstructions. However, we observe that the smoothness based method is more robust to noise as compared to the low rank approach and does not require denoising of the measurements prior to the estimation of the null space. Specifically for the low rank approach, the denoising step was able to get rid of some pixelation artifacts in the inhomogeneity corrected image. The need for denoising makes it more computationally expensive than the smoothness based approach. For numerical simulation experiments, the run times for the smoothness and low rank approaches were recorded as 0.22 s and 41.7 s respectively.

Our numerical simulations on the brain phantom in Fig. 3.3 also show that the proposed schemes can provide improved reconstructions compared to the techniques described in Section 3.5.1. We also show that the direct Toeplitz method is computationally more intensive than the proposed approach. Specifically, we note that the proposed smoothness approach takes 0.22 s, while the direct Toeplitz based method takes 132 s. The large speed up is due to a difference in formulation and few other factors. Firstly, we observed that the direct Toeplitz method required a large number of CG iterations (around 200) as compared to the proposed scheme (around 25), in order to achieve similar reconstruction quality. Secondly, problem (3.21) correspond-

ing to the proposed approach was solved completely on the GPU. In contrast, the construction of the Toeplitz matrix and its adjoint for the direct Toeplitz method were done on the CPU, while the other term in the gradient was computed on the GPU. Though a more efficient implementation may speed up the direct Toeplitz approach, we expect that the proposed scheme would still offer a significant speed up along with memory savings as discussed in Section 3.4.

We note that the $\mathbf{R}_2^*$ maps follow anatomical structures more closely than the field maps which are inherently smooth. By penalizing the roughness of the field map and $\mathbf{R}_2^*$ map equally, the sharp transitions of the $\mathbf{R}_2^*$ maps might not be captured. This problem can be alleviated by penalizing the roughness of the maps differently, which we plan to pursue in the future.

To compensate for field inhomogeneities, the proposed method requires two EPI datasets such that the read out of the second dataset is delayed by a few ms. We note that motion between the scans can cause errors in the field map estimate. To minimize these errors, we specifically instructed the subjects to stay still during the acquisition of both the datasets. We also plan to investigate single shot strategies using spiral-in/spiral out trajectories to minimize this risk.

We note that the reported TR is higher than current practice. This value was chosen to support the acquisition of the second dataset with different delays (ΔT to $16\Delta T$). This was done to determine the delay and hence the dataset pairs which gave the best performance. A common TR that supported all of the above delays was chosen. We also note that the spatial resolution considered in the experiments is lower than the current practice in fMRI/DTI. The proposed single exponential model might not be fully valid at low resolutions due to partial volume effects. The residual distortions resulting from this misfit can be decreased by moving to higher spatial resolution. In the future, we plan to push the spatial resolution and TR to the state-of-the-art values.

The proposed method can be applied in dynamic applications such as fMRI and diffusion MRI, where it has the potential to compensate for time varying field-map variations. The two EPI datasets can be acquired in an interleaved fashion. Specifically, the readout of datasets acquired at even time points can be delayed from the datasets acquired at odd time points by a few ms. A similar acquisition strategy has been proposed in [13] for dynamic field map distortion correction. The field map compensation can then be done using every pair of neighboring datasets using our proposed scheme. We plan to investigate such applications in future.

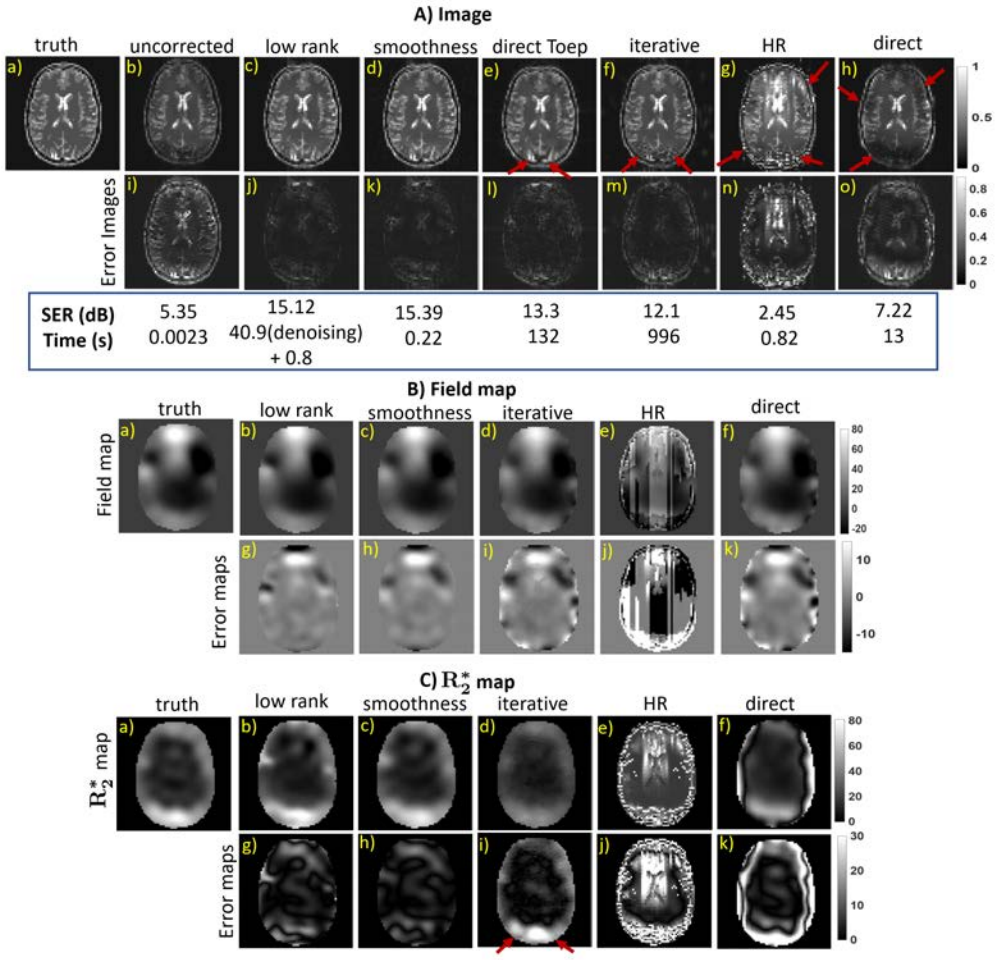

Figure 3.3: Simulation experiments on a numerical brain phantom: In A), the simulated image with artifacts due to field inhomogeneity is shown in (b) and the proposed reconstructions in (c) and (d) are compared with the reconstructions from the direct Toeplitz method (e), iterative (f), HR (g) and direct method (h). The error between the ground truth in (a) and the images from different methods is shown in the second row from (i) to (o). The computation time and SER of the different methods are also shown in A). The estimated field maps and $\mathbf{R}_2^*$ maps from the proposed and the competing methods are compared with the true maps (shown in (a)) in the first row of (B) and (C) respectively. The errors in the field and $\mathbf{R}_2^*$ maps are shown from (g) to (k) in the second row of (B) and (C) respectively. Note that the maps corresponding to the direct Toeplitz method are not shown here. This is because there are several null space vectors in this case and it is not possible to get a single map. Compared to the proposed approaches, we note that this method is more computationally intensive and also results in errors in reconstruction as pointed by the red arrows. We observe that the field map and the $\mathbf{R}_2^*$ maps corresponding to the proposed methods have much lower errors compared to other methods, and hence results in improved reconstructions. We observe some artifacts in the competing methods, which are pointed by the red arrows. Note that the geometric distortion is reduced in the reconstruction corresponding to the iterative approach. However, the errors in the $\mathbf{R}_2^*$ map (red arrows in (i)) results in intensity losses in the reconstruction, which are pointed by the red arrows in (f) in A). The scales of both the field map and the $\mathbf{R}_2^*$ maps are displayed in Hz and s^{-1} respectively.

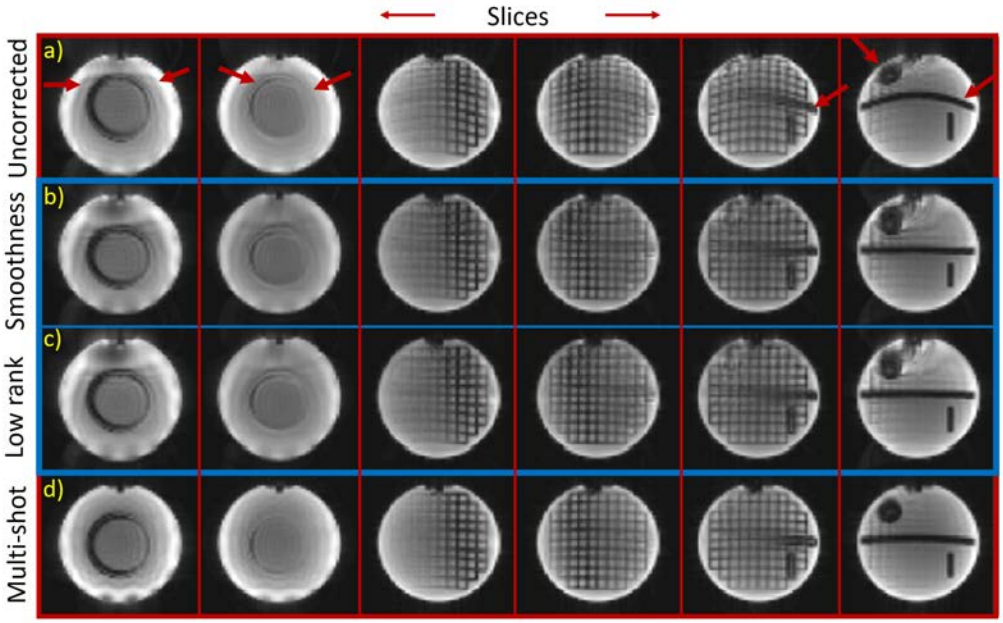

Figure 3.4: Validation of the proposed methods on a spherical MR phantom: A few reconstructed slices corresponding to the proposed low rank and smoothness approaches are displayed inside the blue boxes. For comparison, we have also shown the uncorrected single-shot and multi-shot EP images in the first and fourth rows respectively. We observe that the field inhomogeneity artifacts are greatly reduced in the proposed reconstructions; especially the curved grid lines in the uncorrected EP mages appear straight in the proposed slices. Other artifacts, as pointed by the red arrows in the uncorrected EP images, are also greatly reduced in the proposed reconstructions.

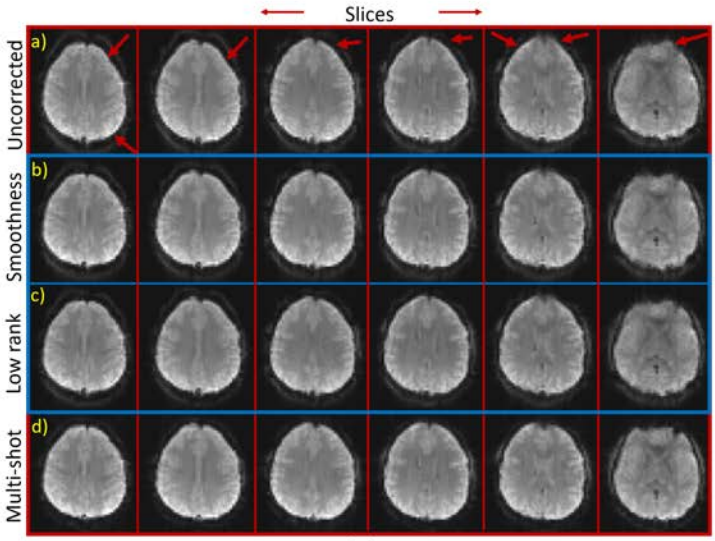

Figure 3.5: Validation of the proposed methods on two human datasets: The proposed reconstructions from a few slices of the two datasets are highlighted using the blue boxes in (A) and (B). For comparison, the uncorrected single-shot and multi-shot EP images are shown in the first and fourth rows respectively. We note that the distortions are more severe in dataset 2 and the severity varies across different regions for both the subjects. We observe that the proposed reconstructions have reduced inhomogeneity artifacts compared to the uncorrected EP images. The distortions are prevalent in many regions of the uncorrected EP images with the red arrows pointing to the most obvious regions. Note there are some differences between the proposed and the multi-shot reconstructions for human dataset 2. This is due to the shorter echo time of the multi-shot data.

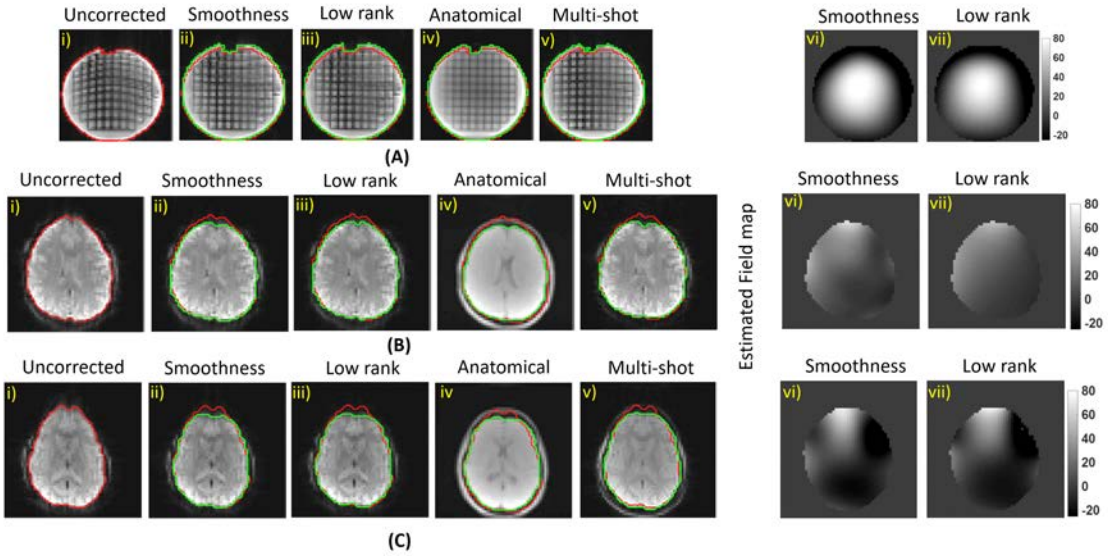

Figure 3.6: Comparison of the proposed reconstructions with a high spatial resolution anatomical scan: For a particular slice, the reconstructions and field maps corresponding to spherical MR phantom, human dataset 1 and dataset 2 are shown in (A), (B) and (C) respectively. In each case, the proposed reconstructions in (ii) and (iii) are compared with a anatomical image in (iv). The uncorrected single-shot and multi-shot EP images are also shown in (i) and (v) respectively. The field maps (Hz) estimated using the proposed approaches are shown in (vi) and (vii). With the aid of the red and green contours, the improvements offered by the proposed approaches can be clearly appreciated.

CHAPTER 4
FIELD MAP COMPENSATION FOR NON-CARTESIAN TRAJECTORIES: DEMONSTRATING ON ROSETTE DATA

4.1 Introduction

MR acquisition schemes with long read outs are often susceptible to off-resonance related artifacts, which arise due to the inhomogeneities in the main magnetic field. These off-resonance artifacts manifest differently in images acquired using Cartesian and non-Cartesian trajectories. For instance in Cartesian EPI where data is acquired using a rectilinear trajectory, the images are affected by geometric distortion artifacts. In non-Cartesian trajectories such as spiral and rosette, there is blurring and intensity losses respectively in images. In the previous chapter, we introduced a novel structured low rank method for correcting field inhomogeneity artifacts in EPI. We showed that images recovered using the proposed method had fewer errors and distortion levels comparable to that of a multi-shot EP image. In this chapter, we extend the structured low rank framework to correct for inhomogeneity related artifacts in non-Cartesian trajectories. Specifically we demonstrate the algorithm for artifact correction on data acquired using Rosette trajectories.

Rosette trajectory was first proposed in [36] and was re-introduced in [52] for spectrally selective imaging. It has been applied in many applications such as functional MRI (fMRI), spectroscopy and fat/water imaging. The function generating the trajectory consists of a rapid one dimensional oscillating sinusoid, which is modulated by a complex exponential. The trajectory goes through the origin and intersects itself many times. This results in significant de-phasing throughout the Fourier space, leading to loss of image intensity.

To correct these inhomogeneity related intensity losses, we employ the time segmentation approach [53] and reformulate the field map compensation problem as a recovery of time series of images from highly undersampled measurements. We adopt the structured low rank framework and formulate the recovery of kspace volume as a

structured low rank optimization problem in the Fourier domain. The trajectory was designed such that the petals of the Rosette trajectory don't overlap and this ensures the incoherence of the undersampling across the time segments/frames of the volume. This also enables the application of compressed sensing type algorithms to recover the missing entries of the volume. For this reason, we employ the IRLS based algorithm, which was introduced in chapter 2, to solve the optimization problem. We also introduce similar approximations, which eliminates the need to store the Toeplitz matrix resulting in a memory efficient algorithm. We demonstrate the proposed method on a 64×64 and 128×128 MR phantom data and show that the proposed reconstructions have fewer errors and artifacts compared to those obtained using conjugate gradient (cg) based Tikhonov reconstructions.

4.2 Rosette trajectory

The rosette trajectory can be described by a rapidly oscillating sinusoidal function, which is also slowly rotating in the $k_x - k_y$ plane [52]. It has the following form:

$$\mathbf{k}(t) = k_{max} \sin(2\pi f_1 t) e^{j2\pi f_2 t} \tag{4.1}$$

where k_{max} is the maximum extent to which the Fourier space is covered, f_1 is the frequency of rapid oscillation of the sinusoid and f_2 is the frequency of the slow rotation. Typically the frequency values are chosen such that the petals of the trajectory don't completely overlap. The gradient waveforms which generate the rosette trajectory according to (4.1) are given by:

$$\begin{aligned} \mathbf{G}(t) &= \frac{2\pi}{\gamma} \frac{d}{dt} \mathbf{k}(t) \\ &= \frac{2\pi}{\gamma} k_{max} ((2\pi f_1 + 2\pi f_2) e^{j(2\pi f_1 + 2\pi f_2)t} + (2\pi f_1 - 2\pi f_2) e^{-j(2\pi f_1 - 2\pi f_2)t}) \end{aligned} \tag{4.2}$$

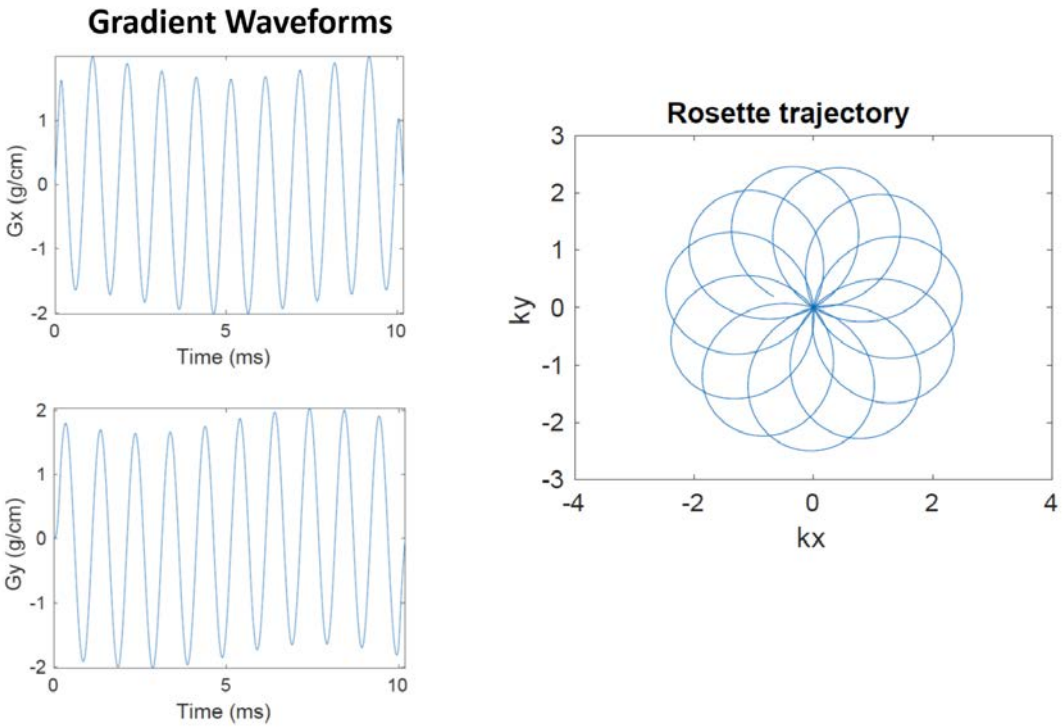

Figure 4.1: Plot of the gradient waveforms and the rosette trajectory generated using them: The data is acquired for 10 ms using the rosette trajectory. The maximum gradient amplitude and slew rate was assumed to be 25 mT/m and 115 T/m/s respectively.

where $\gamma = 2.675.10^8$ rad/(s.T) is the gyromagnetic ratio for protons. Refer Fig. 4.1 which shows the Rosette trajectory and the gradient forms generating it. While designing k space trajectories in MRI, we should always make sure that the maximum value of gradient amplitude and the maximum rate of change of gradient amplitude (slew rate) do not exceed values specified by the vendors. These two parameters serve as constraints and help us in designing the values of the frequencies f_1 and f_2. The maximum value of gradient amplitude and the slew rate can be computed as:

$$\begin{aligned} |G| &\leq \frac{2\pi}{\gamma} k_{max} \omega_1 \\ |S| &\leq \frac{2\pi}{\gamma} k_{max} (\omega_1^2 + \omega_2^2) \end{aligned} \tag{4.3}$$

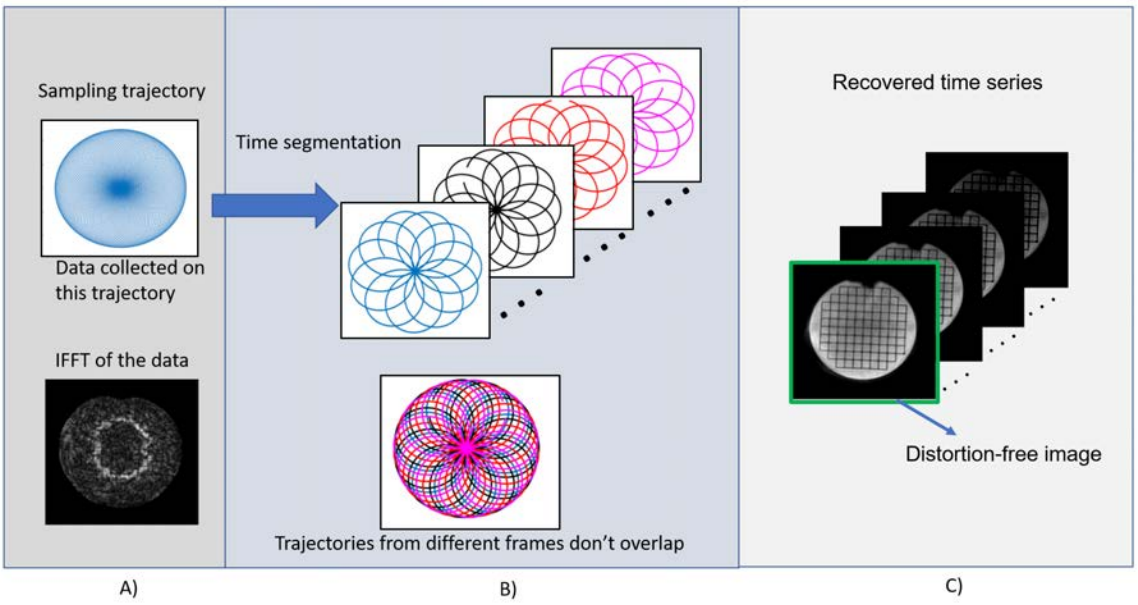

Figure 4.2: Reformulation of the artifact correction problem as the recovery of image time series: Shown in (A) are the sampling trajectory on which the data is acquired and the image corresponding to it. The data acquisition window is divided into multiple short time segments and the sampling trajectories corresponding to the different segments are shown in (B). Note that the trajectories corresponding to the different segments don't overlap. This incoherence between the frames enables the application of compressed sensing based algorithms to recover the image time series from undersampled measurements. Upon recovery, the first image corresponds to the distortion-free image.

where $\omega_1 = 2\pi f_1$ and $\omega_2 = 2\pi f_2$.

4.3 Proposed approach

When the read out associated with the Rosette acquisition is long, the images are corrupted by off-resonance related artifacts which manifest as intensity losses. To correct these artifacts, we extend the proposed ideas and framework for the EPI setting to non-Cartesian Rosette setting. To make this chapter self-contained we briefly summarize the main ideas below.

4.3.1 Time segmentation and reformulation as time series recovery

To correct the inhomogeneity related artifacts, we adopt the time segmentation approach and reformulate the artifact correction problem into a recovery of time series of images from undersampled measurements. Upon recovery, the distortion free image will correspond to the first image. An illustration of the reformulation process is shown in Fig. 4.2. We assume the size of each image in the time series is $N \times N$. With this discretization, the measurements at $t_n = nT; n = 1, 2, \dots M$, are specified by:

$$\begin{aligned} \mathbf{b}_n &= \int \underbrace{\rho_0(\mathbf{r}) e^{-\gamma(\mathbf{r})nT}}_{\rho_n(\mathbf{r})} e^{-j2\pi \mathbf{k}_n \cdot \mathbf{r}} d\mathbf{r} + \boldsymbol{\eta}_n \\ &= \mathcal{A}_n(\boldsymbol{\rho}_n) + \boldsymbol{\eta}_n \end{aligned} \tag{4.4}$$

Here $\boldsymbol{\rho}_n$ is the image corresponding to $t_n = nT$, while $\mathbf{b}_n$ is its Fourier measurement. The operator $\mathcal{A}_n$ is a linear acquisition operator corresponding to the n^{th} segment.

4.3.2 Annihilation relation and structured matrix prior

We assume a single exponential signal model, defined in chapter 3, at every pixel location. We exploit the linear predictability of the exponential signal at every pixel location along with the smoothness of the parameters to derive a 3D annihilation relation in the Fourier domain:

$$\widehat{\rho}[\mathbf{k}, n] \otimes \widehat{d}[\mathbf{k}, n] = 0. \tag{4.5}$$

where $\rho[\mathbf{r}, n]$ and $d[\mathbf{r}, n]$ are the 2-D Fourier coefficients of $\rho[\mathbf{k}, n]$ and $d[\mathbf{k}, n]$ respectively, while $\otimes$ denotes 3-D convolution. We assume that the inhomogeneity map to be smooth; this implies $\widehat{d}[\mathbf{k}, n]$ is a bandlimited 3-D FIR filter. The spatial bandwidth controls the spatial smoothness of the parameters, while its temporal bandwidth is two. When the filter dimensions are over-estimated, there will be multiple filters

$\widehat{d_1}[\mathbf{k}, n], .., \widehat{d_P}[\mathbf{k}, n]$ that satisfy (4.5) [4, 60].

Expressing the above annihilation relations in compact matrix notation, we obtain

$$\mathcal{T}(\widehat{\boldsymbol{\rho}}) \left[\widehat{\mathbf{d}_1}, \ldots, \widehat{\mathbf{d}_P}\right] = 0 \tag{4.6}$$

where $\mathcal{T}(\widehat{\boldsymbol{\rho}})$ is a multi-fold Toeplitz matrix formed from the Fourier samples. From (4.6), we can infer that $\mathcal{T}(\widehat{\boldsymbol{\rho}})$ is low rank.

4.3.3 Structured low rank optimization problem

We exploit the low rank property of the Toeplitz matrix to recover the time series of images from undersampled measurements. For this purpose, we pose the recovery as the following optimization problem:

$$\widehat{\boldsymbol{\rho}}^{\star} = \arg\min_{\widehat{\boldsymbol{\rho}}} \|\mathcal{T}(\widehat{\boldsymbol{\rho}})\|_p + \frac{\mu}{2}\|\mathcal{A}(\widehat{\boldsymbol{\rho}}) - \mathbf{b}\|_2^2 \tag{4.7}$$

where μ is a regularization parameter and $\|.\|_p$ is the Schatten p norm, which is defined in chapter 1.

4.3.4 Optimization algorithm

We note that the sampling pattern across the frames is highly incoherent. We made sure of this by designing the rosette trajectory in such a way that its petals didn't overlap. As incoherence in the measurements between the frames favors compressed sensing based algorithms, we apply an iterative strategy similar to the one applied to the MR parameter mapping problem in chapter 2. Specifically we employ an IRLS based algorithm, which alternates between the update of a weight matrix and a least squares solution, to solve (4.7).

As the size of the filter is chosen to be small, the update of the weight matrix is done according to (2.18). However, there is a huge computational burden associated with the least squares problem (2.17). To address this issue we introduce approxima-

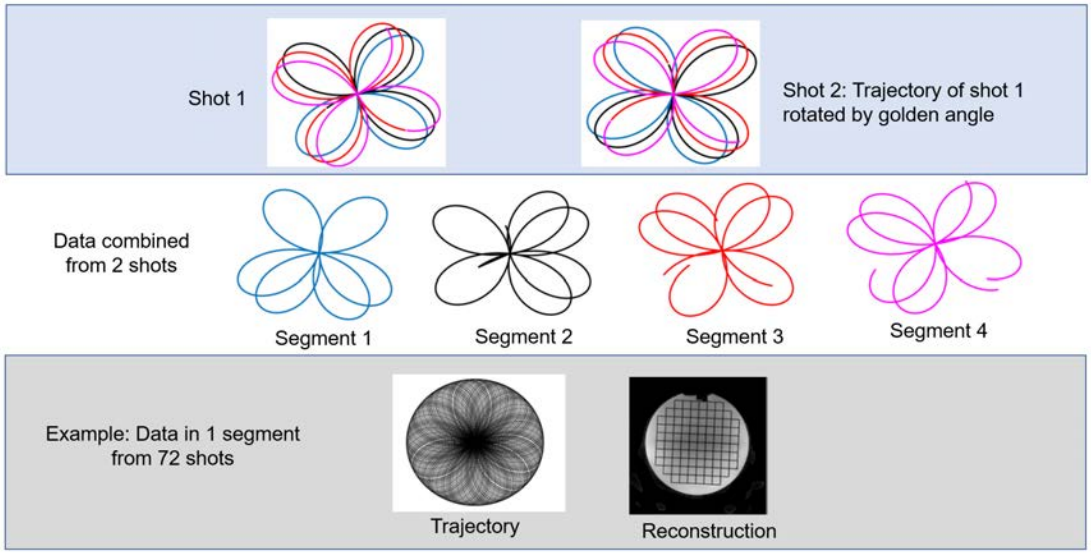

Figure 4.3: Multishot data for reference: In the top row, data corresponding to two shots are shown. The scan parameters for the two datasets were the same; however the trajectory of the second dataset was rotated by golden angle. Upon time segmentation, data from both the shots are combined to form the measurements of each segment. This is shown in the middle row. In the bottom row, the measurements in one segment are formed by combining data from 72 shots. The image corresponding to this segment is treated as a reference.

tions similar to those introduced in chapter (2). Specifically, we approximate the 3D linear convolution as a series of 2D circular convolutions along the spatial dimension and a linear convolution along time. These approximations enable us to solve the least squares problem efficiently using fast Fourier transforms.

4.4 Results

4.4.1 Data acquisition

We used the platform provided by GE's Multi Nuclear Spin (MNS) package to design the rosette trajectory. The package consists of a set of matlab codes, which can be modified to design different kinds of k space trajectories such as rectilinear, rosette, spiral etc.

The 3T MR scanner at the University of Iowa is equipped with gradient coils with maximum gradient amplitude (max grad) and slew rate (max slew) of 44 mT/m and 200 T/m/s respectively. We designed the values of f_1 and f_2 such that max grad and max slew in (4.3) were assumed to be 25 mT/m and 115 T/m/s respectively. Heuristically, we set $f_2 = \frac{f_1}{\alpha}$, where $\alpha = 1.9416$, in (4.3) and estimated the frequencies. The gradient waveforms were designed to generate a rosette trajectory corresponding to the estimated frequencies. Empirically, we observed that this resulted in a trajectory with non-overlapping petals. We also observed that there was uniform coverage of kspace in each frame of the volume, generated using time segmentation approach.

Using the above designed trajectory, we acquired a phantom data on a GE 3T scanner with a 32 channel head coil. The scan parameters used for the phantom were as follows: FOV = 256 mm, matrix size of dataset 1 = 64x64, matrix size of dataset 2 = 128x128, slice thickness = 3.6 mm, TR = 100 ms.

In order to obtain a ground truth for our experiments, we acquired multiple rosette datasets, herein referred to as shots, with the same scan parameters; the trajectory of each dataset was rotated by a multiple of golden angle. We acquired 36 shots and 72 shots corresponding to the 64×64 and 128×128 datasets respectively. In order to generate the volume, we divided the acquisition window into 40 segments such that each segment contained data for 2.5 ms. Fully sampled data for each segment can be obtained by combining the measurements from different rotations. An illustraton of the formation of the multishot data is shown in Fig. 4.3. The coil maps were estimated from the data itself using the ESPIRIT algorithm [39]. The images corresponding to each segment were obtained by solving a CG based Tikhonov reconstruction algorithm. The first image of the series was considered as the ground truth.

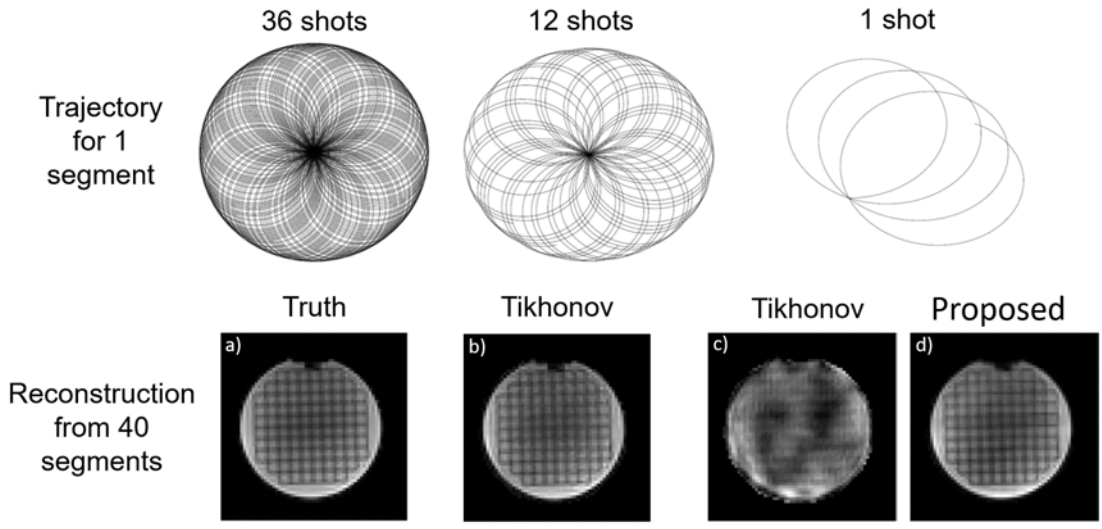

Figure 4.4: Demonstration of the proposed method on a low resolution 64×64 dataset: In the top row, the sampling trajectory for 1 segment corresponding to 36 shots, 12 shots and 1 shot are shown. The reconstructions from different methods are shown in the bottom row. The proposed reconstruction in d) is compared with the ground truth in a) and Tikhonov reconstructions on 12 shot and 1 shot data in b) and c) respectively. We can clearly appreciate the quality of the proposed reconstruction over the 1 shot Tikhonov reconstruction.

4.4.2 Phantom experiment

We validate the proposed approach on both the MR phantom datasets. We illustrate the results on a low resolution 64×64 dataset in Fig. 4.4. The proposed method was applied on 1 shot data and the reconstruction is shown in d). This is compared to the ground truth in a), Tikhonov reconstruction of 12 shot and 1 shot in b) and c) respectively. We observe that the Tikhnov (1 shot) reconstruction has a lot of artifacts and intensity losses, which are significantly reduced in the proposed reconstruction. We note that the quality of the Tikhnonov reconstruction improves when the number of shots is increased to 12. It can be observed from the figure that the image qualities of both the proposed method and the 12 shot reconstruction are similar.

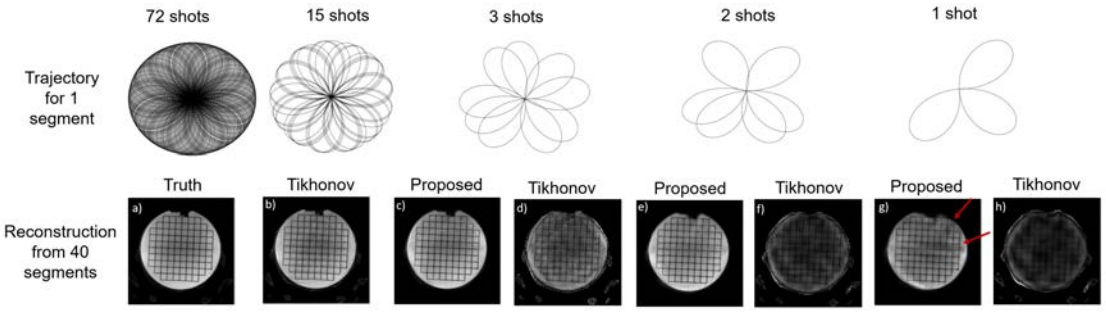

Figure 4.5: Demonstration of the proposed method on a high resolution 128×128 dataset: In the top row, the sampling trajectory for 1 segment corresponding to 72 shots, 15 shots, 3 shots, 2 shots and 1 shot are shown. The reconstructions from different methods are shown in the bottom row. The proposed reconstructions on 3 shots, 2 shots and 1 shot are shown in c), e) and g) respectively. They are compared to the ground truth in a) and Tikhonov reconstructions on 15 shot, 3 shot, 2 shot and 1 shot data in b), d), f) and h) respectively. We can clearly observe that the proposed method on 2 and 3 shots provides improved reconstructions over the Tikhonov reconstructions. However the proposed reconstruction corresponding to 1 shot has artifacts and errors, which are pointed by the red arrows in g).

The results corresponding to the high resolution 128 data are shown in Fig. 4.5. The proposed method was applied on 3 shots, 2 shots and 1 shot data and the reconstructions are shown in c), e) and g) respectively. They are compared to the ground truth in a) and Tikhonov reconstructions applied to 15 shots, 3 shots, 2 shots and 1 shot, shown in b), d), f) and h) respectively. We observe that the Tikhonov reconstructions corresponding to 1, 2 and 3 shots have a lot of intensity losses and artifacts, which are reduced in the 15 shot reconstruction. However, the proposed method on 2 shot and 3 shot data provides improved reconstructions over the 15 shot Tikhonov reconstruction. On 1 shot data, where the number of samples per frame is very low, the proposed reconstruction has artifacts and intensity losses as pointed by the red arrows in g).

4.5 Conclusion

In chapter 3, we introduced a structured low rank method to correct the field inhomogeneity related artifacts in the EP image. Here, we extend this framework to correct the off-resonance related intensity artifacts and losses occuring in images acquired using the rosette trajectory. We designed the rosette trajectory on the platform provided by GE's MNS package. We validated the algorithm on two MR phantom datasets acquired using our designed trajectory. We compare the proposed reconstructions against the ground truth obtained from a large number of shots (36 for low resolution data and 72 for high resolution data). We observed that the proposed method provides images of similar quality as the ground truth from much fewer shots (1 shot for low resolution data and 2 to 3 shots for high resolution data). For the Tikhonov reconstructions to have similar image quality as the proposed reconstructions, the number of shots required are 12 and 15 shots for low resolution and high resolution data respectively.

CHAPTER 5
ACCELERATED DYNAMIC MRI

5.1 Introduction

Obtaining high spatial & temporal resolution is challenging in dynamic MRI, mainly due to the slow nature of acquisition. A common approach to speed up the acquisition is to acquire undersampled Fourier data and to regularize the recovery problem using appropriate priors. Common regularization penalties include ℓ_1 sparsity prior in the Fourier/wavelet domain and smoothness priors (e.g. total variation regularization).

Recently, structured low rank matrix priors are emerging as powerful alternatives for classical ℓ_1 regularization [17, 27, 56, 58]. For example, we have modeled a 2-D image as a piecewise smooth signal, whose partial derivatives are localized to zero-crossings of a band limited trigonometric polynomial [56, 58]; this work is inspired by [62]. We have shown that such a signal can be annihilated by a large set of finite impulse response filters in the Fourier domain. These annihilation relations imply that a matrix with convolutional structure derived from the uniform Fourier samples of the signal is low-rank. We have exploited this property to recover the image from uniform [59] and non-uniform samples [56]. Since these methods can exploit the additional structure in many multidimensional problems (e.g. smoothness of the edges), on top of sparsity, they are demonstrated to yield better reconstruction performance than classical total variation methods. These methods are generalization of classical 1-D FRI methods [35,78] to the multidimensional setting with non-uniform sampling.

Despite improved performance, structured low rank methods suffer from high memory demand and computational complexity, both resulting from the lifting of the original 2-D problem to a dense high-dimensional structured matrix. Since the dimension of the matrix is atleast two to three orders of magnitude greater than the size of

the original data, it results in computationally expensive algorithms. Various methods have been explored to make the computational complexity manageable. For example, greedy multi-scale approximations to sequentially recover the image [27] and factorization of the matrix to two low-dimensional matrices have been explored [17, 27]. Despite these approximations, it is still challenging to extend the above scheme to three dimensions and beyond. Current methods recover 2-D slices of the 3D datasets independently [27], which is suboptimal and requires Cartesian undersampling; this approach is not as efficient as more general non-Cartesian acquisition schemes. Another challenge with most of the current methods is that they are only designed for one derivative operator. [17, 27]. When multiple derivative operators are desired (e.g. directional derivatives), the problems are solved in a sequential fashion; the data recovered using one weighting is then used to recover the image with the other weighting.

Recently, we have introduced a fast and memory efficient structured low-rank matrix recovery algorithm called *Generic Iteratively Reweighted Annihilating Filter* (GIRAF) [59]. This approach works in the unlifted domain & exploits the convolutional structure of the structured matrix using Fast Fourier Transforms (FFT), which quite significantly reduces the computational complexity and memory demand of the algorithm. In addition, the algorithm is also general enough to handle arbitrary number of k-space weightings at the same time. In this work, we extend the GIRAF algorithm to recover signals that can be modeled as piecewise smooth functions in three dimensions. We demonstrate the improvement offered by this algorithm on breath held cine data over spatio-temporal total variation (TV) & temporal Fourier sparsity regularized reconstruction schemes.

5.2 Theory

Consider the general class of piecewise smooth functions g of degree n in d dimensions:

$$g(\mathbf{r}) = \sum_{i=1}^{N} g_i(\mathbf{r})\chi_{\Omega_\mathbf{i}}(\mathbf{r}), \quad \forall \mathbf{r} = (x, y) \in [0, 1]^d, \tag{5.1}$$

where χ_{Ω_i} is a characteristic function of the region $\Omega_\mathbf{i}$ and g_i are smooth polynomial functions of degree at most n. We assume that the edge set $\partial\Omega = \bigcup_{i=1}^{N} \partial\Omega_i$ coincides with the zero level sets of a d dimensional bandlimited function:

$$\mu(\mathbf{r}) = \sum_{\mathbf{k}\in\Delta} c[\mathbf{k}]e^{j2\pi\langle\mathbf{k},\mathbf{r}\rangle}, \quad \forall \mathbf{r} = (x, y) \in [0, 1]^d \tag{5.2}$$

where $c[\mathbf{k}] \in \mathbb{C}$ are the Fourier coefficients of μ and Δ is any finite subset of $\mathbb{Z}^2$. We have shown that such signals satisfy

$$\left(\partial_{x_1}^{n_1} \dots \partial_{x_d}^{n_d} g\right) \cdot \phi = 0; \quad \forall \quad n_1 + \dots n_d = n + 1, \tag{5.3}$$

where $\phi = \mu \cdot \eta$ is any function bandlimited to $\Lambda_1 \supseteq \Delta$, with a factor μ. The above conditions (5.3) translates into a convolution relation in the Fourier domain.

$$\left((j\omega_1)^{n_1} \dots (j\omega_d)^{n_d}\hat{g}\right) \star c = 0; \quad \forall \quad n_1 + \dots + n_d = n + 1 \tag{5.4}$$

We consider the recovery of the the Fourier coefficients on a rectangular region $\Gamma \subset \mathbb{Z}^d$. When $n = 0$ in (5.3), we obtain a piecewise constant signal model with conditions similar to the assumptions in classical total variation regularization. The annihilation relations in this case can be compactly written in matrix form as

$$\mathcal{T}(\hat{g})h = \begin{bmatrix} \mathcal{T}_1(\hat{g}) \\ \vdots \\ \mathcal{T}_d(\hat{g}) \end{bmatrix} \mathbf{h} = 0 \tag{5.5}$$

Here, $\mathcal{T}_i(\hat{g}) \in \mathbb{C}^{|\Lambda_2|\times|\Lambda_1|}$ is a Toeplitz/Hankel matrix whose entries are derived from $j\omega_i\hat{g}$; $\mathcal{T}_i(\hat{g})\mathbf{h}$ corresponds to the convolution of $j\omega_i\hat{g}$ with $\mathbf{h}$. Here, $\mathbf{h} \overset{\mathcal{F}}{\leftrightarrow} \phi$ is a d dimensional filter, supported in Λ_1. We have shown that the dimension of the space of filters $\mathbf{h}$ that satisfy (5.5) is given by the size of the set $\Lambda_1|\Delta$ — the valid shifts of the set Δ within Λ_1. $\Lambda_2 \in \Gamma$ indicates the set of indices over which the convolutions between the samples of $\hat{g}$ and $\mathbf{h}$ are valid. See Fig. 5.1 for an illustration of the structure of the lifted matrix $\mathcal{T}(\hat{g})$. Since the annihilation conditions are satisfied for filters $\mathbf{h}$ that live in a large subspace, we can conclude that $\mathcal{T}(\hat{g})$ is low rank. We use this property to recover $\hat{g}$ from non-uniform samples.

5.3 Proposed formulation

5.3.1 Measurement model

Let $\tilde{\mathbf{G}} \in \mathbb{C}^{\mathbf{P}\times\mathbf{T}}$ denote the Casoratti matrix structure of the dynamic MRI dataset, where each column $\tilde{\mathbf{G}}_i$ represents a vectorized image at a time point $\mathbf{t}_i$. We consider the recovery of the 3-D discrete Fourier coefficients of $\tilde{\mathbf{G}}$, denoted by $\mathbf{G}$. The Fourier measurements $\mathbf{b}$ can be modeled as:

$$\mathbf{b} = \mathbf{S}\mathbf{F}_t\mathbf{G} + \eta; \tag{5.6}$$

where $\mathbf{S}$ and η are the sampling matrix and zero mean white Gaussian noise vector respectively. $\mathbf{F}_t$ is the 1-D discrete inverse Fourier transform (DFT) matrix along the time direction. (5.6) can be compactly written as

$$\mathbf{b} = \mathcal{A}(\mathbf{G}) + \eta \tag{5.7}$$

where $\mathcal{A}$ is the measurement operator.

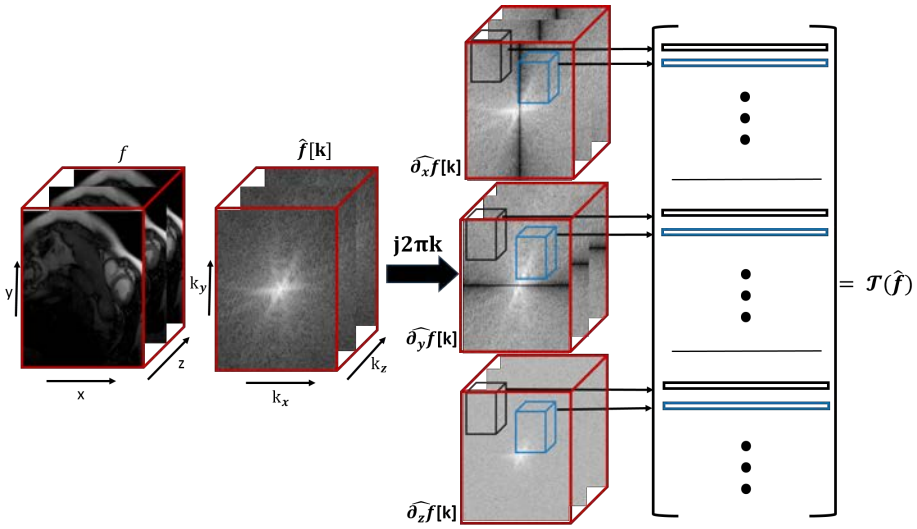

Figure 5.1: Illustration of the lifted matrix $\mathcal{T}(\mathbf{G})$: The rows of the matrix are cube shape neighborhoods of the weighted Fourier samples corresponding to the partial derivatives. We use the structure of the low-rank matrix to recover it from few measurements as in (5.9).

5.3.2 Problem formulation

We assume that the time series of MR images can be modeled as three dimensional piecewise constant functions and consider its recovery from few Fourier measurements. We formulate the problem in the Fourier domain and pose the recovery of $\mathbf{G}$ as the solution to the following structured low rank matrix completion problem.

$$\min_{\mathbf{G}} \ \text{rank}[\mathcal{T}(\mathbf{G})] \ \ s.t \ \ \mathbf{b} = \mathcal{A}(\mathbf{G}) + \eta \tag{5.8}$$

Here $\mathbf{G}$ is the data to be recovered. $\mathcal{T}(\mathbf{G}) \in \mathbb{C}^{\mathbf{M}\times\mathbf{N}}$ is a structured Toeplitz matrix in the lifted domain. Since (5.8) is NP hard, we relax the rank function with a Schatten $p(0 \leq p \leq 1)$ norm:

$$\mathbf{G}^{\star} = \arg\min_{\mathbf{G}} \|\mathcal{T}(\mathbf{G})\|_p + \frac{\lambda}{2}\|\mathcal{A}(\mathbf{G}) - \mathbf{b}\|_2^2 \tag{5.9}$$

where λ is a regularization parameter. Here, $\|\mathbf{X}\|_p$ is the Schatten p norm, defined as $\|\mathbf{X}\|_p := \frac{1}{p}\mathrm{Tr}[(\mathbf{X}^*\mathbf{X})^{\frac{p}{2}}] = \frac{1}{p}\sum_i \sigma_i^p$, where σ_i are the singular values of $\mathbf{X}$. $p = 1$ results in a convex nuclear norm penalty and when $(0 \leq p < 1)$, the Schatten norm is non-convex. When $p \to 0$, $\|\mathbf{X}\|_0 := \sum_i \log \sigma_i$.

Note that we lift the original problem involving a 3-D signal to a large matrix $\mathcal{T}(\mathbf{G})$, whose number of rows is around three times the total number of pixels in the 3-D volume. The number of columns is equal to the size of the filter. The explicit use of such a matrix requires a lot of memory for storage and also increases the computational complexity of the problem. Even for a data set of dimension $128 \times 128 \times 15$ and filter size of $21 \times 21 \times 3$, the memory demand is 1323 times the memory needed to store the original signal, which makes the application of the scheme to even modest sized datasets intractable.

5.4 Optimization algorithm

We use an iterative re-weighted least squares (IRLS) algorithm [47] to solve (5.9), which relies on the property $\|\mathbf{X}\|_p = \|\mathbf{X}\mathbf{H}^{\frac{1}{2}}\|_F^2$, where $\mathbf{H} = (\mathbf{X}^*\mathbf{X})^{\frac{p}{2}-1}$. Setting $\mathbf{X} = \mathcal{T}(\mathbf{G})$, we obtain the iterative algorithm that alternates between the following steps:

$$\mathbf{H}_n = [\mathcal{T}(\mathbf{G}_{n-1})^*\mathcal{T}(\mathbf{G}_{n-1}) + \epsilon_n \mathbf{I}]^{\frac{p}{2}-1} \tag{5.10}$$

$$\mathbf{G}_n = \arg\min_{\mathbf{G}} \|\mathcal{T}(\mathbf{G})\mathbf{H}_n^{\frac{1}{2}}\|_F^2 + \frac{\lambda}{2}\|\mathcal{A}(\mathbf{G}) - \mathbf{b}\|_2^2 \tag{5.11}$$

where $\epsilon_n \to 0$ is added to stabilize the inverse. We now show how the above steps can be modified to avoid the explicit evaluation and storage of the large lifted matrix $\mathcal{T}(\mathbf{G})$.

Update of $\mathbf{G}_n$:

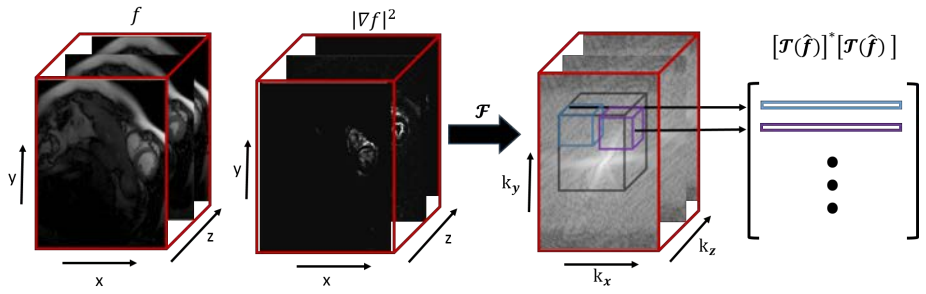

Figure 5.2: Illustration of the direct evaluation of $\mathcal{T}(\mathbf{G})^*\mathcal{T}(\mathbf{G})$ that does not require the lifting. This direct computation, as well as the update step (5.14) that does not require the lifted matrix, results in the fast and memory efficient algorithm for (5.9).

Denoting $\mathbf{H} = [\mathbf{h}_1, .., \mathbf{h}_N]$, we rewrite (2.17) as

$$\mathbf{G}^* = \arg\min_{\mathbf{G}} \frac{1}{2}\sum_{i=1}^{N} \|\mathcal{T}(\mathbf{G})\mathbf{h_i}\|_F^2 + \frac{\lambda}{2}\|\mathcal{A}(\mathbf{G}) - \mathbf{b}\|_2^2 \tag{5.12}$$

By exploiting the structure of $\mathcal{T}(\mathbf{G})$ and from the commutative property of convolution we have,

$$\mathcal{T}(\mathbf{G})\mathbf{h}_i = \mathcal{P}_{\Lambda_2}(\mathcal{Q}(\mathbf{G}) * \mathbf{h}_i) = \mathcal{P}_{\Lambda_2}(\mathbf{h}_i * \mathcal{Q}(\mathbf{G})) = \mathbf{P}\mathbf{C_i}\mathcal{Q}(\mathbf{G}) \tag{5.13}$$

Here, $*$ denotes 3-D convolution. $\mathcal{Q}$ is a linear operator specified by $\mathcal{Q} = \left[\mathcal{Q}_x^*, \mathcal{Q}_{\mathbf{y}}^*, \alpha\mathcal{Q}_{\mathbf{z}}^*\right]^*$. Here, $\mathcal{Q}(\mathbf{G})$ represents element wise multiplication of $\mathbf{G}$ by Fourier derivatives $j2\pi k_x$, $j2\pi k_y$ and $j2\pi k_z$ where $\mathbf{k} = (k_x, k_y, k_z)$. $\mathbf{C}_i$ represents the 3-D linear convolution by $\mathbf{h}_i$. $\mathcal{P}_{\Lambda_2}$ is the projection of the convolution onto a valid k space index set Λ_2 and is represented by the matrix $\mathbf{P}$.

We approximate $\mathbf{C}_i$ by a 3-D circular convolution by $\mathbf{h_i}$, which is valid if the convolution grid is sufficiently large. This allows us to evaluate $\mathbf{C}_i$ as $\mathbf{F}\mathbf{D}_i\mathbf{F}^*$, where $\mathbf{F}$ is the 3-D DFT matrix and $\mathbf{D}_i$ is a diagonal matrix corresponding to the 3-D inverse DFT of $\mathbf{h}_i$. We also assume $\mathbf{P}^*\mathbf{P} \approx \mathbf{I}$, which is valid if the projection set Λ_2 is large compared to the filter size. Substituting (5.13) in (5.12) and then taking the

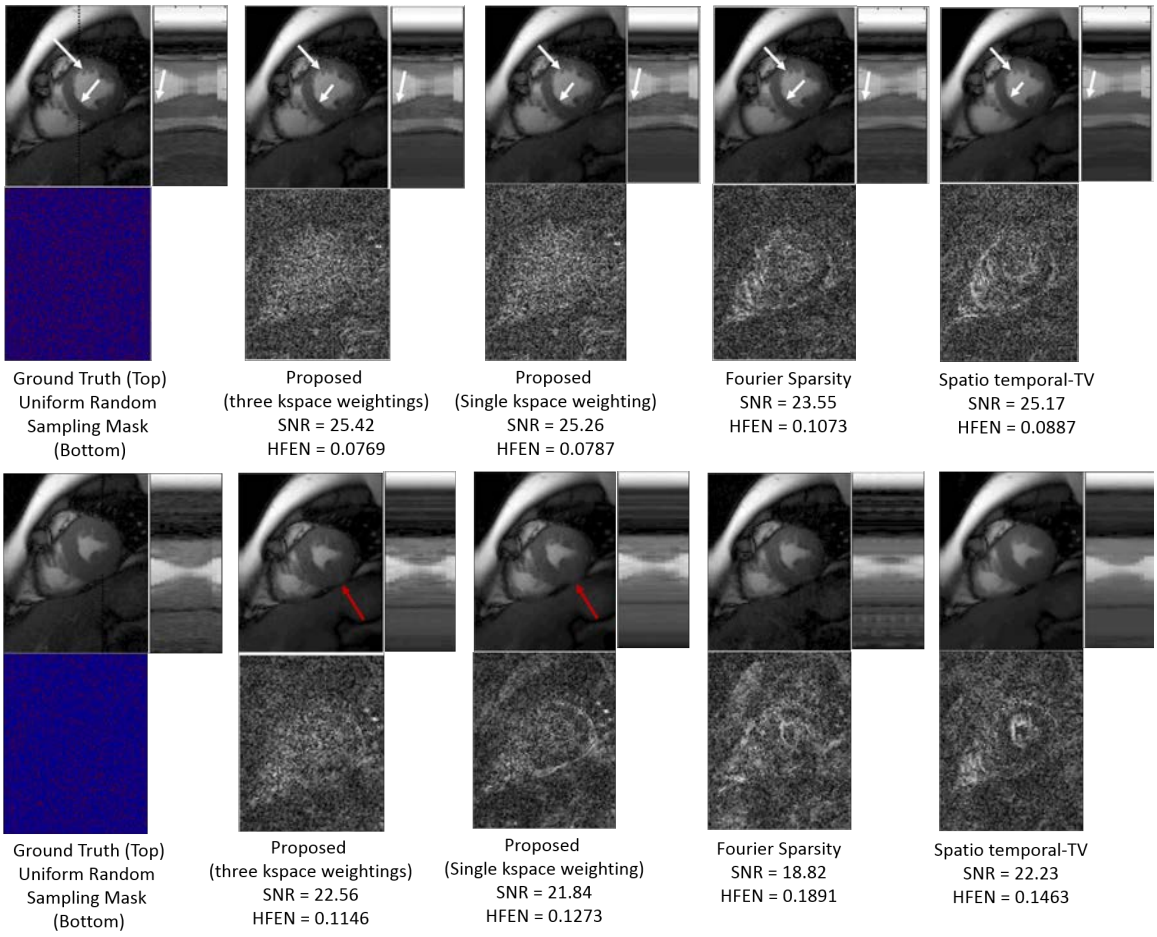

Figure 5.3: Comparison of the proposed scheme (single weighting and multiple weighting) with temporal Fourier sparsity and spatio-temporal TV methods at an acceleration factor of four (top row) and seven (bottom Row).

gradient, we obtain

$$\underbrace{\left(\mathcal{Q}^*\mathbf{F}\underbrace{\left(\sum_{i=1}^{N}\mathbf{D}_i^*\mathbf{D}_i\right)}_{\mathbf{D}(\overline{\mu})}\mathbf{F}^*\mathcal{Q}+\lambda\,\mathcal{A}^*\mathcal{A}\right)}_{\mathbf{R}}\mathbf{G}=\lambda\,\mathcal{A}^*\mathbf{b} \tag{5.14}$$

where $\mathbf{D}(\overline{\mu})$ is a diagonal matrix with entries

$$\overline{\mu}(\mathbf{r}) = \sum_{i=1}^{N} |\mu_i(\mathbf{r})|^2, \quad \forall(\mathbf{r}) \in [0,1]^3 \tag{5.15}$$

Here, $\mu_i(\mathbf{r})$ is a trigonometric polynomial corresponding to the inverse fourier transform of $\mathbf{h_i}$. With these approximations, forming matrix vector products with $\mathbf{R}$ only requires 2 FFT's after precomputing $\overline{\mu}$.

Update of $\overline{\mu}(\mathbf{r})$:

Using the convoution relation mentioned in (5.13), the correlation matrix $\mathbf{R} = \mathcal{T}(\mathbf{G})^*\mathcal{T}(\mathbf{G})$ can be computed as

$$\mathbf{R} \approx \mathcal{P}_{\Lambda_1}[\mathbf{C}(\mathcal{Q}(\mathbf{G}))^*\mathbf{C}(\mathcal{Q}(\mathbf{G}))]\mathcal{P}^*_{\Lambda_1} \tag{5.16}$$

where $\mathcal{P}_{\Lambda_1}$ is the projection onto the set Λ_1, $\mathbf{C}$ is applied to each block of $\mathcal{Q}(\mathbf{G})$ and represents circular convolution. By expressing $\mathbf{C}$ in terms of the DFT matrix $\mathbf{F}$, we can simplify (5.16) further and obtain $\mathbf{R} \approx \mathcal{P}_{\Lambda_1}[\mathbf{FDF}^*]P^*_{\Lambda_1}$ where $\mathbf{D}$ is a diagonal matrix whose entries correspond to $|\nabla|^2 := \left(|\frac{\partial \tilde{\mathbf{G}}}{\partial_x}|^2 + |\frac{\partial \tilde{\mathbf{G}}}{\partial_y}|^2 + |\frac{\partial \tilde{\mathbf{G}}}{\partial_z}|^2\right)$. Hence the entries of $\mathbf{R}$ are obtained from the Fourier coefficients of $|\nabla|^2$; specifically every row of $\mathbf{R}$ is obtained by vectorizing a brick shaped region of size equal to the dimensions of the filter from the black cuboid region of dimension twice the size of the filter. See Fig. 5.2 which depicts the construction of $\mathbf{R}$.

Next the weight matrix $\mathbf{H}$ can be efficiently computed from the eigen decomposition of $\mathbf{R}$. Let $(\mathbf{V}, \mathbf{\Lambda})$ be the eigen decomposition of $\mathcal{T}(\mathbf{G})^*\mathcal{T}(\mathbf{G})$, where $\mathbf{V}$ is the orthogonal basis of eigen vectors $\mathbf{v_i}$ and Λ is a diagonal matrix containing the eigen values $\lambda_\mathbf{i}$. Substituting the eigen decomposition in (2.18) and simplifying further we obtain,

$$\mathbf{H} = [\mathbf{V}(\mathbf{\Lambda} + \epsilon\mathbf{I})\mathbf{V}^*]^{\frac{p}{2}-1} = \mathbf{V}(\mathbf{\Lambda} + \epsilon\mathbf{I})^{\frac{p}{2}-1}\mathbf{V}^*.$$

Hence, one choice of the matrix square root $\mathbf{H}^{\frac{1}{2}}$ is

$$\mathbf{H}^{\frac{1}{2}} = \mathbf{V}(\mathbf{\Lambda} + \epsilon\mathbf{I})^{\frac{p}{4}-\frac{1}{2}} = [\alpha_1^{\frac{1}{2}}\mathbf{v}_1, \ldots, \alpha_N^{\frac{1}{2}}\mathbf{v}_N].$$

where $\alpha_i = (\lambda_i + \epsilon)^{\frac{p}{2}-1}$. The spatial domain trigonometric polynomial $\mu_\mathbf{i}$ and $\mathbf{v_i}$ are related as $\mu_\mathbf{i} = \alpha_\mathbf{i}^{\frac{1}{2}}\gamma_\mathbf{i}(\mathbf{r})$ where $\gamma_\mathbf{i}(\mathbf{r})$ is the inverse fourier transform of the eigen vector $\mathbf{v_i}$. Hence using this relation, the SOS polynomial is updated as

$$\overline{\mu}(\mathbf{r}) = \sum_{i=1}^{N} \alpha_\mathbf{i}|\gamma_i(\mathbf{r})|^2, \quad \forall(\mathbf{r}) \in [0,1]^3 \tag{5.17}$$

which can be efficiently computed using $\mathbf{N}$ FFT's. Note that the weights $\alpha_\mathbf{i}$ are only high for vectors $\mathbf{v_i}$ close to the null space.

5.5 Results

In Fig 5.3 , we compare the recovery of the proposed method (single weighting and multiple weighting) with the spatio-temporal TV (S-TV) and temporal Fourier Sparsity (FS) regularized reconstruction methods on a Breath Held Cine Data of dimension $(224 \times 256 \times 16 \times 5)$ (coil compressed) at an acceleration factor of four and seven respectively. The data was acquired using a SSFP sequence using the following parameters: TE/TR= 2.0/4.1 ms and flip angle=45°. For the proposed method, a filter size of $(21 \times 21 \times 3)$ was used in the recovery.

$\mathcal{Q}$ is defined as $\sqrt{(j\omega_x)^2 + (j\omega_y)^2 + (\alpha j\omega_z)^2}$ for the proposed method with single kspace weighting. As this is an isotropic operator, at an acceleration factor of seven, it results in a recovery with some edges blurred, compared to the proposed method with multiple weightings and TV. The reconstructions from the proposed method with multiple weightings are more accurate with a lot of details faithfully captured. Specifically, the errors corresponding to it are scattered as opposed to being concentrated along the edges, which is the case with TV and Fourier sparsity based methods.

5.6 Conclusion

We introduced a fast & memory efficient algorithm to recover piecewise smooth three dimensional signals from few of their measurements. The algorithm is similar in concept to iterative reweighted algorithm for total variation regularization, with the exception that the weights are derived using a novel Fourier domain strategy involving singular value decomposition. The ability of the scheme to additionally regularize the smoothness of the edges enables it to provide improved results over total variation regularization. The comparison of the proposed scheme against state of the art methods in the context of cine MRI demonstrates its ability to provide more accurate reconstructions with better edge details.

CHAPTER 6
SUMMARY AND FUTURE DIRECTIONS

6.1 Summary

In this thesis, we have studied the problem of recovering a series of images, in which the temporal profile at every pixel follows an exponential curve, from very few Fourier measurements. We exploit the exponential signal at every pixel location along with the smooth structure present in the exponential parameters to derive a 3D annihilation relation in the Fourier domain. This relation translates into a product of a low rank Toeplitz structured matrix and a vector of filter coefficients. We exploit this low rank property to recover the images from undersampled measurements. We pose the recovery as a structured low rank optimization problem. To solve the problem, we employ an iterative re-weighted least squares (IRLS) based algorithm which enables us to exploit the convolution structure present in the Toeplitz matrix. We also present novel approximations to solve the problem efficiently for different applications.

First we demonstrate the algorithm on the problem of MR parameter mapping. The direct implementation of the above algorithm results in a memory intensive and computationally expensive algorithm. We address these issues by introducing novel approximations in the Fourier domain, which enable us to solve the sub-problems efficiently using fast Fourier transforms (FFTs). We show that the proposed algorithm provides improved reconstructions and maps compared to those obtained from the competing methods. Most of these methods exploit the signal structures such as sparsity, smoothness, low rankness or linear predictability of the exponential signals to recover the images. The proposed work can be thought of as a strategy that unifies the aforementioned methods. Specifically, the proposed prior qualitatively combines all of the above mentioned priors into one single prior.

Next we introduce a structured low rank algorithm for the calibration-free compensation of field inhomogeneity artifacts in EPI data. For this purpose, we combined

information from two EPI acquisitions and reformulated the artifact correction problem into a recovery of time series of images from undersampled measurements. This reformulation allowed us to exploit the smooth structure of the exponential 3D dataset to derive a low rank structured matrix prior in the Fourier domain. We enforced the low rankness of the matrix as a prior to recover the time series of images. The reformulation resulted in a unique pattern of measurements in every frame, which inspired us to come up with a fast two step algorithm. In the first step, we proposed two strategies to estimate the field map from the measured EPI data. This was followed by estimating the distortion-free image, which was obtained as a solution of a least squares problem. We validated the proposed method on phantom and human data and showed that the artifacts were significantly reduced compared to the single shot uncorrected EP image.

We extended the structured low rank method to correct inhomogeneity related artifacts on data acquired using a Rosette trajectory. The reformulation of the problem as a time series recovery resulted in measurements following an incoherent undersampling pattern between frames. This enabled us to solve the optimization problem using a compressed sensing based iterative algorithm, similar to the one applied for MR parameter mapping. We designed the rosette trajectory and acquired MR phantom datasets. We applied the algorithm in the datasets and observed that the intensity losses were significantly reduced.

Last, we developed a structured matrix recovery framework to accelerate cardiac MRI. We modeled the breath-held cardiac data as a 3D piecewise constant function and derived Fourier domain annihilation relations between the Fourier samples of the gradient images and a vector of filter coefficients. We exploited these relations to recover the series of images from undersampled measurements. We compared the proposed method against conventional sparsity and smoothness based methods and showed that the proposed reconstructions had fewer artifacts and errors. We note

that even though the signal model is not exponential here, the algorithm developed is very similar to the one applied to the parameter mapping case.

We have developed novel computationally efficient algorithms to solve important problems in various MRI applications. They are capable of working with high dimensional datasets efficiently. Though we have demonstrated the algorithms in MRI applications, they are general enough to be extended to imaging applications beyond MRI.

6.2 Future directions

Application to MR Spectroscopy: The structured matrix recovery algorithm developed in this thesis was demonstrated on the problem of MR parameter mapping. This could be extended to the problem of denoising in MR spectroscopy (MRS). In MRS, the goal is to estimate the spatial map of different metabolite concentrations from a time series of images. The maps provide useful clinical information and act as biomarkers for neurological disorders. However, the concentration of metabolites is orders of magnitude lower than water resulting in very low SNR images. Thus denoising the images is essential to obtaining accurate metabolite maps. Similar to parameter mapping, the temporal profile at every pixel location follows an exponential decay. This structure can be exploited along with the smoothness of the concentration maps to derive a structured matrix prior. We can exploit the low rank property to denoise the time series of images.

Dynamic field map compensation: In this work, we have developed a structured low rank algorithm and corrected field inhomogeneity artifacts in a single image. However, in many dynamic applications such as fMRI, a single field map estimated in the beginning of the scan cannot be used for correcting the artifacts in the entire image series. This is because the field map could change due to subject motion, scanner drift and respiration. Our algorithm developed for EPI acquisitions can be extended to the dynamic case. In order to do this, the two EPI datasets can be acquired in an

interleaved fashion. Specifically, the readout of datasets acquired at even time points can be delayed from the datasets acquired at odd time points by a few ms. The field map compensation can then be done using every pair of neighboring datasets using our structured low rank algorithm.

Accelerating perfusion cardiac MRI: In this work, we have developed an algorithm for accelerating breath-held cardiac MRI. For this application, we assumed a piece-wise constant image model and derived annihilation relations accordingly. However for applications such as perfusion MRI, where there is contrast flow in addition to cardiac motion, this model might not be accurate. Hence we could move towards piece-wise linear or polynomial signal models for representation and derive appropriate annihilation relations, resulting in a similar structured low rank matrix prior. We can exploit the low rank structure to recover the perfusion images from undersampled measurements. Since we consider a higher order model, the size of the Toeplitz matrix would be very large. We can introduce Fourier domain approximations, similar to the ones in this work, to reduce the computational complexity.

REFERENCES

[1] J. L. Andersson, S. Skare, and J. Ashburner, "How to correct susceptibility distortions in spin-echo echo-planar images: application to diffusion tensor imaging," *Neuroimage*, vol. 20, no. 2, pp. 870–888, 2003.

[2] D. Atkinson, D. A. Porter, D. L. Hill, F. Calamante, and A. Connelly, "Sampling and reconstruction effects due to motion in diffusion-weighted interleaved echo planar imaging," *Magnetic Resonance in Medicine: An Official Journal of the International Society for Magnetic Resonance in Medicine*, vol. 44, no. 1, pp. 101–109, 2000.

[3] A. Balachandrasekaran and M. Jacob, "Novel structured Low-rank algorithm to recover spatially smooth exponential image time series," in *IEEE 14th International Symposium on Biomedical Imaging 2017*.

[4] A. Balachandrasekaran, V. Magnotta, and M. Jacob, "Recovery of damped exponentials using structured low rank matrix completion," *IEEE Transactions on Medical Imaging*, vol. 36, no. 10, pp. 2087–2098, 2017.

[5] A. Balachandrasekaran, M. Mani, and M. Jacob, "Calibration-free B0 correction of EPI data using structured low rank matrix recovery," *arXiv preprint arXiv:1804.07436*, 2018.

[6] N. Ben-Eliezer, D. K. Sodickson, and K. T. Block, "Rapid and accurate T2 mapping from multi–spin-echo data using bloch-simulation-based reconstruction," *Magnetic Resonance in Medicine*, vol. 73, no. 2, pp. 809–817, 2015.

[7] S. Bhave, S. G. Lingala, C. P. Johnson, V. A. Magnotta, and M. Jacob, "Accelerated whole-brain multi-parameter mapping using blind compressed sensing," *Magnetic Resonance in Medicine*, 2015.

[8] A. Borthakur, M. Sochor, C. Davatzikos, J. Q. Trojanowski, and C. M. Clark, "T1ρ MRI of Alzheimer's disease," *Neuroimage*, vol. 41, no. 4, pp. 1199–1205, 2008.

[9] Y. Chen and Y. Chi, "Robust spectral compressed sensing via structured matrix completion," *Information Theory, IEEE Transactions on*, vol. 60, no. 10, pp. 6576–6601, 2014.

[10] A. Crawley and R. Henkelman, "Errors in T2 estimation using multislice multiple-echo imaging," *Magnetic Resonance in Medicine*, vol. 4, no. 1, pp. 34–47, 1987.

[11] A. Di Costanzo, F. Trojsi, M. Tosetti, T. Schirmer, S. M. Lechner, T. Popolizio, and T. Scarabino, "Proton MR spectroscopy of the brain at 3T: an update," *European radiology*, vol. 17, no. 7, pp. 1651–1662, 2007.

[12] M. Doneva, P. Börnert, H. Eggers, C. Stehning, J. Sénégas, and A. Mertins, "Compressed sensing reconstruction for magnetic resonance parameter mapping," *Magnetic Resonance in Medicine*, vol. 64, no. 4, pp. 1114–1120, 2010.

[13] B. Dymerska, B. A. Poser, W. Bogner, E. Visser, K. Eckstein, P. Cardoso, M. Barth, S. Trattnig, and S. D. Robinson, "Correcting dynamic distortions in 7T echo planar imaging using a jittered echo time sequence," *Magnetic Resonance in Medicine*, vol. 76, no. 5, pp. 1388–1399, 2016.

[14] L. Feng, R. Otazo, H. Jung, J. H. Jensen, J. C. Ye, D. K. Sodickson, and D. Kim, "Accelerated cardiac T2 mapping using breath-hold multiecho fast spin-echo pulse sequence with k-t FOCUSS," *Magnetic Resonance in Medicine*, vol. 65, no. 6, pp. 1661–1669, 2011.

[15] J. A. Fessler, S. Lee, V. T. Olafsson, H. R. Shi, and D. C. Noll, "Toeplitz-based iterative image reconstruction for MRI with correction for magnetic field inhomogeneity," *IEEE Transactions on Signal Processing*, vol. 53, no. 9, pp. 3393–3402, 2005.

[16] M. Guerquin-Kern, L. Lejeune, K. P. Pruessmann, and M. Unser, "Realistic analytical phantoms for parallel magnetic resonance imaging," *Medical Imaging, IEEE Transactions on*, vol. 31, no. 3, pp. 626–636, 2012.

[17] J. Haldar, "Low-rank modeling of local k -space neighborhoods (LORAKS) for constrained MRI," *IEEE Transactions on Medical Imaging*, vol. 33, no. 3, pp. 668–681, March 2014.

[18] J. P. Haldar, "Autocalibrated LORAKS for fast constrained MRI reconstruction," in *IEEE 12th International Symposium on Biomedical Imaging (ISBI) 2015*. IEEE, 2015, pp. 910–913.

[19] P. C. Hansen and D. P. OLeary, "The use of the l-curve in the regularization of discrete ill-posed problems," *SIAM Journal on Scientific Computing*, vol. 14, no. 6, pp. 1487–1503, 1993.

[20] P. A. Hardy, R. S. Hinks, and J. A. Tkach, "Separation of fat and water in fast spin-echo MR imaging with the three-point Dixon technique," *Journal of Magnetic Resonance Imaging*, vol. 5, no. 2, pp. 181–185, 1995.

[21] T. B. Harshbarger and D. B. Twieg, "Iterative reconstruction of single-shot spiral MRI with off resonance," *IEEE Transactions on Medical Imaging*, vol. 18, no. 3, pp. 196–205, 1999.

[22] J. Hennig, "Multiecho imaging sequences with low refocusing flip angles," *Journal of Magnetic Resonance (1969)*, vol. 78, no. 3, pp. 397–407, 1988.

[23] D. Holland, J. M. Kuperman, and A. M. Dale, "Efficient correction of inhomogeneous static magnetic field-induced distortion in echo planar imaging," *Neuroimage*, vol. 50, no. 1, pp. 175–183, 2010.

[24] C. Huang, C. G. Graff, E. W. Clarkson, A. Bilgin, and M. I. Altbach, "T2 mapping from highly undersampled data by reconstruction of principal component coefficient maps using compressed sensing," *Magnetic Resonance in Medicine*, vol. 67, no. 5, pp. 1355–1366, 2012.

[25] P. Irarrazabal, C. H. Meyer, D. G. Nishimura, and A. Macovski, "Inhomogeneity correction using an estimated linear field map," *Magnetic Resonance in Medicine*, vol. 35, no. 2, pp. 278–282, 1996.

[26] P. Jezzard and R. S. Balaban, "Correction for geometric distortion in echo planar images from B0 field variations," *Magnetic Resonance in Medicine*, vol. 34, no. 1, pp. 65–73, 1995.

[27] K. H. Jin, D. Lee, and J. C. Ye, "A general framework for compressed sensing and parallel mri using annihilating filter based low rank Hankel matrix," *IEEE Transactions on Computational Imaging*, vol. 2, no. 4, pp. 480–495, 2016.

[28] Y. M. Kadah and X. Hu, "Simulated phase evolution rewinding (SPHERE): A technique for reducing B0 inhomogeneity effects in MR images," *Magnetic Resonance in Medicine*, vol. 38, no. 4, pp. 615–627, 1997.

[29] T. Knopp, H. Eggers, H. Dahnke, J. Prestin, and J. Senegas, "Iterative off-resonance and signal decay estimation and correction for multi-echo MRI," *IEEE Transactions on Medical Imaging*, vol. 28, no. 3, pp. 394–404, 2009.

[30] K. K. Kwong, J. W. Belliveau, D. A. Chesler, I. E. Goldberg, R. M. Weisskoff, B. P. Poncelet, D. N. Kennedy, B. E. Hoppel, M. S. Cohen, and R. Turner, "Dynamic magnetic resonance imaging of human brain activity during primary sensory stimulation." *Proceedings of the National Academy of Sciences*, vol. 89, no. 12, pp. 5675–5679, 1992.

[31] D. Lee, K. H. Jin, E. Y. Kim, S.-H. Park, and J. C. Ye, "Acceleration of MR parameter mapping using annihilating filter-based low rank Hankel matrix," *Magnetic Resonance in Medicine*, 2016.

[32] J. Lee, K. H. Jin, and J. C. Ye, "Reference-free single-pass EPI Nyquist ghost correction using annihilating filter-based low rank Hankel matrix (ALOHA)," *Magnetic Resonance in Medicine*, vol. 76, no. 6, pp. 1775–1789, 2016.

[33] W. Li, M. Griswold, and X. Yu, "Fast cardiac T1 mapping in mice using a model-based compressed sensing method," *Magnetic Resonance in Medicine*, vol. 68, no. 4, pp. 1127–1134, 2012.

[34] Z.-P. Liang, "Spatiotemporal imaging with partially separable functions," in *2007 4th IEEE International Symposium on Biomedical Imaging: From Nano to Macro*. IEEE, 2007, pp. 988–991.

[35] Z.-P. Liang, E. Haacke, and C. Thomas, "High-resolution inversion of finite Fourier transform data through a localised polynomial approximation," *Inverse Problems*, vol. 5, no. 5, p. 831, 1989.

[36] R. S. Likes, "Moving gradient zeugmatography," Dec. 22 1981, US Patent 4,307,343.

[37] S. G. Lingala, Y. Hu, E. DiBella, and M. Jacob, "Accelerated dynamic MRI exploiting sparsity and low-rank structure:kt SLR," *IEEE Transactions on Medical imaging*, vol. 30, no. 5, pp. 1042–1054, 2011.

[38] R. A. Lobos, T. H. Kim, W. S. Hoge, and J. P. Haldar, "Navigator-free EPI ghost correction using low-rank matrix modeling: Theoretical insights and practical improvements," in *Proc. Int. Soc. Magn. Reson. Med*, 2017, p. 0449.

[39] M. Lustig and J. Pauly, "Spirit: Iterative self-consistent parallel imaging reconstruction from arbitrary k-space sampling," *Magnetic resonance in medicine*, vol. 64, pp. 457–71, 2010.

[40] A. Maeda, K. Sano, and T. Yokoyama, "Reconstruction by weighted correlation for MRI with time-varying gradients," *IEEE Transactions on Medical Imaging*, vol. 7, no. 1, pp. 26–31, 1988.

[41] S. Majumdar, S. Orphanoudakis, A. Gmitro, M. O'donnell, and J. Gore, "Errors in the measurements of T2 using multiple-echo MRI techniques. I. Effects of radiofrequency pulse imperfections," *Magnetic Resonance in Medicine*, vol. 3, no. 3, pp. 397–417, 1986.

[42] S. Majumdar, S. Orphanoudakis, A. Gmitro, M. O'Donnell, and J. Gore, "Errors in the measurements of T2 using multiple-echo MRI techniques. II. Effects of static field inhomogeneity," *Magnetic Resonance in Medicine*, vol. 3, no. 4, pp. 562–574, 1986.

[43] L.-C. Man, J. M. Pauly, and A. Macovski, "Multifrequency interpolation for fast off-resonance correction," *Magnetic Resonance in Medicine*, vol. 37, no. 5, pp. 785–792, 1997.

[44] M. Mani, M. Jacob, D. Kelley, and V. Magnotta, "Multi-shot sensitivity-encoded diffusion data recovery using structured low-rank matrix completion (MUSSELS)," *Magnetic Resonance in Medicine*, vol. 78, no. 2, pp. 494–507, 2017.

[45] M. Mani, V. Magnotta, and M. Jacob, "A general algorithm for compensation of trajectory errors: Application to radial imaging," *Magnetic Resonance in Medicine*, 2018.

[46] M. Mani, V. Magnotta, D. Kelley, and M. Jacob, "Comprehensive reconstruction of multi-shot multi-channel diffusion data using MUSSELS," in *IEEE 38th Annual International Conference of the Engineering in Medicine and Biology Society (EMBC) 2016*, pp. 1107–1110.

[47] K. Mohan and M. Fazel, "Iterative reweighted algorithms for matrix rank minimization," *The Journal of Machine Learning Research*, vol. 13, no. 1, pp. 3441–3473, 2012.

[48] P. Munger, G. R. Crelier, T. M. Peters, and G. B. Pike, "An inverse problem approach to the correction of distortion in EPI images," *IEEE Transactions on Medical Imaging*, vol. 19, no. 7, pp. 681–689, 2000.

[49] H. M. Nguyen, X. Peng, M. N. Do, and Z.-P. Liang, "Denoising MR spectroscopic imaging data with low-rank approximations," *IEEE Transactions on Biomedical Engineering*, vol. 60, no. 1, pp. 78–89, 2013.

[50] H. M. Nguyen, B. P. Sutton, R. L. Morrison Jr, and M. N. Do, "Joint estimation and correction of geometric distortions for EPI functional MRI using harmonic retrieval," *IEEE Transactions on Medical Imaging*, vol. 28, no. 3, pp. 423–434, 2009.

[51] D. G. Nishimura, *Principles of magnetic resonance imaging*. Stanford University, 1996.

[52] D. C. Noll, "Multishot rosette trajectories for spectrally selective MR imaging," *IEEE transactions on medical imaging*, vol. 16, no. 4, pp. 372–377, 1997.

[53] D. C. Noll, C. H. Meyer, J. M. Pauly, D. G. Nishimura, and A. Macovski, "A homogeneity correction method for magnetic resonance imaging with time-varying gradients," *IEEE Transactions on Medical Imaging*, vol. 10, no. 4, pp. 629–637, 1991.

[54] D. C. Noll, "Reconstruction techniques for magnetic resonance imaging." 1992.

[55] V. T. Olafsson, D. C. Noll, and J. A. Fessler, "Fast joint reconstruction of dynamic R2* and field maps in functional MRI," *IEEE Transactions on Medical Imaging*, vol. 27, no. 9, pp. 1177–1188, 2008.

[56] G. Ongie and M. Jacob, "Recovery of piecewise smooth images from few Fourier samples," *SampTA*, 2015.

[57] G. Ongie, S. Biswas, and M. Jacob, "Convex recovery of continuous domain piecewise constant images from nonuniform Fourier samples," *IEEE Transactions on Signal Processing*, vol. 66, no. 1, pp. 236–250, 2017.

[58] G. Ongie and M. Jacob, "Super-resolution MRI using finite rate of innovation curves," in *IEEE 12th International Symposium on Biomedical Imaging (ISBI), 2015*. IEEE, 2015, pp. 1248–1251.

[59] ——, "A fast algorithm for structured low-rank matrix recovery with applications to undersampled MRI reconstruction," *IEEE International Symposium on Biomedical Imaging (ISBI)*, April 2016.

[60] ——, "Off-the-grid recovery of piecewise constant images from few Fourier samples," *SIAM Journal on Imaging Sciences*, vol. 9, no. 3, pp. 1004–1041, 2016.

[61] ——, "A fast algorithm for convolutional structured low-rank matrix recovery," *IEEE Transactions on Computational Imaging*, vol. 3, no. 4, pp. 535–550, 2017.

[62] H. Pan, T. Blu, and P. L. Dragotti, "Sampling curves with finite rate of innovation," *IEEE Transactions on Signal Processing*, vol. 62, no. 2, 2014.

[63] X. Peng, L. Ying, Y. Liu, J. Yuan, X. Liu, and D. Liang, "Accelerated exponential parameterization of T2 relaxation with model-driven low rank and sparsity priors MORASA," *Magnetic Resonance in Medicine*, 2016.

[64] F. H. Petzschner, I. P. Ponce, M. Blaimer, P. M. Jakob, and F. A. Breuer, "Fast MR parameter mapping using k-t principal component analysis," *Magnetic Resonance in Medicine*, vol. 66, no. 3, pp. 706–716, 2011.

[65] M. Poustchi-Amin, S. A. Mirowitz, J. J. Brown, R. C. McKinstry, and T. Li, "Principles and applications of echo-planar imaging: A review for the general radiologist," *Radiographics*, vol. 21, no. 3, pp. 767–779, 2001.

[66] S. Ramani, T. Blu, and M. Unser, "Monte-carlo sure: A black-box optimization of regularization parameters for general denoising algorithms," *IEEE Transactions on Image Processing*, vol. 17, no. 9, pp. 1540–1554, 2008.

[67] S. Ramani, Z. Liu, J. Rosen, J.-F. Nielsen, and J. A. Fessler, "Regularization parameter selection for nonlinear iterative image restoration and mri reconstruction using gcv and sure-based methods," *IEEE Transactions on Image Processing*, vol. 21, no. 8, pp. 3659–3672, 2012.

[68] E. Schneider and G. Glover, "Rapid in vivo proton shimming," *Magnetic Resonance in Medicine*, vol. 18, no. 2, pp. 335–347, 1991.

[69] H. Schomberg, "Off-resonance correction of MR images," *IEEE Transactions on Medical Imaging*, vol. 18, no. 6, pp. 481–495, 1999.

[70] I. Shenberg and A. Macovski, "Inhomogeneity and multiple dimension considerations in magnetic resonance imaging with time-varying gradients," *IEEE Transactions on Medical Imaging*, vol. 4, no. 3, pp. 165–174, 1985.

[71] P. J. Shin, P. E. Larson, M. A. Ohliger, M. Elad, J. M. Pauly, D. B. Vigneron, and M. Lustig, "Calibrationless parallel imaging reconstruction based on structured low-rank matrix completion," *Magnetic Resonance in Medicine*, vol. 72, no. 4, pp. 959–970, 2014.

[72] P. Stoica and R. L. Moses, *Introduction to spectral analysis*. Prentice hall Upper Saddle River, NJ, 1997, vol. 1.

[73] B. P. Sutton, D. C. Noll, and J. A. Fessler, "Fast, iterative image reconstruction for MRI in the presence of field inhomogeneities," *IEEE Transactions on Medical Imaging*, vol. 22, no. 2, pp. 178–188, 2003.

[74] ——, "Dynamic field map estimation using a spiral-in/spiral-out acquisition," *Magnetic Resonance in Medicine*, vol. 51, no. 6, pp. 1194–1204, 2004.

[75] J. I. Tamir, M. Uecker, W. Chen, P. Lai, M. T. Alley, S. S. Vasanawala, and M. Lustig, "T2 shuffling: Sharp, multicontrast, volumetric fast spin-echo imaging," *Magnetic resonance in medicine*, vol. 77, no. 1, pp. 180–195, 2017.

[76] M. Ugander, P. S. Bagi, A. J. Oki, B. Chen, L.-Y. Hsu, A. H. Aletras, S. Shah, A. Greiser, P. Kellman, and A. E. Arai, "Myocardial edema as detected by precontrast T1 and T2 CMR delineates area at risk associated with acute myocardial infarction," *JACC: Cardiovascular Imaging*, vol. 5, no. 6, pp. 596–603, 2012.

[77] J. V. Velikina, A. L. Alexander, and A. Samsonov, "Accelerating MR parameter mapping using sparsity-promoting regularization in parametric dimension," *Magnetic Resonance in Medicine*, vol. 70, no. 5, pp. 1263–1273, 2013.

[78] M. Vetterli, P. Marziliano, and T. Blu, "Sampling signals with finite rate of innovation," *IEEE Transactions on Signal Processing*, vol. 50, no. 6, pp. 1417–1428, June 2002.

[79] T. Zhang, J. M. Pauly, and I. R. Levesque, "Accelerating parameter mapping with a locally low rank constraint," *Magnetic Resonance in Medicine*, vol. 73, no. 2, pp. 655–661, 2015.

[80] B. Zhao, F. Lam, and Z.-P. Liang, "Model-based MR parameter mapping with sparsity constraints: parameter estimation and performance bounds," *IEEE Transactions on Medical Imaging*, vol. 33, no. 9, pp. 1832–1844, 2014.

[81] B. Zhao, W. Lu, T. K. Hitchens, F. Lam, C. Ho, and Z.-P. Liang, "Accelerated MR parameter mapping with low-rank and sparsity constraints," *Magnetic Resonance in Medicine*, vol. 74, no. 2, pp. 489–498, 2015.

[82] Y. Zhu, Q. Zhang, Q. Liu, Y.-X. J. Wang, X. Liu, H. Zheng, D. Liang, and J. Yuan, "PANDA-T1ρ: Integrating principal component analysis and dictionary learning for fast T1ρ mapping," *Magnetic Resonance in Medicine*, vol. 73, no. 1, pp. 263–272, 2015.